UNIVERSITY OF CALIFORNIA, MERCED

The Integrated Compound Parabolic Concentrator (ICPC): a low cost, non-tracking, solar thermal collector for low carbon process heating up to 150˚C

A dissertation submitted in partial satisfaction of the requirements for the degree of

Doctor of Philosophy

In

Environmental Systems

By

Jordyn Brinkley

Committee Members:

Professor Sarah Kurtz, chair

Professor Gerardo Diaz

Professor Catherine Keske

Professor Roland Winston

2022

This dissertation by Jordyn Brinkley, titled “The Integrated Compound Parabolic Concentrator (ICPC): a low cost, non-tracking, solar thermal collector for low carbon process heating up to 150˚C” is approved, and it is acceptable in quality and form for publication on microfilm and electronically:

Sarah Kurtz, Chair	Date
Gerardo Diaz	Date
Catherine Keske	Date
Roland Winston	Date

University of California, Merced

2022

Dedicated to Randy Brinkley, my honest, hilarious, loving, and terrible driving brother. You are eternally missed.

Acknowledgements

The material described in this dissertation is based upon work supported by the U.S. Department of Energy's Office of Energy Efficiency and Renewable Energy (EERE) under the Solar Energy Technologies Office (SETO) Award Number DE-EE0008399. This dissertation was prepared as an account of work sponsored by an agency of the United States Government. The views and opinions of authors expressed herein do not necessarily state or reflect those of the United States Government or any agency thereof.

Chapter 2 of this dissertation was prepared as a result of work sponsored by the California Energy Commission as part of GFO-16-503 under contract # PIR-16-007. The Energy Commission, the State of California, its employees, contractors, and subcontractors make no warranty, express or implied, and assume no legal liability for the information in this document; nor does any party represent that the use of this information will not infringe upon privately owned rights.

Throughout my experience in grad school, I have received a great deal of support and assistance. To my committee: Prof. Sarah Kurtz, Prof. Gerardo Diaz, Prof. Catherine Keske, and Prof. Roland Winston, I want to express my gratitude for your guidance and support throughout the PhD experience.

I would like to thank my advisor, Roland Winston, for introducing me into solar thermal and nonimaging optic research. I would not be here in this moment without you pushing me into it, and I am forever grateful that you challenged me to do so. To Dr. Sarah Kurtz, I am incredibly grateful to have received your support and guidance throughout the years. You really have been my unofficial co-advisor, and I am glad to have experience learning from you.

My time in the Winston lab at UC Merced would be nothing without my colleagues, Bennett Widyolar, Yogesh Bhusal, Melissa Mitchell, Jon Ferry, Robyn Lukens, Lun Jiang, and Kaycee Chang. Thank you so much for all the support, guidance, and good times we've experienced throughout the years. What a ride it's been!

I would also like to acknowledge and sincerely thank the following people and organizations for supporting this work in different capacities:

- Justin aka "Texas Chainsaw", Brian, and Keith for all the welding consultations & good laughs
- APG Solar staff for all the consultations, brazing work, & equipment loans
- My step dad, Kenny Woods, for the expert support & teaching me how to braze Cu over the phone
- Matt & Melissa Mitchell for all the technical and emotional support throughout the years
- The Merced community for all the support and great experiences

This degree would not have been completed without the love and support of my loving parents, Deanna and Kevin Brinkley, step-parents, sister, grandmothers, family, and friends. I would like to acknowledge and thank my humbly patient housemates, Jocelyn and Donnoban, for putting up with me during the writing process.

I will forever cherish the grad school times in Merced spent with good people, building collectors, and melting in the valley heat.

Curriculum Vitae

JORDYN T. BRINKLEY
2102 Crestline Drive, Oceanside, CA 92054 | (818) 813-3463 | jbrinkley@ucmerced.edu

EDUCATION

University of California, Merced
Ph.D Environmental Systems **2017-May**
School of Engineering **2022**

University of California, Merced
B.S. Mechanical Engineering
School of Engineering **2012 -2017**

TEACHING EXPERIENCE

University of California, Merced

CE 193– "Civil & Enviro. Eng. Capstone"
Teaching Assistant: Assisted students in project managing for deliverables and deadlines, graded design review presentations and final design reports **F21-S22**

ENGR 57 – "Statics and Dynamics"
Teaching Assistant: Instructed weekly 50-minute discussion sections, held weekly office hours, homework/quiz/exam grading, proctored quizzes. **Spring 2021**

ENVE 160/ES 260 – "Sustainable Energy"
Developed homework assignments, proctored exams, and administered all grades. **Spring 2018**

ENGR 155 – "Engineering Economic Analysis"
Teaching Assistant: Held weekly office hours, administered all grades, proctored exams. **Fall 2017**

RELATED EXPERIENCE

UC Solar, University of California, Merced

Graduate Researcher **2017-Present**

- Developed thermal heat transfer model of solar-to-thermal efficiency including optical and thermal losses of a novel non-tracking evacuated solar thermal collector. Prototype includes work with minichannels, vacuum insulation, and nonimaging optics. Fabricated prototype 10 kW pilot array and set-up experimental plumbing test facility with data recording sensors for solar irradiance, flow, and temperatures. Conduct daily experiments to gain solar-to-thermal efficiency and daily energy generation to confirm thermal model. Report and present data and findings to the Department of Energy.

- Assembled and fabricated a novel CHP combined solar PV/T collector for low temperature heat and electricity generation for residential energy needs. Constructed a small module and conducted daily solar experiments to analyze daily solar-to-electricity efficiency and solar-to-thermal efficiency Developed a solar thermal and electricity generation heat transfer model, confirmed by experimental results. Drafted reports and presented results to the California Energy Commission.

UC Solar, University of California, Merced

Undergraduate Research Assistant **2015 – 2017**
Assisted graduate students with sponsored projects, data collection and analysis, and followed instructions from GSRs and post-docs.

Strategic Energy Innovations, University of California, Merced

Internship **Spring 2017**
Collaborated with MID representatives and UC Solar to develop educational classes, posters, and flyers for youth class to promote Renewable Energy, and took part in high school outreach to teach about renewable solar energy.

PUBLICATIONS AND PROCEEDINGS

Brinkley, J., Jiang, L., Widyolar, B., Hota, S.K., Bhusal, Y., Diaz, G. and Winston, R., 2020. Thermal, electrical, and cost study of advanced optical photovoltaic thermal system (ADOPTS). *Applied Energy*, *269*, p.115105.

Brinkley, J., Widyolar, B., Jiang, L., Bhusal, Y., Diaz, G., Palko, J. and Winston, R., 2020, August. Preliminary experimental results of a novel low cost solar thermal collector with integrated optics for desalination processes. In Nonimaging Optics: Efficient Design for Illumination and Solar Concentration XVII (Vol. 11495, p. 114950N). International Society for Optics and Photonics.

Brinkley, J., Jiang, L., Widyolar, B. and Winston, R., 2018, September. Flowline analysis of eténdue transfer of a wide-angle solar concentrator. In Nonimaging Optics: Efficient Design for Illumination and Solar Concentration XV (Vol. 10758, p. 107580K). International Society for Optics and Photonics.

Brinkley, J. and Hassanzadeh, A., 2017, September. Adaptive sensor-based ultrahigh accuracy solar concentrator tracker. In Nonimaging Optics: Efficient Design for Illumination and Solar Concentration XIV (Vol. 10379, p. 1037909). International Society for Optics and Photonics.

POSTERS

"Low cost dispatchable heat for small scale solar thermal desalination systems." Brinkley, J. Presented at the 2019 Solar World Congress in Santiago, Chile.

"Mid-Temperature Thermal XCPC." Brinkley, J.; Chang, K. Presented at the 2017 UC Solar Symposium at the California Public Utilities Commission Auditorium.

"Solar Tracking." Brinkley, J. Presented at the 2016 UC Solar Symposium at University of California, Davis.

MEMBERSHIPS AND SCHOLARSHIPS

Simon Family Foundation (2009-2017)
UC Merced Summer Bridge Program (2017)
Dan David Fellowship (2018-2020)
Edward Hildebrand Fellowship (2019)

Abstract

The Integrated Compound Parabolic Concentrator (ICPC): a low cost, non-tracking, solar thermal collector for low carbon process heating up to 150˚C

By Jordyn Brinkley
Doctor of Philosophy in Environmental Systems
University of California, Merced
2022
Committee Chair: Dr. Sarah Kurtz

With the recent IPCC report, the time to de-carbonize the energy sector and provide cost-competitive renewable technology is now! Using the most abundant source of energy, the sun, solar irradiance can be captured (through materials and optics) and converted to renewable energy in the form of low carbon emitting electricity or useable heat. The Integrated Compound Parabolic Concentrator (ICPC) is a simple, wide-angle, nonimaging optic that negates the need for tracking. The solar design process of module and array scale results of the ICPC are outlined containing the 3 fundamental steps: develop a system design, estimate system cost, and estimate system performance. Multiple design prototypes of the ICPC coupled with low cost aluminum minichannel absorbers were fabricated including: a low temperature, hybrid photovoltaic/thermal (PV/T) design for residential and commercial buildings, and a high temperature ICPC with vacuum insulation for solar heat industrial processes (SHIP) and solar thermal desalination. With solar PV's low cost and wide adoption into the electricity grid, the PV/T design does not seem to be ideal for low temperature applications in these end-use heat sectors based on modular performance and cost. Therefore, the thermal only collector solar design processes of the ICPC is highlighted with modular performance, and fabrication of a 12 kW array is analyzed to incorporate additional system losses that modular performance neglects. The ICPC, thermal only, module collector demonstrated instantaneous solar-to-thermal efficiencies of 72% ±4% at 43˚C, 60% ±4% at 120˚C, and 55% ±5% at 140˚C. The ICPC's 26.25 m2 array averaged daily efficiencies of 38%, and generated an average 65 kWh of thermal energy over an average span of 6.4 hours of active solar each day (producing average 2.5 kWh/m2-day at 38%). The array's annual thermal generation estimation of 784 kWh/m2-year estimates the cost of ICPC's delivered heat over operating temperatures of 120˚ at $0.0168/kWh. The array experienced 11% vacuum tube failure and about 5% solder connection failure. With further improvements in the thermal and manufacturing stages, the ICPC cost of levelized heat has the potential to be reduced to $0.015/kWh; making the ICPC a top cost-competitive challenger to high carbon-emitting fossil fuels.

The ICPC has been submitted to the DOE's solar initiative contest called "American-Made Solar Desal Prize: round 2", and won the first stage of prize ($50,000) and accepted to move on for stage 2 submission teaming phase. The four-stage competition was designed to accelerate the development of low cost desalination systems that use solar-thermal power to produce clean water from salt water. The phase 2 application has been submitted and awaits announcements (expected late April 2022)

Table of Contents

LIST OF TABLES

LIST OF FIGURES

LIST OF EQUATIONS

Chapter 1. Introduction to Solar Energy and Nonimaging Optics

1.1 *Introduction to Solar Energy*

This section covers the nuclear fusion reaction that produces solar radiation to emit from the sun's surface into all directions of the solar system. Along with the spectral irradiance behavior (terrestrial and extraterrestrial), the section introduces the capturing of solar energy for end-use. A summary of solar collectors is given with emphasis on the thermal producing technologies.

1.1.1 Solar radiation

At the center of our solar system lies, 'Sol', Earth's home star, a sphere of extremely hot gaseous matter with a diameter of $1.39*10^9$ m and an estimated density about 100 times that of water. The sun is about $1.5*10^{11}$ m from the Earth, and is the source of most energy on Earth. For example: fossil fuels are derived from biological matter fueled by solar, hydro is driven by solar evaporation, and wind is caused by solar induced thermal gradients.

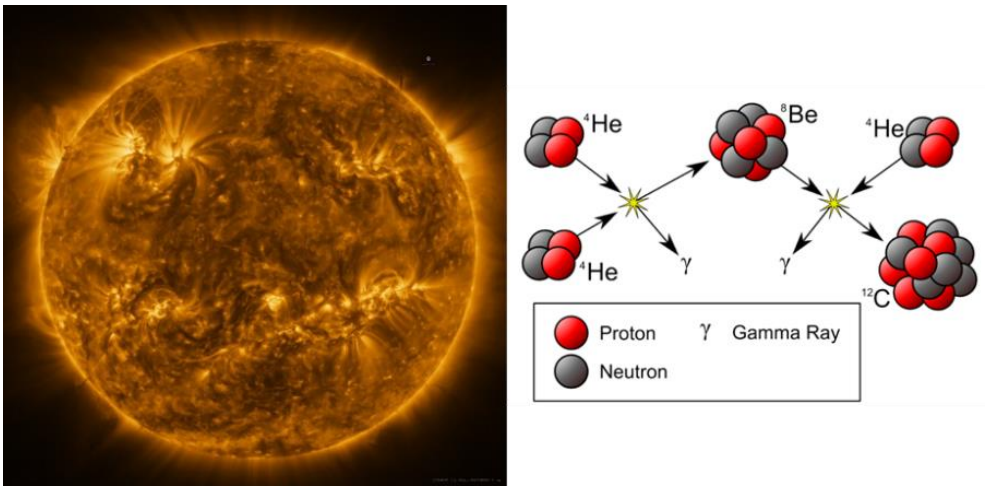

Figure 1: The sun in high resolution made up of a mosaic of 25 individual images taken on March 7th, 2022 by the Extreme Ultraviolet Imager (EUI) instrument [1] (Left) & Nuclear fusion reaction with gamma ray byproducts (Right)

This energy radiated by the sun is created as a product of the continuous fusion reaction in which hydrogen combines with its constituent gases as the 'containing vessel' to form helium and convert the loss of mass to energy (see fusion reaction in Figure 1). This energy is carried away by particles of light, known as photons, through the radiative zone of the sun into the convective zone. This produced energy is millions of degrees in temperature. This energy is transferred through the convective zone with hot plasma rise and fall, creating thermal processes to transport the heat to the outer layer of the sun, the photosphere. The photosphere, the source of most solar radiation, consists of strongly ionized gases that absorb and emit a continuous spectrum of radiation[2].

Although the temperature at the center of the sun is estimated to be 8-40 x 10^6 K, the sun has an effective outer blackbody temperature of 5762 K and a total energy output of 3.8 x 10^{20} MW from the fusion reaction, which is 63 MW/m^2 radiating outwards in all directions from the sun's surface [3]. However, only a small fraction of the total radiation emitted from the sun is intercepted by the Earth.

1.1.2 Solar constant and terrestrial radiation

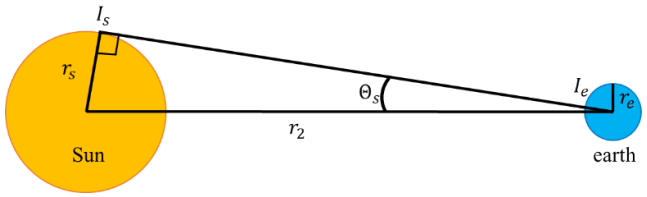

Figure 2: Geometry of sun and Earth positions for inverse square intensity

The radiation intensity at the Earth's upper atmosphere (extraterrestrial), I_e, can be determined using the inverse square law of radiation.

Equation 1

$$sin\,\Theta = \frac{r_s}{r_2}$$

Equation 2

$$I_s * 4\pi r_s^2 = I_e * 4\pi r_e^2 \rightarrow \frac{I_s}{I_e} = \frac{{r_s}^2}{r_e} \;\; OR \;\; \frac{I_s}{I_e} = \frac{1}{sin^2\Theta}$$

The solar constant, I_e, is the energy from the sun per unit time received on a unit area of surface perpendicular to the direction of propagation of the radiation at mean earth-sun distance outside the atmosphere[4]. The solar constant averages about 1373 W/m^2, and the radiation power density at the Earth's surface peaks average at approximately 1 kW/m^2, S. If the power was collected by absorbing it on a perfect blackbody, the equilibrium temperature, T, of the blackbody can be determined with Equation 3. Note, σ is the Stephan-Boltzmann constant of 5.67*10^{-8} W/m^{2}K^4. The estimated temperature would be 364K (91˚C), where water boils at 373K (100˚C).

Equation 3

$$S = \sigma T^4$$

Since the distance between the sun and Earth changes due to Earth's elliptical orbit, the power density variation, I, based on the day of year, n, can be determined with Equation 4. However, the variations are typically small.

Equation 4

$$\frac{I}{I_e} = 1 + 0.033\,cos(\frac{360(n-2)}{365})$$

With the solar constant being the peak power density of the blackbody radiation source of the sun at 5762 K (T_{sun}), the wavelength where the spectral irradiance is the highest, $\lambda_{b,max}$ (μm), can be calculated using Wein's law:

Equation 5

$$\lambda_{b,max} = \frac{2900}{T_{sun}}$$

The peak wavelength for the spectral curve is about 0.5 μm, which is demonstrated in Figure 3. This is in the midpoint of the visible spectrum. In comparison, if the blackbody temperature was represented as ambient temperature of Earth, which is about 300 K, the peak wavelength would lie in the infrared at about 10 μm. See Figure 3, right for visual representation and breakdown of the electromagnetic spectrum.

As the radiation, I, enters and passes through the atmosphere, light experiences a power reduction as it's absorbed, scattered, or transmitted through the particles that make up the atmosphere (i.e. air, water vapor, clouds, dust, ozone, and greenhouse gases). High absorption from particles like ozone, dioxygen, and water vapor change the spectral solar radiation by reducing infrared radiation(see annotations in Figure 3), and all introduce diffuse or indirect solar radiation (varying from the direct light path experienced at the extraterrestrial atmospheric surface.

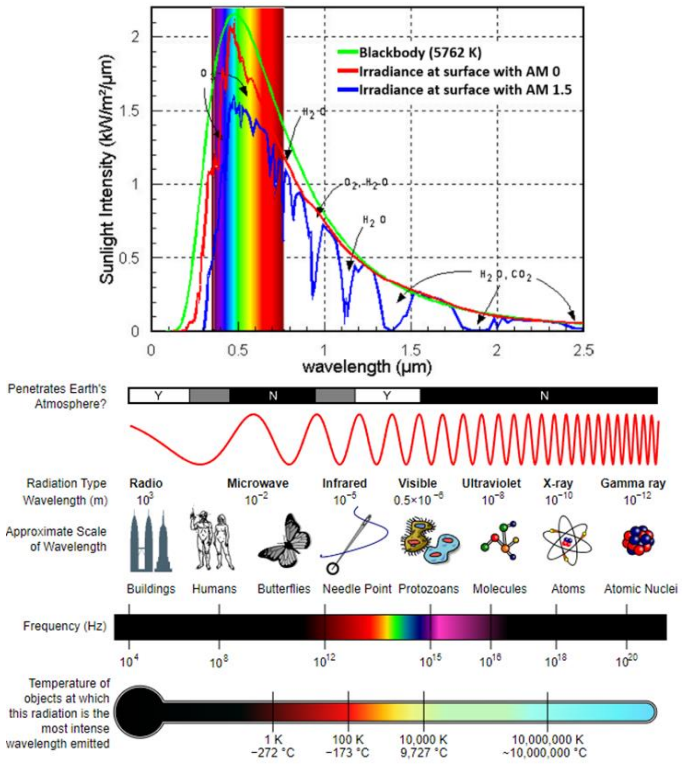

Figure 3: Solar Irradiance spectral distribution at Earth's surface as a blackbody (green), extraterrestrial with air mass of 0 (red), and terrestrial irradiance with air mass of 1.5 (blue). Note the visual wavelengths show with the VIBGYOR spectrum and the marked high absorption wavelengths from ozone (O_3), dioxygen (O_2), and water vapor (H_2O)[5] ***(Left)*** *& electromagnetic spectrum with properties, scales, and ranges [6]* ***(Right)***

The path length of the photons passing through the atmosphere normalized to when the sun is directly overhead (the shortest possible path length) is known as the air mass ratio. So, when the sun is directly perpendicular to the surface, the air mass is 1. The air mass (AM) is based on the angle from the vertical, or zenith angle, Θ_z. This equation assumes the atmosphere is a flat horizontal layer.

Equation 6

$$AM = \frac{1}{\cos \Theta_z}$$

This equation is only an estimation and neglects the curvature of the Earth, therefore a more accurate estimation of air mass is the following.

Equation 7

$$AM = \frac{1}{\cos(\Theta_z) + 0.50572(96.07995 - \Theta_z)^{-1.6364}}$$

As mentioned, the particles within the atmosphere introduce diffuse radiation or indirect light. When determining solar irradiance on the Earth's surface, the total global irradiance, I_G, is the sum of the direct radiation, I_D, and indirect radiation, I_{ID}. The direct solar irradiance can be estimated as a function of air mass and height above sea level with Equation 8, where a = 0.14 [5].

Equation 8

$$I_D = 1.353 * [(1 - ah)0.7^{AM^{0.678}} + ah]$$

Sea level, h, is considered due to sunlight intensity increasing with height. The diffuse radiation is estimated to be 10% of the direct, so an estimation of the total global irradiance on Earth's surface is based on the calculations of direct irradiance using Equation 4, Equation 7, and Equation 8.

Equation 9
$$I_G = 1.1 * I_D$$

This variable represents the total available solar irradiance in units of W/m^2, that can be captured on the earth's surface for energy. However, the earth's rotation affects the angle of direct irradiance. If positioned at a fixed point on earth, the path the sun appears to follow moves through the sky. The positioning of the sun from that fixed position on earth will depend on time of year, time of day, and location on earth. The sun's path, from the northern hemisphere for example, rises in the east and sets in the west as the day passes from morning to night. Seasonally, the sun is in a lower position in the winter (23.5˚ below equator) and higher position in the summer (23.5˚ above equator). These seasonal positions follow the solar equinoxes and solstices (around the 21st of March, June, September, and December), where the sun meets the highest position in June, lowest in December, and lies on the equator twice a year in March and September (from the northern hemisphere example). To model the sun's angle to a fixed position on earth, requires latitude, longitude, day of year, and the time of day. Although there are multiple equations to calculate the solar position, advanced solar position calculators have been developed by private companies, university research institutes, and national laboratories[7]–[10].

Based on the solar position, the power density varies. For instance, if an absorbing surface was placed on the surface and angled perpendicularly to the sunlight, the power density on the absorbing surface is equal to the sunlight's power density. While the maximum power density of an absorbing surface is when the surface is perpendicular to the incoming sunlight, the radiation incident on a tilted surface can be estimated. This tilt of the absorbing surface will have maximum output when perpendicular to incoming incident radiation and will change tracking the elevation angle and tilt angle of the module. These estimations are used to determine the angle to tilt solar collectors to optimize the maximum output of an installed system.

Although the solar irradiance can be modeled based on the methods described above, a real value of the solar irradiance can be measured with pyrheliometers, pyrheliometric scales, reference photovoltaic cells, and pyranometers. In this dissertation, the photovoltaic reference cell and pyranometers were used. The most used instrument to measure solar irradiance is the Eppley precision pyranometer (PSP) which utilizes a thermopile detector, two concentric hemispherical optically ground covers, and temperature compensation results in temperature dependence of 0.5% from -20 to 40˚C [4]. The PSP measures global solar irradiance, I_G; global solar irradiance measures both direct and diffuse radiation.

1.1.3 Capturing solar energy

Through materials available and developed, solar irradiance can be captured and converted for end-use energy, like electricity and heat. Through photovoltaic (PV) solar capturing technology, these electronic devices directly convert sunlight into electricity. Solar cells are made up of materials that raise electrons as light is absorbed to a higher energy state and eventually from the cell into a circuit, and most solar cells use semiconductor materials in p-n junction forms. As the excited electrons generate a voltage across the cell and travel to generate a current for useable power in the form of electricity. The most common photovoltaic systems are silicon cells.

Chapter 2 explores a hybrid, photovoltaic thermal (PV/T) collector, which works as a basic PV panel to generate electricity, which also incorporates a thermal collection to capture actively "cool" the PV cells. This transfers the heat away from the cells and can be designs to use that heat for low

temperature applications, such residential water heating. These hybrid collectors capture solar radiation and transfer the energy to both useable electricity and heat.

Another form of energy that can be captured by solar irradiance, is the solar radiation itself. Solar thermal technologies are designed with the purpose of capturing the solar radiation with an absorbing material, and transfer the heat within a heat transfer fluid (HTF); transferring the radiant energy into useable heat. Examples of heat energy uses include a range of technologies for low temperature like water heaters to high temperature industrial or chemical processes and turbine powering.

Solar thermal technologies can be generally distinguished between tracking and stationary/non-tracking collectors. A stationary collector's aperture area (area where light enters the collector) is the same plane and surface as the absorber (i.e. flat plate collectors). The need for tracking comes from the acceptance angle of the optical collector. The function of solar collectors is to direct sunlight onto an absorbing material. Some designs have a larger aperture area directed onto a smaller absorber area. These optical solar collectors use mirrors or lenses in order to 'concentrate' sunlight from the larger aperture area onto the absorber surface area. These concepts and technologies are further described in Chapter 3. A detailed summary of solar thermal collectors can be found in [11].

It's important to note that the term "concentrator" in the solar field has two different definitions. Some scientists believe a solar collector can be classified as a concentrator if the concentration ratio is >1. However, the more recent classification of concentrators are optical designs that focus, or 're-direct', light from one aperture area onto an absorber area. Throughout this dissertation, the term concentrator will follow the latter definition.

1.1.4 Motivation for solar energy

The most recent Intergovernmental Panel on Climate Change (IPCC) AR6 WG III report determined the global break-down of 59 $GtCO_2eq$ total emissions as follows: 5.6% from buildings, 15% transport, 22% agriculture, forestry, and other land use (AFOLU), 10% other energy, and 23% electricity & heat, and 24% from industry. The main contributions to the net anthropogenic GHG emissions for 2019 showed carbon dioxide (CO_2) contributing 64%, and 18% from methane (CH_4). Carbon dioxide is a common emission from natural gas combustion.

Industry sector emissions have been growing faster since 2000 than emissions in any other sector, driven by increased basic materials extraction and production. GHG emissions attributed to the industrial sector originate from fuel combustion, process emissions, product use and waste, which jointly accounted for 14.1 $GtCO_{2\text{-}eq}$ or 24% of all direct anthropogenic emissions in 2019. Industry is a leading GHG emitter – 20 $GtCO_{2\text{-}eq}$ or 34% of global emissions in 2019 – if indirect emissions from power and heat generation are included [12].

The science behind these reports clearly demonstrate that drastic changes need to occur in current infrastructures of energy generation, food production, and water capturing in order to limit the global temperature mean rise due to greenhouse gas (GHG) emissions. Methods to reduce annual emissions into the atmosphere are the main key in maintaining the global temperature mean.

In order to do so, infrastructure changes to renewable and low carbon emitting technologies should be taken. Changes to the energy sector are already being steered with in the electricity sector with hydro, wind (onshore and offshore), solar PV, and nuclear. The transportation sector is seeing an increase in electrical vehicles and even advancements in fuel cells. The energy end-use 'heat' sector is majority from industrial demand and does not seem to have a lot of renewable options that can

supply the heat at specific operating temperatures (2/3 of heat demand for all industrial processes lies below 300˚C[13]). See Chapter 3 introduction for further motivation.

Along with the energy infrastructure, low carbon emitting heat is needed to increase wastewater capturing, through thermal desalination for high salinity brine waste from industry and agriculture. This concept is known as solar desalination and is a fast up and coming topic that is being heavily investigated and invested in by both private and government identities.

1.2 *Combining Nonimaging optics, vacuum insulation, and minichannels*

When considering the design of a solar collector, the application must first be determined to determine an ideal optical design. Therefore, a simple summary into the concept of nonimaging optics is summarized here. Minichannels are also introduced as a possible absorber for solar thermal applications; these mini or micro-channels, have been established within the electrical and automotive industry as active cooling mechanisms. With the incorporation of a simple optic derived from nonimaging optic principles and minichannel heat exchangers which are previously established in the electronics and automotive industries, a solar thermal collector design is investigated lightly as a hybrid (PV/T), low temperature, and a higher focus on a thermal only, vacuum insulated, medium temperature (up to 150˚C) design.

1.2.1 Nonimaging-optics: what the heck is it?

The need for nonimaging optics is to increase the concentration on radiation collection to obtain higher temperatures. If limited by peak approximation of 1 kW/m^2 on earth's surface, the maximum temperature obtainable (from Equation 3) is about 364K (91˚C), where water boils at 373K (100˚C) at atmosphere. As recently mentioned, most industrial temperature demands lies below 300˚C, therefore concentration is required.

Nonimaging optics is simply optics without imaging (Figure 4) and the theory of maximal efficiency radiative transfer. The main difference is how the sources are treated. Imaging optics is the optics of point sources, while nonimaging is the optics of extended sources. Extended sources have a boundary. This simplest boundary is a line. Extended sources have regions of light and region with no light. The sun is not a point source, but rather an extended source. The idea of extended sources was the first innovation that made up nonimaging optics.

It is axiomatic and algorithmic based; however, the subject depends much more on thermodynamics than on optics. Nonimaging optics established a limitation in imaging optics for theoretical maximum concentration.

Equation 10

$$C_{max} = \frac{1}{sin^2\Theta}$$

With imaging optics, the maximum concentration ratio is limited to 1/sinΘ, however the theoretical concentration ratio based on nonimaging optic principles becomes Equation 10 (see Appendix A for details).

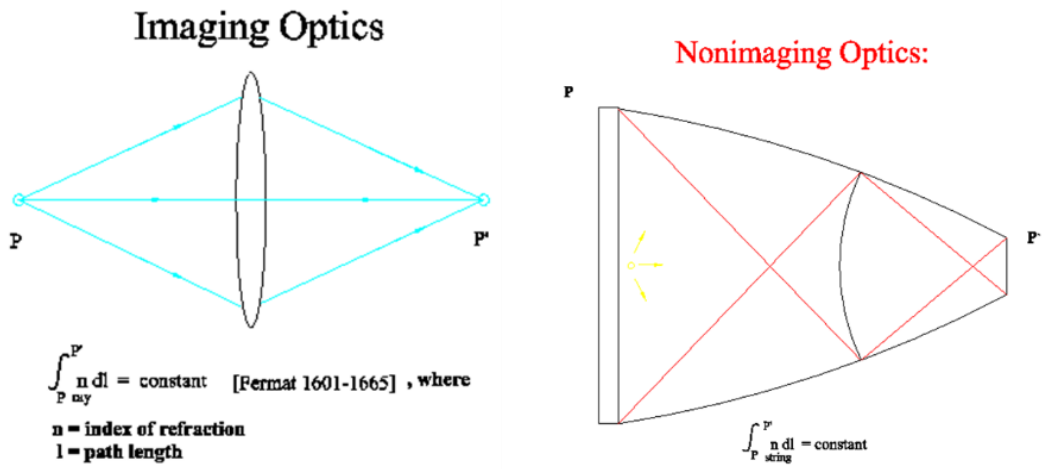

Figure 4: Imaging Optics compared to Nonimaging Optics using Fermat's principles for rays and strings

In its simplest form, the 'string method' could be used to derive a nonimaging optic based on the absorbers shape and dimensions. This method will develop a geometrical shape (to be made from reflective material and act as a mirror) that will capture all incoming light (direct and diffuse) that enters the aperture area (as long as the light is within the collector's designed acceptance angle), and concentrate or redirect that light using the geometrical mirrors onto the absorber surface. Nonimaging optical principles develop optics that accept all light based on the designs acceptance angle to transfer radiation negating the need to direct an image, but only requiring redirection of the radiation. A step by step instruction manual of the string method for a flat CPC can be found in Appendix B [14].

But, what does nonimaging optics do? What is nonimaging optics really? Well, in simple, the general perspective, including the founder's, of these questions are continuously changing. The first book's "Optics of nonimaging concentrators" publication was in 1978 by W.T. Welford and Roland Winston, and stems from a not so simple combination of geometrical optics and thermodynamics. Nonimaging optics is a new field of study, with only a handful of researchers investigating it since its establishment. The founding father of nonimaging optics himself would tell you that he doesn't know how it works, and religiously quote, "it just works." With that mentality, the majority focus for this field is application.

1.2.2 Minichannels' debut into solar

The theoretical maximum concentration is limited by thermodynamics; however, the solar-to-thermal efficiencies of current commercial solar thermal technologies can still be improved. Specifically, thermal efficiency improvements are needed to minimize thermal resistance within the solar collector design to improve thermal generation and in turn, lower levelized costs of heat. The goal is to design solar collectors to meet as close to the theoretical maximum as possible and produce low cost thermal energy, and that is done through design improvements within the components that make up the collectors. An excellent candidate for improvement being the absorbers that absorb the thermal radiation and transfer the heat through conduction and convection into a working HTF.

Common absorber designs consist of concentric round tubes in counter flow with a u-shaped tube or copper tube heat pipes. These are used in typical collectors, like evacuated tube collectors. Other absorbers used incorporate copper tubes or heat pipes welded to copper or aluminum fins to conduct the radiation that is absorbed on the fin surface to the copper tube carrying the heat transfer fluid.

An up-and-coming heat transfer technology known as minichannels are debuting in the solar thermal applications. However, mini or microchannel have been famously established as active cooling heat exchangers for auto-motives, electronics, and even air conditioning. For the solar thermal market, a study comparing the thermal performance of a minichannel based solar collector and standard U-shape round tube collector demonstrated slightly better performance in the minichannel collector with an average outlet temperature of 0.2˚C higher and 4.7% higher efficiency (at 180˚C, [15]) than the standard round tube collector. Another study comparing these two types of collectors with different collector designs found the increase in heat transfer area and the decrease in absorber resistance with minichannels demonstrated increase in efficiencies over all ranges of mass flow rates of the HTF[16]. Another study comparing daily performance of a minichannel flat plate collector to a conventional copper flat plate fin with tube collector showed an average increase in thermal efficiency of 13% and higher energy collection throughout the day for the minichannel collector[17].

With the goal to develop a solar system to compete with competing fossil fuels performance per unit cost, minichannels made with inexpensive and high thermal efficiency materials become an ideal candidate for solar thermal absorbers.

*1.2.3 **Introducing the ICPC***

This dissertation will demonstrate multiple designs of the nonimaging, non-tracking integrated compound parabolic concentrator, also known as the ICPC, coupled with minichannel absorbers to capture solar energy for useable heat. These designs included both an advanced optical photovoltaic thermal system (ADOPTS) and a lowcost, high efficiency thermal only system.

Each design was modeled, prototyped, and tested at the University of California, Merced's Castle Facility. The following chapters will communicate the solar design process for both the hybrid and thermal only systems. The solar design process, contains 3 fundamental steps and summarized as:

- Step 1. Develop a system design
- Step 2. Estimate system cost
- Step 3. Estimate system performance

Step 1 of the ICPC design process is defined in Chapter 3. Step 2's cost analysis is estimated in Chapter 4.4, and Step 3 is discussed in Chapters 4.1-4.2. With the solar design process results, the solar system can be compared to competing systems (i.e. fossil fuels) based on the performance per unit cost[18]. As mentioned in previous sections, the highest competitors for solar thermal systems would be the current infrastructure of low cost fossil fuels. In this dissertation, the levelized cost of heat (LCOH) is used to compare different heat generating technologies, which can vary with location, collector materials, and economic parameters. Solar thermal systems are not widely adopted yet within the heat sector, and need to establish longevity with demonstrations through viable applications. Additional demonstrations are needed in order to further understand the system cost and additional performance losses throughout the system and loads. To effectively penetrate the heat energy market, a solar collector must be fully researched and developed into a commercial and quality technology. With the goal of de-carbonizing the energy sector, it's important to note that the competing technologies are not other renewables; the competition to beat currently within the energy sector are high carbon emitting energy sources (i.e. coal, natural gas, etc). Therefore, in order to compete and, ideally, replace the current fossil fuel infrastructure, a low cost quality solar thermal collector is needed.

Although the hybrid design of the ICPC was thoroughly analyzed, the thermal only design of the ICPC is proving to be the ideal design system. Due to the dramatically low costs and mass installation, residential or low temperature thermal energy needs seem to be prospering in the electrification movement. However, the ICPC has a larger energy demand market in the higher temperatures and industrial energy demand needs, which is further described in Chapter 4. Therefore, this dissertation will have a higher focus on the thermal only producing ICPC design.

Chapter 2. Thermal, electrical and cost study of advanced optical photovoltaic thermal system (ADOPTS)

Note: *This chapter is a stand-alone paper published in Applied Energy Journal* [19].

Citation: Brinkley, J., Jiang, L., Widyolar, B., Hota, S.K., Bhusal, Y., Diaz, G. and Winston, R., 2020. Thermal, electrical, and cost study of advanced optical photovoltaic thermal system (ADOPTS). Applied Energy, 269, p.115105.

Abstract: In this paper, the Advanced Optical Photovoltaic Thermal System (ADOPTS) solar collector was thoroughly tested and analyzed in performance and cost analysis. The ADOPTS collector integrates optics within the PV/T device to enable geometric concentration, as well as a protection of the solar cells from the elements using the same encapsulation. The rooftop or façade mounted photovoltaic/thermal (PV/T) collector provides a low cost, two-in-one solution for residential/commercial hot water and electricity needs, while also providing a renewable energy option to reduce annual greenhouse gas emissions. The ADOPTS collector can provide 150 W_{el}/m2 and 400 W_{th}/m2, and prevent a total of 3916 kg of CO_2/m^2 (or 4.3 tons CO_2/m^2) over a 20-year period. The collector provides a low cost option that delivers both heat and electricity for single or multifamily homes and commercial buildings to compete with current commercialized PV and thermal systems, while simultaneously preventing CO2 emissions and reducing the need for natural gas.

Keywords: *Photovoltaic/thermal (PV/T); solar hybrid; solar PV; solar thermal; residential solar; nonimaging optics; ADOPTS*

2.1 *Introduction*

With rising sea levels, diminishing nonrenewable sources, increasing climate temperatures and increasing energy demands to maintain a growing global population, the need for renewable technologies that can reduce greenhouse gas (GHG) emissions is becoming more popular, particularly in California. California is the fifth largest economy in the world, and a continuous leader in environmental solutions and motivator to others. However, only half of California's electricity comes from zero-carbon emission sources such as nuclear, hydropower plants and other renewable sources. The state has an aggressive goal of 100% clean energy in electricity by 2045. At the same time, energy need in the form of heat remains unaddressed across the industrial, commercial and residential sectors. Solar photovoltaic (PV) and solar thermal could be combined together to make a hybrid collector called a photovoltaic thermal (PV/T) system, which consists of solar cells and solar thermal components to generate both electric power and heat [20] in a single module. The PV/Thermal solar collector has the advantage of serving both needs with a single system [21]. However, the cost of such systems remains high due to its material and assembly cost. Our effort in this project aims to reduce the cost of the heat transfer element by integrating advanced optics with the encapsulation envelop of the solar cells. In this way we can take advantage of both the electricity and heat generated from a single device at a lower cost. A hybrid PV/T reduces the cost of the system from an installation point of view when compared to having a PV system side by side with a thermal system. When using two separate systems to provide residential electricity and heating, there will be two separate installation costs (one installing a PV system, the other installing a solar thermal system) along with only allowing half the roof space area for each system: taking note that installation is one of the highest costs for solar technology.

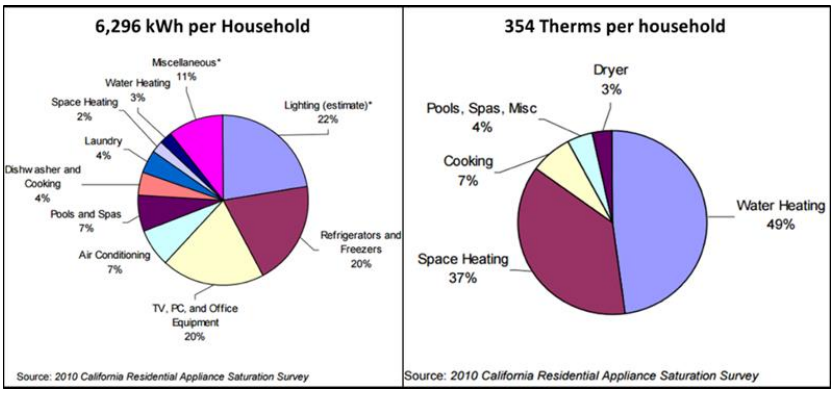

Figure 5: 2010 California residential appliance survey

According to the published results in Figure 5, main uses of residential heat are water and space heating. The heat load of natural gas to electrical usage ratio is ~1.7 to 1 (~10 MWhth to~ 6 MWhel), meaning the demand for thermal is higher than electrical for residential energy needs. By developing low cost solar hybrid collectors, California's residential dependence on natural gas for electricity and heat can be reduced or eliminated.

In this type of hybrid collector, the solar cells convert about 20% of incoming solar energy to electricity; the rest is converted to heat, which is collected by the thermal absorbers underneath the cells. Thus, by combining the two separate systems into a single system through an integrated approach, this hybrid technology minimizes the land requirement, and improves the efficiency of solar energy conversion. PV/T can also reduce the greenhouse gas (GHG) emissions. Additionally, the system has the potential of being significantly more economical, particularly when used as Building Integrated (BI) systems [22]. These systems have been reported to have the potential to reduce the GHG emissions 32% more than PV only systems [23].

Huide et al. [24] performed a comparative study by investigating the simulation model of individual solar thermal and PV collectors, and that of the hybrid PV/T systems for three different cities with experiments to validate the simulated model. The PV/T systems were potentially the best energy saving options for energy consumption in buildings, particularly in crowded urban areas with limited installation space. Recently, Guarracino et al. [25] presented the test procedures of PV/T collectors under real weather conditions in steady state and dynamic conditions, and investigated the effect of glass cover and quality of thermal contact between the PV cells and absorber. The results showed that a poor thermal contact can lead to a significant deterioration in thermal performance, and the addition of a glass cover improves the thermal efficiency. However, the addition of a glass cover causes electrical performance losses, depending on the glass transmittance and solar incidence angle [26]. Herrando et al. performed techno economic analysis and optimization of the PV/T collectors for domestic applications to fulfill 60% of thermal and electrical needs in Athens (14m2), Zaragoza (17m2), and London (12m2) [23]. The payback period for Athens and Zaragoza was found to be 15.6 years and 11.6 years respectively. The uncovered flat plate (water based) PV/T collectors, that account for 72% of the global PV/T market, would cost $360 /m2 as per a 2018 price survey (de Keizer et al., 2019; [27]). The major bottleneck to integrating the PV/T systems into homes is the systems' economic viability. Currently, existing solar PV/T systems fail to penetrate the market due to their high costs with average module cost of $\$2/W_{DC}$ [28]; stand-alone PV panels have a reported module cost of $\$0.22/W_{DC}$ [29]. Table 1 below summarizes the current commercialized PV/T systems on the market.

Company / Author	Collector	Type	Concentration	Aperture Area (m^2)	$\eta_{0,th}$	$\eta_{0,el}$
Absolicon [30]	x10 PVT	PTC	17.8X	10.37	0.55	0.07
Chromasun [31]	Hybrid MCT	cLFR	20X	3.50	0.59	0.08
J. Coventry 2005 [32]	CHAPS	PTC	37X	1.875	0.64	0.11
DualSun [33]	DualSun Spring	FPC	1X	1.65	0.47	0.15
Solarus [34]	PowerCollector	CPC	1.5X	2.21	0.64	0.11

Table 1: Summary of commercial PV/T collectors

At this moment, the conventional PV/T technology has to be subsidized with effective rebates or benefits to the end users. Air/ or water-based PV/T systems are the most commonly used PV/T technologies, but their heat removal effectiveness is lower. Refrigerant based PV/T systems are still in research stages; however, they could achieve higher efficiencies than air/water-based systems. Relatively new PV/T technology using heat pipes have better heat transfer from the solar cells to the working fluid, and have been found to reach maximum electrical efficiency and thermal efficiency of 10% and 58% respectively. However, the cost of heat pipes and the effective control of heat pipe performance has been a challenge [26].

In this research, a team has designed, prototyped, and extensively tested the Advanced Optical Photovoltaic Thermal System (ADOPTS) over the course of two years, resulting in a low cost and highly efficient heat pipe based PV/T system that can be used for domestic or commercial water heating, electricity source, and space heating. This proposed hybrid collector consists of glass tubes integrated with nonimaging optics, aluminum mini channel heat pipes (for thermal energy collection) sandwiched by commercially available solar cells (to generate electricity). By incorporating a simple optical design with a low concentration ratio, this collector avoids the need for tracking, leading to reduced costs compared with tracked systems. The material choices, such as: commercial cells, glass tubes, aluminum absorbers, and silvering chemical treatment on the tubes, minimize the module costs and create a cost competitive collector compared to other PV/T's requiring costlier materials. With the prototyped design, the ADOPTS collector demonstrates competitive overall (electrical and thermal) efficiencies with the current commercial PV/T systems [results shown in Chapter 2.5.3].

When comparing the proposed solar hybrid collector to PV and thermal separate side by side systems, the proposed ADOPTS solar collector benefits by: producing similar electric and thermal output, while only requiring half the roof space, and achieving a cheaper option than installing two separate systems. Also, by combining the two systems into one, the installation cost, a major component of residential solar system cost, is reduced.

2.2 *Design*

The proposed ADOPTS design is a low cost, highly efficient solar PV/T collector that can produce both electricity and thermal heat up to 65˚C. The hybrid collector (shown in Figure 6) consists of a glass tube (2 m long, 70 mm outer diameter, 2 mm thickness) with the bottom half coated with a reflective silver coating, and a thermal absorber with silicon solar cells attached by double-sided tape to the top and bottom surfaces. The glass tube will provide protection for the absorber and solar cells from the environment. Simultaneously, the glass tube acts as a substrate for the reflective silver coating. Therefore, the glass tube serves as both the protective housing for the device and part of the optical concentrator. By also using the tape to secure the solar cells onto the heat transfer element, the heat can be harvested as the electricity is being generated. The glass tube is rounded and closed on one end, while the other end is shaped to have screw threading in order to be coupled

with an aluminum cap, similar to a mason jar. A low cost minichannel heat pipe (2 m long, 30 mm wide, 3 mm thick) was incorporated as the thermal absorber with interdigitated back contact silicon solar cells mounted on both sides. For the absorber, 1.8 meters of the heat pipe lies within the glass tube, while the remaining 0.2 meters is used in the manifold outside of the glass tube.

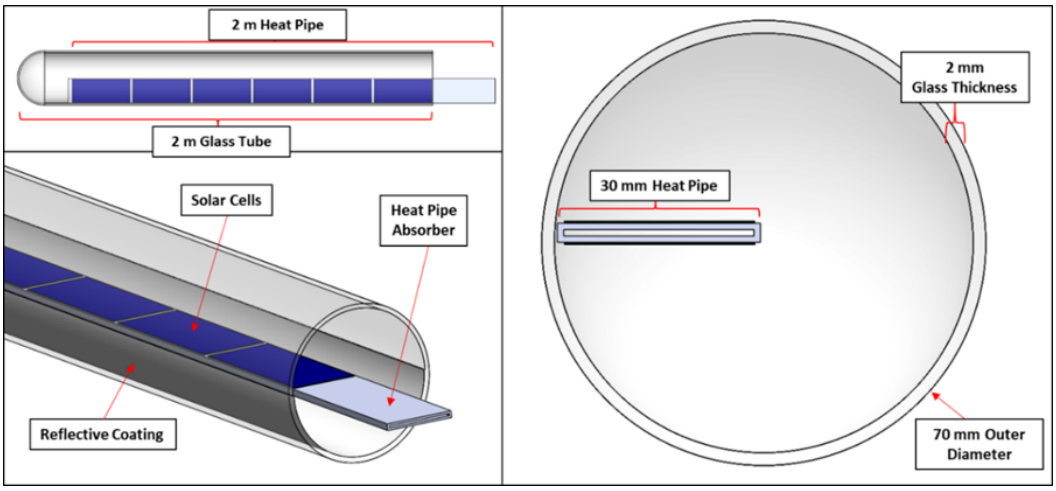

Figure 6: ADOPTS design and dimensions

For each single collector, there are two sets of 13 solar cells connected in series (increasing the voltage) on the top and bottom absorber surfaces; the two strips on the absorber were then wired in parallel (almost doubling the current), creating an efficient photovoltaic/ thermal (PV/T) collector. In order for the commercial solar cells to fit the absorber, the solar cells were sent to be professionally cut. See 'Results' section for further description.

Here, a new, recently commercialized heat pipe design is used as the heat transfer element. The heat pipe consists of low cost aluminum minichannels with internal "webs" in their cross-section to improve the structure integrity inside (see Figure 7). About 1.8 meters of the heat pipe sits inside the glass tube, known as the 'Evaporating Section', which is heated by the sun. The acetone then goes through a phase change and carries the heat up to the top of the heat pipe ('Condensing Section'). With this newer form of a heat transfer element being developed in recent years, the heat pipe has potential to grow and adapt to meet the solar thermal industry needs. For more on recent solar applications utilizing heat pipes, see [35].

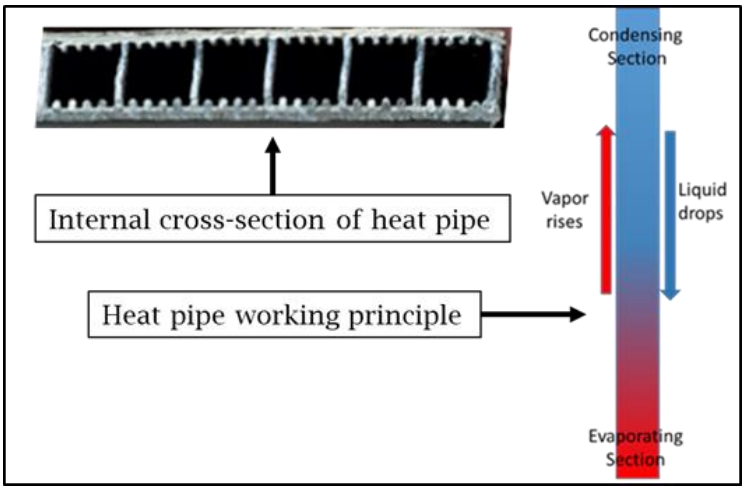

Figure 7: Heat Pipe cross-section

To pull the heat from the absorber, two aluminum minichannel manifolds (80 mm wide, 3 mm thick, 24 channels) are clamped on the top and bottom of the 'Condensing Section' of the heat pipes. A heat transfer fluid then flows through the minichannel manifold, pulling heat off the heat pipe condensers through conduction and convection. The minichannel manifold and heat pipe array are later demonstrated in Figure 14 shown in the 'Assembly' section. An array of a total of 10 hybrid tubes was tested.

2.3 *Optical and Thermal Simulation*

An optical simulation was performed using a proprietary Monte Carlo Ray Tracing (MCRT) software. In this software, a 3-D model of the design was built and simulated with a light source to define the geometric efficiency (ηgeo) and the optical efficiency (ηo). The geometric efficiency assumes perfectly ideal material properties in order to determine only the effects of gap loss (the loss associated with the light rays missing the absorber) and orientations of the absorber; it can also be used to make a first order approximation of the optical efficiency (which is highly impacted by the material properties). Both efficiencies were analyzed to quantify the ADOPTS optical performance. Due to the fact that the light source has a parameter that can be tunes to control the parallel light it emits, a detailed study can be performed regarding the raytracing results under different configuration of the sun's positions. In this way, the simulation generates the collector's optical efficiency under different incident angles of light at different orientations (also known as the incident angle modifier, or IAM) to determine the optical effects of a non-tracking system. For more on IAM's of solar collectors [36]. Figure 4 demonstrates the designs built in the ray tracing software.

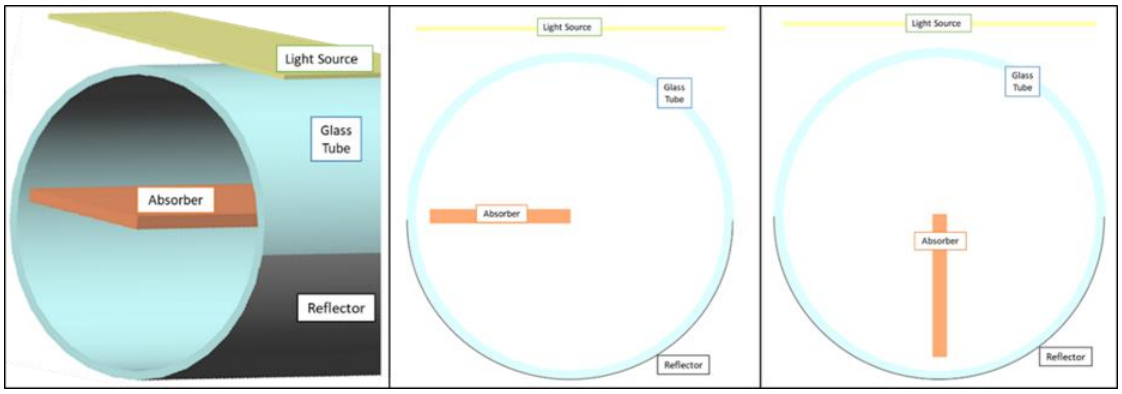

Figure 8: Side view of horizontal configuration (left), front view of horizontal configuration (middle), & front view of vertical configuration (right)

Two orientations, horizontal (middle) and vertical (right), were analyzed with ray tracings in order to determine the optimal placement of the absorber to maximize the collector's optical efficiency. To demonstrate the effects of gap loss, a 30 mm wide and 32 mm wide thermal absorber were simulated. These variations in width yield different results for geometric efficiency, optical efficiency, and the IAM as a result of gap loss. The following optical properties were assigned to the components of the hybrid collector and used in the ray tracing simulations.

Component	**Optical Property**
Glass Tube Transmittance (τ)	$\tau = 92\%$
Reflective Coating Reflectance (ρ)	$\rho = 92\%$
Thermal Absorber Absorptance (α)	$\alpha = 95\%$

Table 2: Optical Properties of collector components

The width of the absorber can increase or decrease the geometric efficiency due to gap loss between the edge of the absorber and the inside of the glass tube; for example, if the absorber width is increased, the geometric efficiency would increase due to the decrease in gap size. The geometric efficiency is calculated for normal incidence with ideal optical properties (all properties set to 100%); an absorber with width equal to the inner radius of the glass tube provides a geometric efficiency of 1. The optical efficiency for the collector is calculated using optical properties (defined in Table 2) in the ray tracing simulation at normal incidence. The geometric (η_{geo}) and optical efficiencies (η_o) are tabulated in Table 3.

Orientation	**η_{geo}**	**η_o**
30 mm wide – Vertical	0.847	0.679
30 mm wide – Horizontal	0.876	0.712
32 mm wide – Vertical	0.939	0.738
32 mm wide – Horizontal	0.954	0.756

Table 3: Optical simulation results

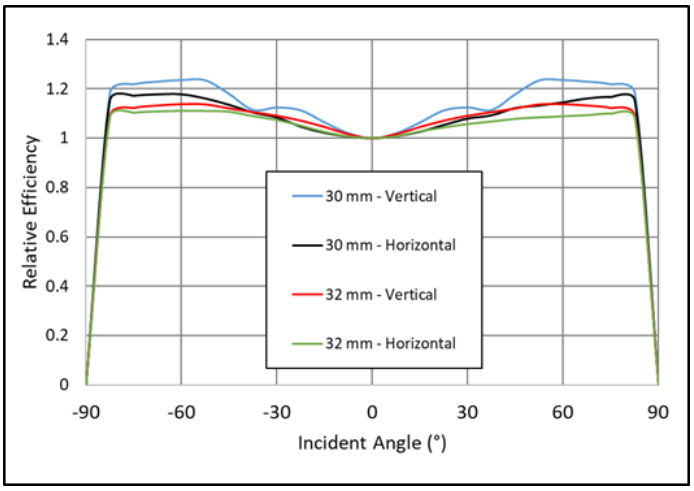

Figure 9: Incident-Angle Modifier (IAM) simulation results

The incident-angle modifier (IAM) demonstrates how the efficiency varies with the angle of incoming sun light, see Figure 9. The value of 1 in the IAM curve is relative to the optical efficiency at normal incidence. As the incident angle of light varies from perpendicular, the collector's performance changes. Due to the cylindrical shape of the collector, the efficiency increases in the morning and afternoon when the incident angles are $\pm 40°$ to $\pm 75°$ from perpendicular, providing good efficiency throughout the day.

From Table 3, as expected, the 32 mm wide absorber produced a higher optical efficiency at normal incidence, however from Figure 5, the 30 mm wide absorber provided relatively higher performance at non-normal incidence compared to the 32 mm wide absorber. Overall, the 30 mm wide heat pipe absorber was used in this prototyping stage because of its commercially availability, and the horizontal orientation was chosen due to the higher optical efficiency at normal incidence compared to the vertical orientation. The 30 mm wide absorber was lower cost, due to its commercial availability and minimal need for customization, which always adds additional costs.

For thermal performance, a performance model was constructed in Matlab with an energy balance analysis of the thermal and electrical efficiencies. The inputs to the model included an ambient (glass-wall) temperature (Tamb) of 25˚C (assumes worst-case thermal losses as would occur in a high-wind condition), global solar irradiance (G) of 1000 W/m2, and a heat transfer coefficient (h_{air}) of 5 W/m2K to quantify the convection in the tube. The aperture area (A_{ap}) and the area of the solar cells (A_{cell}) are calculated as follows, with l as length, *w* as width, and N as the number of solar cells:

Equation 11 $$\boldsymbol{A_{ap} = l_{coll} * w_{coll} = 0.1155\ m^2}$$

Equation 12 $$\boldsymbol{A_{cell} = l_{cell} * w_{cell} * N = 0.0488\ m^2}$$

It is estimated that the solar cells operate 10˚C temperature higher than the absorber, shown as Tcell, to account for the heat transfer between the cell and absorber through the double-sided silicone tape. The solar cell efficiency (η_{cell}) is calculated in Equation 14. Note, (β) -0.35% / ˚C is the temperature coefficient given by the manufacturer of the solar cells.

Equation 13 $$\boldsymbol{T_{cell} = T_{abs} + 10℃}$$

Equation 14 $$\boldsymbol{\eta_{cell} = \eta_{cell,STC}(1 - \beta[T_{STC} - T_{cell}])}$$

To determine the efficiency of the hybrid collector, the electrical and thermal power outputs are first determined. For the electrical output, the design of the collector provides different optical effects when comparing the top and bottom of the absorber. The bottom of the absorber has an additional reflection loss from the silver mirror finish, as noted in Equation 15 and Equation 16. Equation 15determines the electrical output from the top of the absorber ($Q_{elec,top}$), while Equation 16 is for the bottom ($Q_{elec,\ bot}$).

Equation 15
$$\boldsymbol{Q_{elec,top} = A_{cell} * \tau * \eta_{cell} * G}$$

Equation 16
$$\boldsymbol{Q_{elec,bot} = A_{cell} * \tau * \rho * \eta_{cell} * G}$$

The thermal output is calculated by taking the sum of the convective (Q_{conv}), radiative (Q_{rad}), and electrical powers; then, subtracting from the incoming solar power multiplied by the optical efficiency. The convective and radiative losses are determined in equations 9 and 10, while the thermal power output of the collector is calculated with Equation 19. The emissivity is assumed to be 0.6 from [37] measurements on silicon solar cells.

Equation 17
$$\boldsymbol{Q_{conv} = A_{ap} h_{air} (T_{cell} - T_{amb})}$$

Equation 18
$$\boldsymbol{Q_{rad} = A_{ap} \epsilon \sigma (T_{cell}^4 - T_{amb}^4)}$$

Equation 19
$$\boldsymbol{Q_{th} = G * A_{ap} \tau \left[\frac{1+\rho}{2} * \left(\alpha_{cell} + \left(1 - \alpha_{tape}\right)\right)\right] - Q_{elec,top} - Q_{elec,bot} - Q_{conv} - Q_{rad}}$$

In Equation 19, the incoming solar power on the collector is the product of the global solar irradiance, aperture area, and the optical efficiency. Due to optical losses, not all of the incoming solar power will be accepted by the collector. The analytical optical efficiency is determined by taking the product of the following assumed optical properties: reflectance of the silver mirrored reflector ($\rho = 0.92$), the absorptance of the solar cells ($\alpha_{cell} = 0.95$), absorptance of the double-sided silicone tape ($\alpha_{tape} = 0.95$), and the transmittance of the borosilicate glass tube ($\tau = 0.92$). Note that the actual optical efficiency was determined by the ray tracing results from the simulation. With all known losses and incoming powers, both the electrical and thermal efficiency of the collector are evaluated in Equation 20 and Equation 21.

Equation 20
$$\boldsymbol{\eta_{elec} = \frac{Q_{elec,top} + Q_{elec.bot}}{A_{ap} G}}$$

Equation 21
$$\boldsymbol{\eta_{thermal} = \frac{Q_{th}}{A_{ap} G}}$$

Figure 10 shows the simulated efficiency versus $T^* = (T_{abs} - T_{amb}) / G$, with electrical efficiency shown in green, thermal efficiency in red, and combined in blue. The combined efficiency is calculated by taking the sum of the thermal and electrical efficiency. The x-axis depicts T* which is a normalized temperature, and used to determine the collectors' expected performance for different environmental conditions. T* is calculated using the absorber temperature (T_{abs}), the ambient temperature (T_{amb}), and the solar irradiance (G).

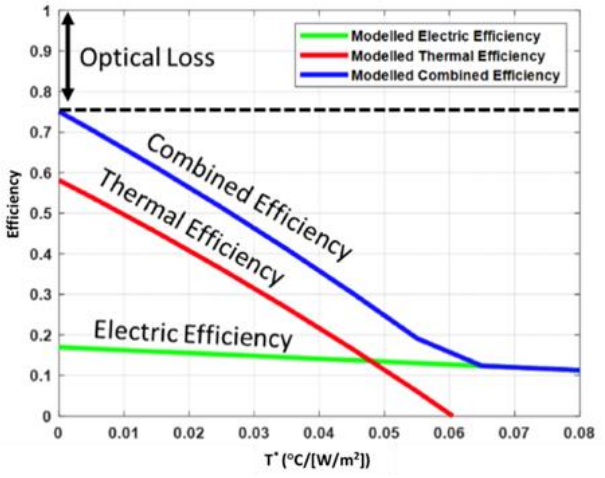

Figure 10: ADOPTS collector modelled efficiency

The simulated model above demonstrates an approximate electrical efficiency of 18% and thermal efficiency of 60% at T_{amb} of 25˚C. Around operating temperatures [T* = 0.035˚C/(W/m^2)], the electrical and thermal efficiencies can be expected at 14.5%$_{el}$ and 26.7%$_{th}$, resulting in a combined efficiency of about 41%.

2.4 *Assembly, Methodology, and Protocols*

After receiving the professionally cut solar cells, the collectors were assembled by the research team at the testing facility. The solar cells' efficiencies were tested and recorded both before and after the cutting process. After the collectors were constructed with the solar cells fully attached and functioning, the collectors were tested with a thermal load and the solar cell efficiencies were analyzed with an IV tracer at varying temperatures.

2.4.1 Assembly

The commercial Sun Power silicon solar cells were sent to a commercial facility to be laser cut into the dimensions shown in Figure 11 below. This was done so each solar cell can properly fit on the top and bottom surfaces of the heat pipe absorber.

The cut solar cells were then soldered in series with interconnections into strips of 13; a multi-meter was used to make sure the voltage was stacking correctly. Two strips were then taped to the heat pipe absorber with silicone double sided tape and wired in parallel to increase the current. Since the absorbers are placed inside a glass tube, the strips -- now in parallel -- were grounded to the bottom of the heat pipe absorber. At the top of the glass tube, two electrical leads were fed through the cap; one wire being the positive lead from the strips, and the other being the ground from the absorber (Figure 12; top).

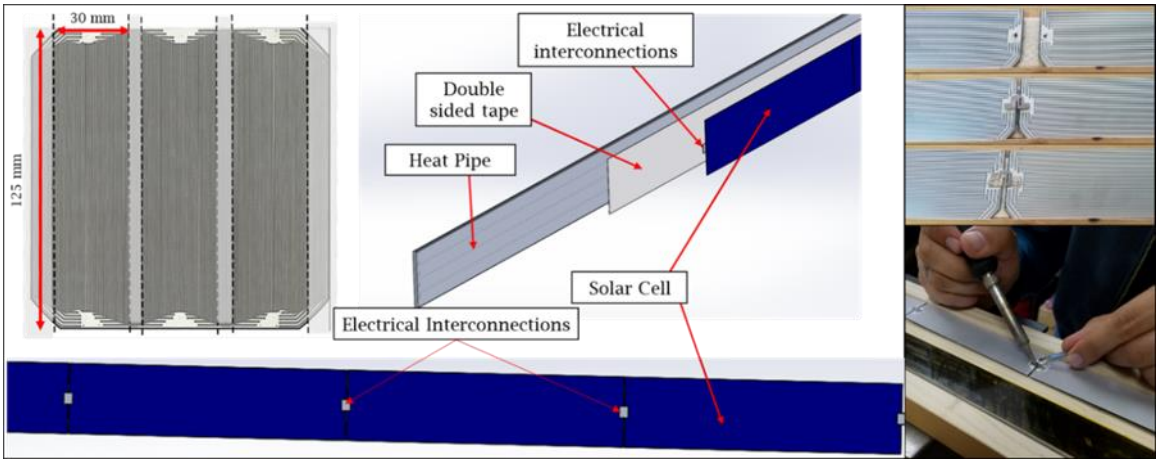

Figure 11: Solar cell cutting dimensions 9 (left) & application (right)

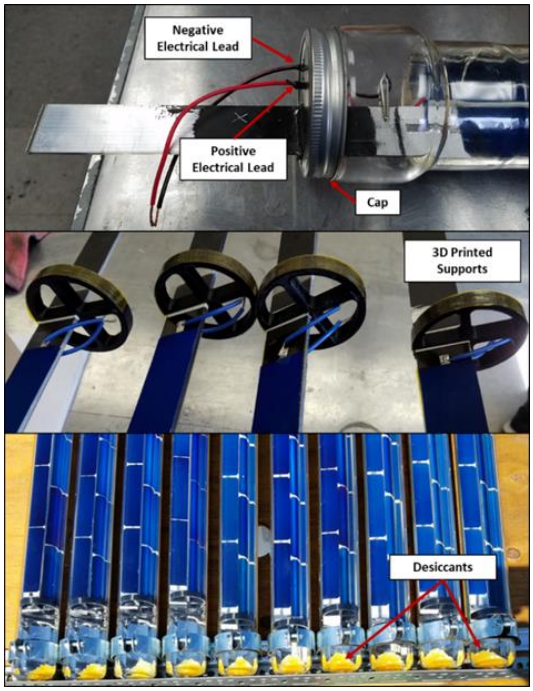

Figure 12: Cap with electrical leads (top), 3D-printed supports (middle), & Sorbead^{TM} Desiccants (bottom)

Notice in the top picture of Figure 12, the heat pipe absorbers were painted with a black paint coating in order to increase the absorptivity. The caps were provided by the glass tube manufacturer and holes were drilled into the cap for the two electrical leads and the absorber. A commercial epoxy was used to seal the components to the cap. Using a 3D Printer located at the testing lab facility, 3D printed supports were designed to hold the weight and keep the orientation of the absorber inside of the glass tube (Figure 12; Middle). Sorbead TM Orange Chameleon BASF desiccants were added to the bottom of the glass tube (Figure 12; Bottom). The inside of the glass tube was then filled with Argon to limit the convective heat loss from the hot absorber to the glass tube. The heat transfer coefficient is about 2/3 that of air (Figure 13). By incorporating the desiccants, any remaining moisture was removed to minimize thermal losses inside the collector.

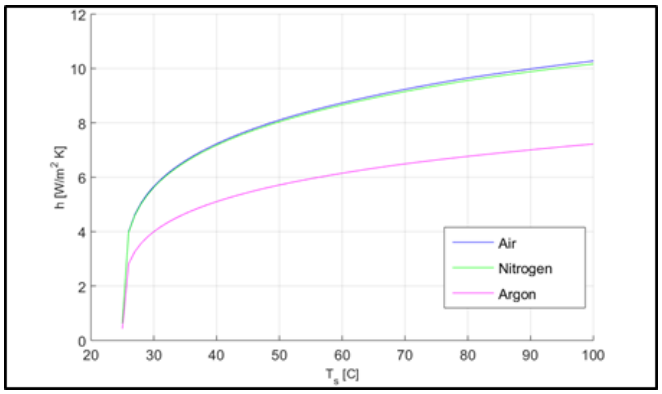

Figure 13: Gas convective heat transfer coefficient

After ten fully functioning collectors were assembled, two minichannels sandwiched the ten heat pipe condenser areas (Figure 14). As shown in the figure, the heat transfer fluid is pumped into the top minichannel manifold and redirected through the bottom manifold. As the heat-transfer fluid (HTF) flows, it extracts the heat from the condenser section of the heat pipes (previously mentioned in Figure 7). The water is circulated through the manifold and the HTF's extracted heat is used with a specific solar water heater (described in the '3.4.2 Methodology' section.)

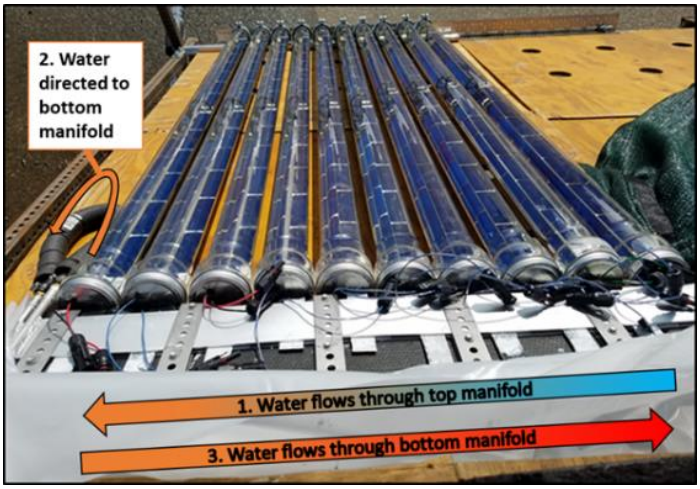

Figure 14: Minichannel manifold with clamping mechanism

While assembling the manifold, thermal grease was added to the condenser areas of each absorber, and a clamping mechanism was installed and tightened to maximize contact between the condensers and manifold. Poor contact between the condensers and manifold can result in large drops of thermal efficiency, overall affecting the electrical efficiency as well due to increased temperatures.

*2.4.2 **Methodology***

Multiple experiments were conducted before the full array was tested. To quantify the electrical performance, multiple IV curves were recorded of the cut solar cells in varying configurations on sun with an IV Tracer. These experiments are discussed in Section 3.5.1. Before analyzing the array performance, single tubes were tested on sun. Individual tubes were tested by circulating water into small heat sinks, which were attached to the condenser area of the heat pipes. These experiments and results are discussed in Section 3.5.2.

After analyzing the individual components and collectors, a circulating loop was built onsite to test the efficiency of the ADOPTS array. The loop began with a 12-volt DC pump to circulate the working fluid to an Omega flowmeter, through the solar array, down through the heat exchanger coil inside the solar hot water heater tank, and back to the pump. McMaster Carr pressure gauges were placed around the pump and around the collector. The pressure gauges helped determine whether the system was pressurized enough to avoid air bubbles inside the thermocouples and whether or not the pump was active. An expansion tank was also installed in order to remove any possible air bubbles inside the loop. Omega J-Type thermocouples were placed at the inlet and outlet of the array to determine the thermal efficiency. The plumbing to carry the fluid was CPVC, a long-lasting ideal material that is compatible with higher temperatures and working fluids. A thermal bath was added before the pump for some testing days, and water would be added to the solar hot water heater tank to provide a thermal load in order to control the working fluid temperatures and obtain specific data points. Insulation was wrapped around all plumping, thermocouples, and around the manifold to minimize convective losses to the environment.

The tank shown in the middle image of Figure 11 is a commercial 200 liters (53 gallon) solar hot water tank that has a copper coil heat exchanger inside the tank. These solar hot water tanks can be installed inside homes and are compatible with any solar thermal residential systems; a working fluid (recommended to be non-toxic heat transfer fluid with low freezing temperatures) is pumped up to the house roof, through the collector to be solar heated, down to the hot water tanks, and through the copper coil. The hot water tank, full of water from the city water line, is then heated by the working fluid through the coil heat exchanger, to create useable hot water for residential needs.

A Dataq web-based voltage, thermocouple, and pulse data logger was installed with eight analog channels and four digital channels. The data logger was set to start recording when solar irradiance reached 100 W/m^2 in the morning, and to stop recording once the solar irradiance fell below the start conditions in the evening. The logger recorded the solar irradiance, ambient temperature, flowmeter pulses, inlet temperature, and three outlet temperatures of the array every second. See Table 4 for more details on the equipment and supplies.

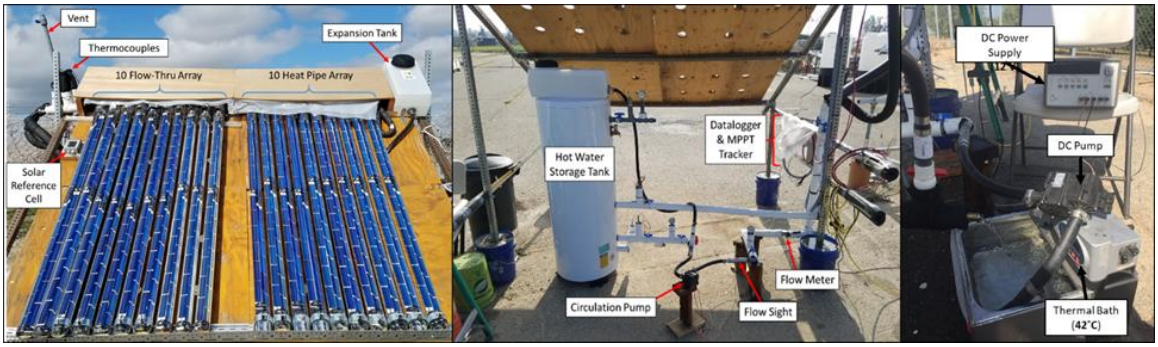

Figure 15:ADOPTS array (Left), test loop (Middle), & thermal bath (Right). Note that the uniform appearance of the tubes in the left array shows the effectiveness of the optics to enable the solar cell to appear the same as the optical illusion of it.

Equipment / Sensors	Manufacturer / Supplier	Model #	Description
Pump	TOPSFLO	TC-C14-A12-1820	12 V_{DC}, 6 A, 72 W Max Flow: 18 L/min
Pressure Gauge	McMaster Carr	4089K61	0-60 psi
Flow Meter	Omega	FTB4607	Max:20 GPM / Min:0.22 GPM Accuracy: ±1.5%
J-Type Thermocouples	Omega	TJ36-CASS-18U-6	Accuracy: ±1.1˚C or ±0.75%
Data logger	DATAQ	DI-808	Measures voltage, thermocouples, & pulses
Current Clamp	ETCR	ETCR-030D	Range: 0-10 A_{DC} Resolution: 0.01 A_{DC} Signal Output: 2.5 mV / 10 mA Accuracy: ±1%
Maximum Power Point Tracker (MPPT)	Victron	BlueSolar MPPT 100/15	Max: 100 V / 15 A Peak Efficiency: 98%
Solar Reference Cell	Ingenieurburo	Si-V-1.5TC-T	Calibrated Temp. Range: -38 to 78˚C Output Signal: 0-1.5 V for 0-1500 W/m^2
IV Curve Tracer	Keithley	2460 SourceMeter	Max: 100 V / 7 A_{DC} / 100 W
Solar Water Heater Tank	Duda Solar	N/A	Size: 53 gallons In-tank Coil: 1 mm thick TU1 Copper Coil

Table 4: Equipment and sensors

To hold the array, a low cost frame was built using wood, metal, and concrete buckets. Holes were cut into the wood boards, shown in the middle of Figure 15, to account for any possible wind load. The holes and the concrete buckets were incorporated to prevent the frame from being tipped over by high winds. The frame was also adjusted to a 37˚ angle from the horizon to match the latitude of the testing facility, and directed south towards the equator. This was to maximize the incoming solar irradiance throughout the full year. Note in Figure 15(left), the mentioned '10 Flow-Thru Array' uses a different type of thermal absorber of the collector. The table below lists the components used in the testing loop for the array. Based on the sensor uncertainties, shown in Table 4, the thermal efficiency is expected to have an uncertainty of ±3.6% (relative), while the electrical efficiency uncertainty is expected to be ±3%(relative).

2.4.3 Test Protocols

The following test conditions listed in Table 5 were required when collecting experimental results represented in this paper. Any data points that did not meet the following conditions were omitted.

Time	30 minutes
$\boldsymbol{T_{in}}$	Must not vary by more than $\pm$ **1** ℃ during course of test
ṁ	Must not vary by more than $\pm$ **8** $\boldsymbol{g/s}$ during course of test
G	≥800 *W/m*^2
	Must not vary by more than ±50 *W/m*^2 during course of test

Table 5: Test protocols

The following procedures tested optical efficiency, electrical efficiency, and stagnation.

1. For optical testing with no load, a city water line hose was fed to the testing loop as the heat transfer fluid. An open loop was used to maintain low water temperatures. The flowrate, solar irradiance, inlet, and outlet fluid temperatures were recorded to determine the thermal efficiency.
2. For performance testing with no load, a thermal bath was added to the open loop to obtain thermal efficiencies at varying temperatures. The city water line was used as the heat transfer fluid. To evaluate the thermal efficiencies at mid temperatures, some water had to be added to the 200-liter (53 gallon) solar water heater tank as a thermal load.
3. For electrical testing, the electrical efficiencies of each tube were measured using an IV curve at solar noon each day of testing. The electrical efficiency was recorded during thermal testing.
4. To test stagnation, thermocouples were placed on the condenser area of the heat pipe collector and condenser temperature, ambient temperature, and solar irradiance were recorded. The collector was left on sun at the same plane of the array until the condenser reached a maximum temperature.

2.5 *Results*

This section summarizes and discusses experimental results. Since the prototype uses commercial silicon solar cells that are cut into strips, a full testing analysis was conducted starting with the solar cells. After an understanding of the solar cell performance was determined, experiments were conducted with the PV/T collector both as a single collector and an array to fully quantify the performance.

2.5.1 Solar Cells

Before and after assembly, the solar cell efficiencies and thermal coefficient were characterized to fully understand the impacts of cutting the solar cells and performance at higher temperatures. The solar cell efficiency was calculated by first determining the maximum power point (MPP), the product of current (I) and voltage (V), and then dividing the MPP by the incoming solar power.

Equation 22

$$\eta_{cell,ap} = \frac{MPP}{A_{ap}G} \quad or \quad \eta_{cell} = \frac{MPP}{A_{cell}G}$$

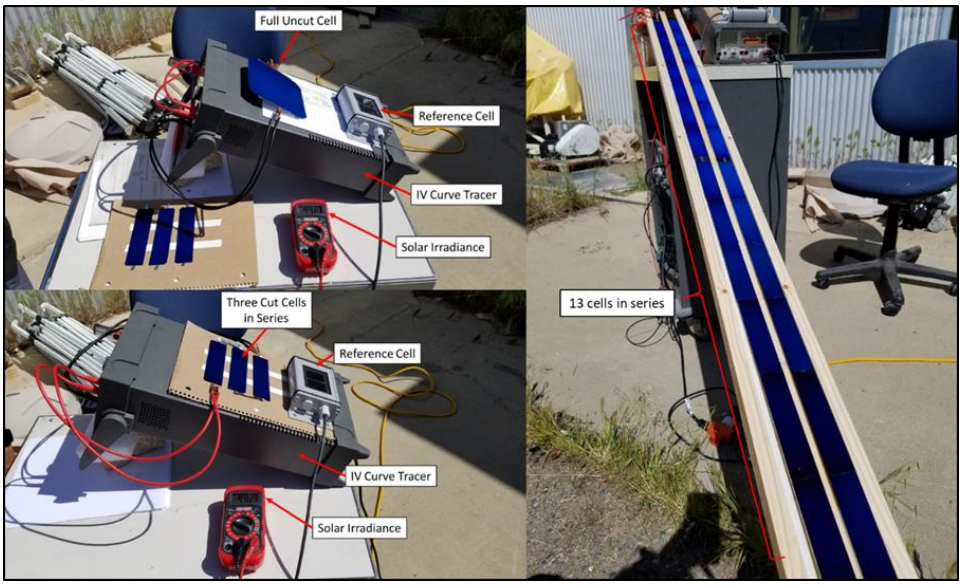

Figure 16: Cell characterization

Note that two efficiencies are analyzed, this is due to the fact that the area of the solar cell is different from the aperture area of the collector. Since the solar cells were sent to be cut, the efficiency was measured every step. The solar cells were tested on sun with an IV tracer, while simultaneously measuring the solar irradiance with a reference cell (Figure 16).

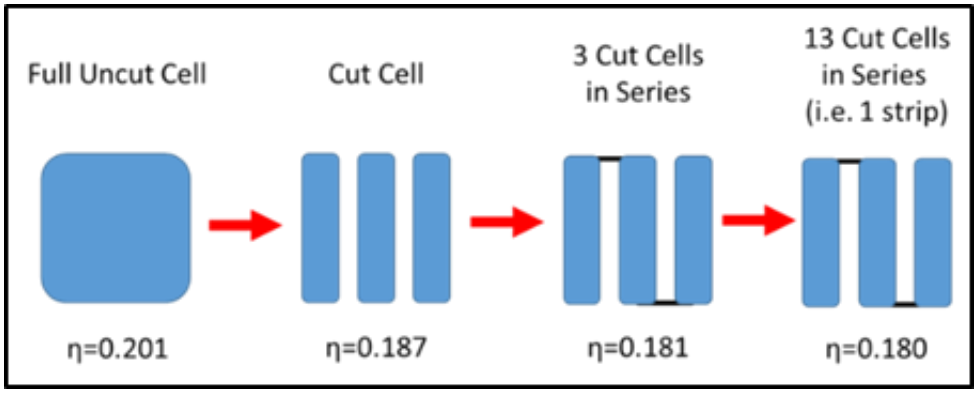

Figure 17: Cell efficiency at standard conditions after each process

The solar cell efficiency was first tested as a full cell, then after the cutting process, and again when soldered into strips. Overall, the efficiency dropped from about *20%* (full cell) to *18%* (13 cut cells in series). See Figure 17 for each step and corresponding efficiencies.

The drop in efficiency could be due to cutting the cells. As the cells were cut to fit the absorber dimensions, it is possible that there can be shorting between the n-type and p-type contacts, however it is uncertain.

A test was conducted to determine the temperature coefficient of the cut and fully assembled solar cell strips. The cells were constructed onto a minichannel where the heat transfer fluid flows directly into the absorber, through the active collector area, and back out. This was done in order to control the temperatures of the solar cells, assuming the temperature of the fluid and of the solar cells tracked together. Two heat sources were used, one being the sun, and the other a thermal bath

(set temperature of *85˚C*) connected to the inlet and outlet of the receiver with flex hoses. The heat transfer fluid used was water. The test set up is shown in Figure 18.

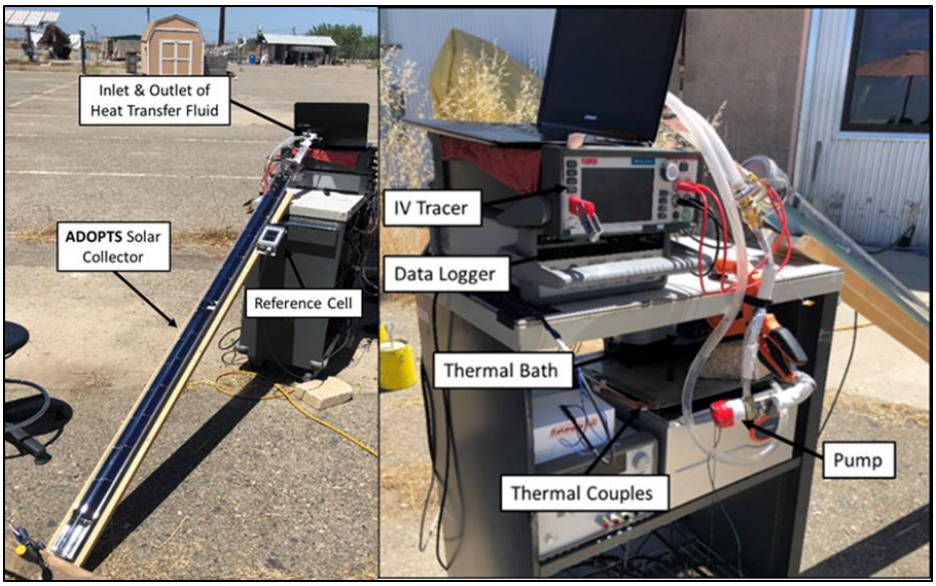

Figure 18: Solar cell thermal characterization experiments, with combined heat and power (CHP) solar collector on left and electronics on the right

Six thermocouples were placed inside the thermal bath, and an IV curve was recorded every water temperature increase of 5˚C. A final IV curve was recorded at 80˚C and the test was concluded. Results below show that the solar cells were working properly and fully connected up to the final mark of 80˚C.

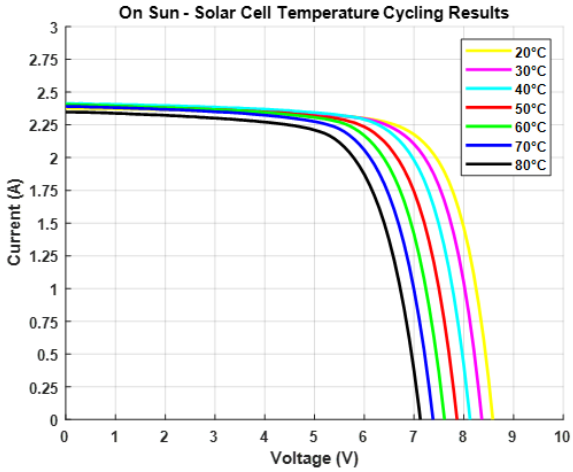

Figure 19: Solar cell IV curves at varying temperatures

Figure 19 demonstrates the IV curves of the hybrid collector at varying temperatures from *20˚C* up to *80˚C*. The efficiencies by cell area and aperture area were calculated to determine the temperature coefficient of the cells for the PV/T collector. As expected, the temperature has minimal effect on current, and an obvious decreasing effect on voltage. After the test, there was no signs of solar cell damage or disconnections from series or the absorber itself. There was an overall drop in efficiency

by cell area (*0.0975 m^2*) of *4% (relative)*, and drop in efficiency by aperture area (*0.1188 m^2*) of *3% (relative)*.

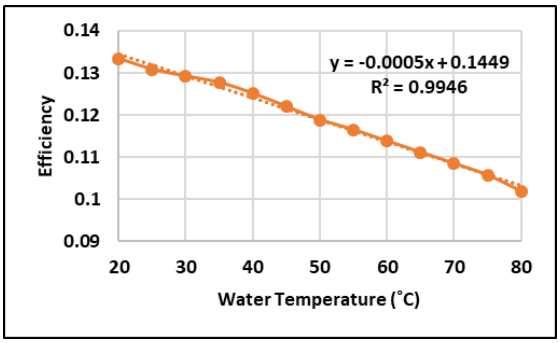

Figure 20: Electrical efficiency versus temperature of solar cells

The electrical efficiency by aperture area was calculated from the experimental data shown in Figure 19 and plotted versus the corresponding temperature in Figure 20 above. A best fit curve was determined and shown in Figure 16. Using the best fit line from Figure 20, the temperature coefficient is calculated to be:

Equation 23

$$\boldsymbol{Temperature\ Coefficient} = \frac{0.0005}{0.1449} \times 100\% = \mathbf{0.345}\ {}^{\%}/_{\circ C}$$

The manufacturer of the silicon solar cells advertised the efficiency temperature coefficient to be -0.35%/˚C. Electrical efficiency versus temperature results are consistent with the advertised values.

2.5.2 Single Tube

Before constructing the ten tube array, single collectors were tested to ascertain the condenser behavior and stagnation point of the thermal design component. First, water circulated into a thermos and two heat sinks, sandwiched on the top and bottom of the condenser area of the heat pipe absorber to use calorimetry to determine the thermal output of a single ADOPTS collector. A clamp was used to maximize contact between the condenser and heat sinks. A magnetic mixer, which supplies a rotating magnetic field to stir a metal bead placed inside the thermos is implemented to avoid temperature gradients within the HTF. The mixing metal bead, along with thermocouples, were placed inside the thermos to measure the water temperature as it was being heated by the collector over time. An actively cooled resistor (Figure 21**; Right**) was used as an electric load to determine the thermal and electrical performance with load.

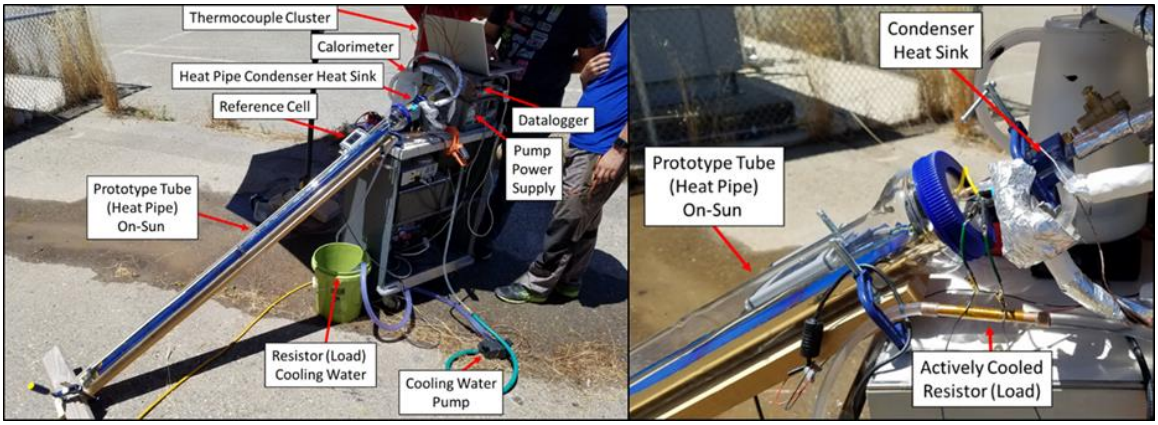

Figure 21: Single collector on-sun experiments

Test #	Global Irradiance (W/m^2)	Thermal Generation (W)	Thermal Efficiency (%)	Electrical Generation (W)	Electrical Efficiency (%)
7	1014	61.1	52%	12.0	10.3%
6	1023	68.0	58%	11.8	10.0%
5	1027	71.3	60%	11.4	10.0%
4	1028	66.5	56%	12.1	10.2%
3	1020	70.8	60%	12.6	10.7%
2	1016	80.1	68%	11.8	10.1%
1	1027	74.0	62%		
Average	**1022**	**70.3**	**60%**	**12.0**	**10.1%**

Table 6: Single collector performance thermal and electrical results

A thermocouple was placed on the heat pipe condenser, beneath the heat sinks to deduce the temperature difference between the condenser and fluid. After testing, the condenser was on average 5˚C warmer than the fluid. The electric and thermal performance of the single collector are recorded below in Table 5.

The electrical efficiency was calculated using an aperture area of *0.1155* m^2. The reasoning for the lower electrical efficiencies may be due to the load being a static resistor.

For extreme temperature performance, a single collector was placed on-sun (Figure 22). Two K-type thermocouples were placed on the condenser area of the heat pipe, and measured with a digital thermometer. Temperatures were measured until the temperature peaked. These tests were conducted during solar noon, where solar irradiance (recorded by the reference cell) is strongest.

Multiple tests were conducted. The maximum temperature reached was *93˚C*, shown above. The measured stagnation points are used to define the overall performance of the hybrid collector. The stagnation results are shown in the 'Array Experimental' results below (Figure 22). From these tests, a better understanding of the heat pipes' performance was gained, and noted that it is important to test the design's robustness to stagnating temperatures.

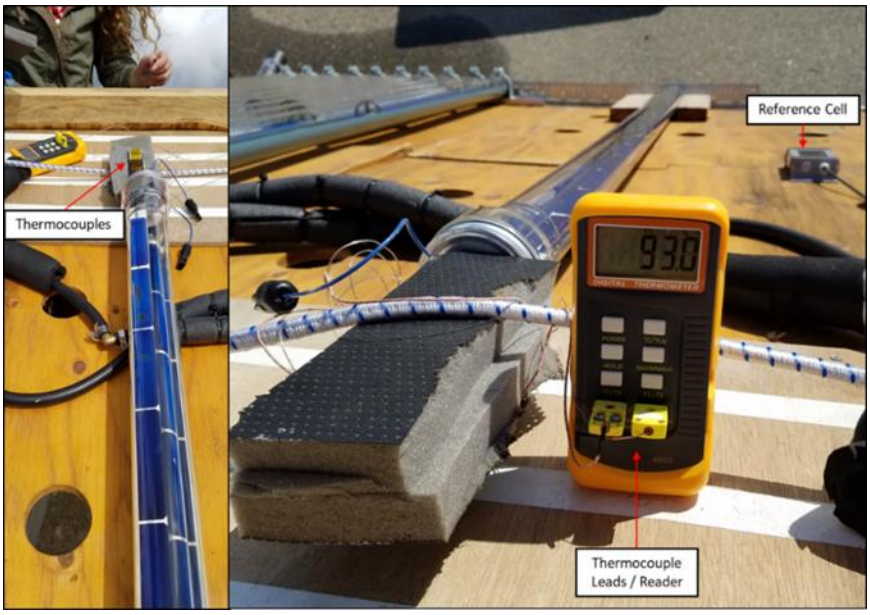

Figure 22: Stagnation experiment

2.5.3 *Array Experimental*

For the ten tubes' area, the average active length, meaning the length of heat pipe that sits inside the glass tube and exposed to sunlight, after assembly was *1.75 m*, making the actual average aperture area $A_{ap} = 1.155m^2$. When analyzing the data, the incoming solar power (Watts) is calculated by multiplying the aperture area of the collector (A_{ap}) by the incoming solar irradiance (GTI) on the same plane of the collector.

Equation 24

$$\boldsymbol{Q_{solar} = A_{ap}G}$$

The thermal output (Watts) is analyzed as the product of the measured flow rate, specific heat of the heat transfer fluid, and temperature difference between the inlet and outlet of the array. The specific heat of water used was *4.184 KJ/kgK*.

Equation 25

$$\boldsymbol{Q_{th} = \dot{m}c_p(T_{out} - T_{in})}$$

The thermal efficiency is then the thermal power output of the collector (Q_{th}) divided by the incoming solar power (Q_{solar}).

Equation 26

$$\boldsymbol{\eta_{thermal} = \frac{Q_{th}}{Q_{solar}}}$$

The ten heat pipe array was tested at varying fluid temperatures from low to high. Figure 23 demonstrates a day of optical testing at low fluid temperatures. The water remained at an average temperature of about *37˚C*, T* of *0.008 ˚C/ (W/m^2)*, and efficiency of *60%*. The left image shows the raw data, including flowrate, solar irradiance, fluid temperatures, and ambient temperatures. The collector efficiency throughout the day is shown in the right image. The 'Start' and 'End' dotted lines depict the data points that meet the testing conditions described in the 'Testing Protocols' section above.

Figure 24 demonstrates a full day of data with a high fluid temperature up to *64˚C*. This day would represent the standard operating conditions, with daily average T* of *0.0267 ˚C/ (W/m^2)* and thermal efficiency of *37% (relative)*. Again, IV curves of each collector were recorded at solar noon.

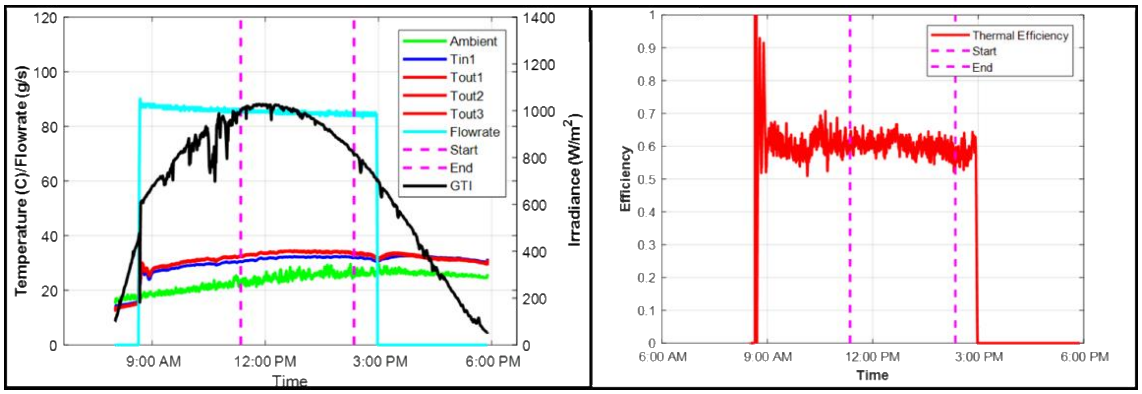

Figure 23: Array testing for low temperatures (left) & Efficiency curve for low temperature (right)

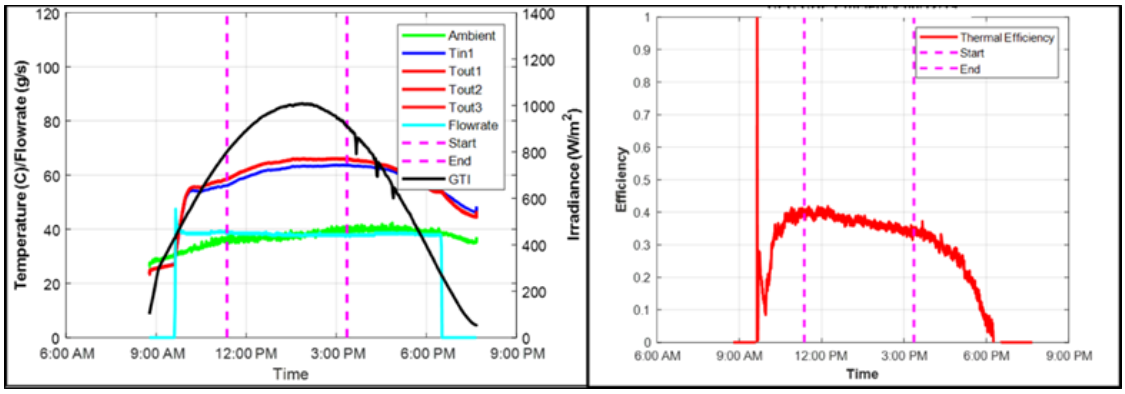

Figure 24:Array testing for high temperatures (left) & Efficiency curve for high temperature (right)

Fluid Temp. (˚C)	**TC 1 (˚C)**	**TC 2 (˚C)**	**TC 3 (˚C)**	**TC 4 (˚C)**
34	38.1	38.3	39.3	36
36	36.9	37.2	39.6	36.6
47	51.2	50.3	53.1	48.9
49	48.3	48.6	49.2	47.6
52	55.8	56.1	54.5	57.2
63	63.8	64	66.4	62.2
66	68.5	68.4	69.5	66.6

Table 7: Manifold temperatures

Four K-type surface thermocouples were placed in multiple locations to better characterize the manifold. The temperature differences between the manifold and fluid are demonstrated in Table 7. Note that the four thermocouples were placed in different locations. 'TC1' was placed between the heat pipe condenser at the start of the manifold, 'TC2' at the end, and 'TC3' in the middle. 'TC4' was placed on the outside of the manifold, between the manifold's top surface and the insulation.

On average, there is a ±4.5˚C difference between the heat pipe condensers and fluid temperature in Table 7. These results are consistent with the single tube testing discussed earlier. To determine the electrical performance, IV curves were taken of the individual ten collectors each test day around solar noon, where the sun is at its highest point in the sky.

In the figure above, the legend defines the heat pipe collector and then the solar irradiance in W/m^2. The IV curves in the left figure above were taken with a fluid temperature of *47.8˚C*, average solar irradiance of 957 W/m^2, and average efficiency by aperture of *10%*. As shown in Figure 25 **(left)**, heat pipe six (shown in yellow as 'hp 6') has a varying IV curve when compared to the rest. The curve drops current at a lower voltage, and continues to degrade as voltage is increased. This variation can be caused by a poor connection between individual solar cells within a strip. Unless the collector is taken down from the testing loop, and completely taken out of the glass tube to be debugged, the exact location of the poor connection cannot be determined.

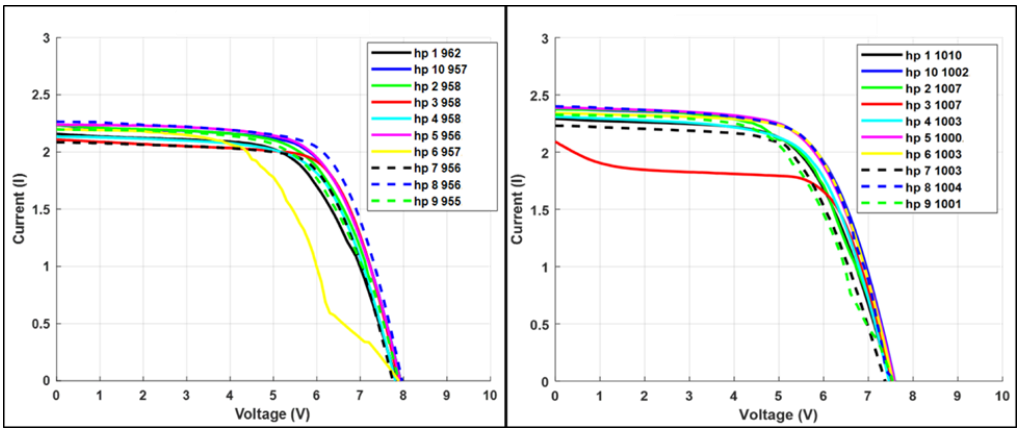

Figure 25: IV curves during solar noon

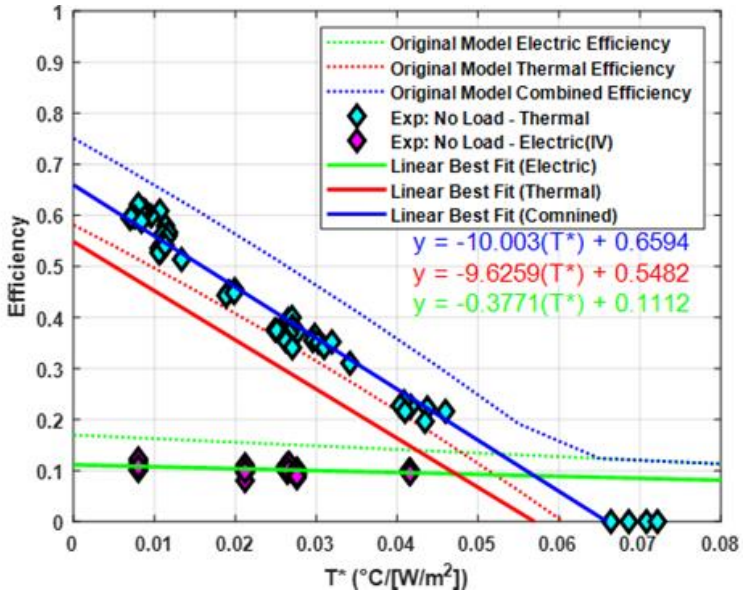

Figure 26: Array experimental and simulated results

The curves recorded on the right of Figure 25 were taken with a fluid temperature of 62.7˚C, average solar irradiance of 1004 W/m^2. In the right figure, heat pipe three (shown in red as 'hp 3') has an initial low current and continues to drop immediately between 0-1 volts. This drop in current at low voltages is a sign of partial shading. This partial shading can be caused the 3D printed supports that hold the absorber. The 10 tube array is placed on a frame, set at an of 37˚ from horizon, resulting in the shading effect. A curious observation from the electrical results is when comparing the left results to the right, heat pipe six's (yellow) contact issue corrected itself. With higher fluid temperatures, the contact resistance was no longer effective. The higher temperatures resulted in thermal expansion that provided a better connection than at lower temperatures.

Thirty minute increments of data that meet the testing protocols are recorded in Figure 26. The blue circles demonstrate the thermal efficiencies recorded with no electrical loads. The magenta circles demonstrate the electrical efficiencies by aperture area from the individual IV curves taken at solar noon each test day. When comparing to the model (shown as dotted lines), it was discovered that some assumptions from the model were not so accurate. A best fit curve (shown as solid lines) was

determined for the electric and combined, using the experimental thermal with no load and the electrical data points.

From the results shown in Figure 26, the combined efficiency of the thermal with an electrical load is the same as the thermal efficiency with no electrical load. Therefore, the thermal with load best fit curve was calculated by taking the difference of the thermal with no load and electric linear best fit curves. The heat pipe based collector demonstrated about *61%* thermal and 11% electrical optical efficiency ($T^* \cong 0.005$ *˚C/ (W/m²)*). Around operating temperatures ($T^* \cong 0.035$ *˚C/ (W/m²)*), the collector performed at about *31%* thermal and *10%* electrical efficiency.

As mentioned, some model assumptions were unmatched with the actual components used to assemble the collectors. The absorptance of the silicon solar cells and the silicone tape were assumed to be 1 and 0.6 in the model, however they seem to both be close to *0.95* absorptance. A *10˚C* temperature difference between the solar cell surface and heat transfer fluid was estimated in the thermal model, however there seems to be closer to a *15˚C* temperature difference based on the experimental results. The models aperture area (*1.188 m²*) was also slightly different from the assembled arrays area (*1.155 m²*). Some other variations from the model to the experimental results could be due to wind and additional convective losses to the environment due to moisture inside the glass tube during testing.

2.6 *Discussion*

Some variations in the components and manufacturing processes could maximize the solar collector's performance. Additional testing may also be beneficial to defining the efficiency.

2.6.1 Optical Losses

In order to increase the optical efficiency, a wider absorber should be used. The 30 mm absorber width introduced additional gap losses by creating a concentration ratio of C_X=60/66=0.909. However, increasing the absorber width, resulting in a $C_X \cong 1$, would minimize the optical losses, overall increasing the thermal and electrical efficiency.

Other optical losses that can be improved, lie within the glass tube. If a low costing anti-reflective coating was incorporated onto the glass tube, the transmissivity would increase to higher than *92%*. Also, the silver reflective coating on the bottom half of the glass tube's outer surface provided a sufficient low costing mirror to direct the sunlight onto the bottom half of the collector. However, having the reflective coating on the inside surface of the glass tube would remove the Fresnel reflection losses the light goes through as it passes through the glass to get to the reflective outer surface.

2.6.2 Solar Cells

Since commercial solar cells were bought from Sun Power and later cut to specific dimensions, the individual cells had to be hand-soldered in series with interconnections. During operation, the solar cells and absorbers go through a process of thermal expansion, which caused issues with the electrical connections between the individual solar cells. The thermal expansion could have had such a drastic effect on the connection due to the too small contact area to lead to disconnected cells. The small contact pad on the back of the solar cells made soldering extremely difficult, and minimized the area that was allowed for connecting the cells together with the interconnections. The temporary fix was purchasing an older generation manufactured cells with larger contact pads. However, in order to maximize the success rate of manufacturing, the best design option would be to purchase custom solar cells that match the dimensions of the absorber. Increasing the size of the solar cells to match the dimension of the absorber would also increase the efficiency by aperture area. Currently there is a packing factor, the cell area over the aperture area of the collector, of only

0.844. By increasing the packing factor to a realistic *0.95*, leaving room for interconnections and supports, the efficiency of the cells can be maximized for the design. Increasing the packing factor and overall reducing the interconnections between the individual solar cells also minimizes the risks of disconnection due to thermal expansion.

*2.6.3 **Manifold***

During testing, it was discovered that once the ten collectors were connected in series, the circuit would short circuit. This was due to the contact between individual heat pipes through the manifold, the current would carry from one heat pipe absorber to next through the aluminum minichannel manifold, creating a short circuiting effect between all ten tubes. With the electrical design using the absorber itself as the ground lead, there must be an electrically isolating media between the heat pipes and minichannel manifold. Another design would be to run a wire from the bottom of the absorber where the two strips are wired parallel, and run the line all the way up the tube through the cap, all together nulling the heat pipe absorber as an electrical concern. However, there are low cost electrically isolating medias, such as mica, that can isolate the absorbers from the manifold, however this would reduce the thermal conductivity drastically. Two mica sheets were layered between the manifold and the heat pipes, however resulted in a drastic drop in thermal efficiency. A better solution would be to anodize the minichannels in the manifold, specifically the outside surfaces of the minichannels that will come in contact with the heat pipes. Anodization is an electrochemical process used on aluminum that is corrosion resistant, and non-conductive. For future manufacturing, incorporating a proper anodization process should be considered.

Another improvement to the manifold would be the increasing contact between the manifold and condensers. During testing, a thermal paste with a make shift clamp (see Figure 14) was used; however, additional clamping mechanisms between each condenser would reduce air gaps, and increase conduction from the condensers to the minichannel manifold.

*2.6.4 **Cap***

A common issue with the collector was maintaining the seal on the cap. Moisture kept penetrating into the glass and there were not enough desiccants to absorb it all. This could be an explanation to the difference between the model and experimental results. With high measures of moisture inside the tube, there is convective losses inside the collector. An easy remedy would be to replace the type of epoxy with one that provides a more permanent and secure seal.

2.7 ***Cost Analysis***

A techno-economic model was developed to estimate bottom up module costs of the mass produced PV/T collector, annual thermal and electrical generation with natural gas savings, and carbon dioxide reductions.

2.7.1 *Cost and Comparison*

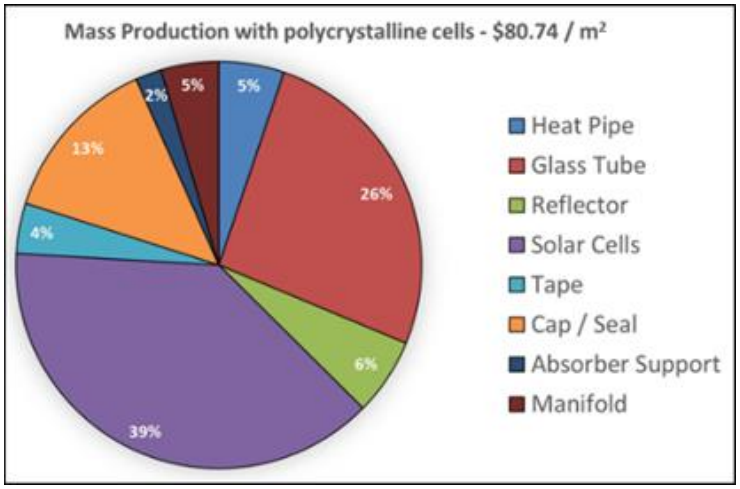

Figure 27: Mass production cost of ADOPTS collector

A bottom up cost was determine for a mass produced collector. The estimated cost is broken out by component in Figure 27.

The bottom up cost estimates the cost for the module only. Installation, maintenance, etc. were not included in the cost analysis. A comparison to the cost of currently available PV modules is made to quantify whether the cost of the proposed module is competitive in the current solar market. The current module cost $/W for PV modules is recorded as $0.20/W to $0.22/W by Feldman, et al [11]. The tested collector provides 150 W_{el}/m^2 and 400 W_{th}/m^2, making the cost of the cell collector to be:

Equation 27

$$\frac{\$80.47/m^2}{150\ W_{el}/m^2} \approx \$0.54/Wel$$

A comparison to PV modules is the best way to quantify the collector's cost since the cost and market of PV modules is so available to residential communities. When comparing to Feldman, et al. PV module costs, the cost calculated above can be broken down for the electrical-power rating to match the *$0.20/$W_{el}$*, or $30/$m^2$, leaving $50/$m^2$ or ~$0.12/$W_{th}$ for the thermal component of the PV/T collector. Therefore, the designed ADOPTS collector displays a promising future with competitive prices that can challenge current commercial PV modules, and provide an additional thermal output without the need for additional roof space.

2.7.2 *Saving and Reductions*

It is recorded from 2018 by the Solar Energy Local, a community-specific source of solar data across the United States, that the average annual global tilt irradiance (GTI) at the latitude tilt (*37°*) in Atwater, Ca is about *5.87 kWh/m^2/year*. The performance ratio (PR) is estimated to be ~ *75%*. The model used an average thermal efficiency (η_{th}) of *40%* and electrical efficiency (η_{el}) of *15%*. Average annual thermal and electric generation for the ADOPTS collector is calculated below.

Equation 28

$$Q_{annual\ output,th} = \frac{GTL*\eta_{th}*PR}{days/year} = 643\ kWh_{th}/m^2/year$$

Equation 29

$$Q_{annual\ output,el} = \frac{GTL*\eta_{el}*PR}{days/year} = 241\ kWh_{el}/m^2/year$$

The thermal generation is higher than the electrical generation by a factor of about *2.6*. Next, the annual amount of natural gas saved (or prevented from being used) is estimated by converting the annual generations into therms of natural gas, shown below.

Equation 30 $$NG_{saved,th} = \frac{Q_{annual\ output,th}}{29.3^{kWh}/_{therm}} = 21.9\ therms/m^2/year$$

Equation 31 $$NG_{saved,el} = \frac{Q_{annual\ output,el}*2.6}{29.3^{kWh}/_{therm}} = 21.4\ therms/m^2/year$$

Note that the natural gas saved through the electrical generation component is multiplied by a factor of 2.6; assuming a 38% efficiency for the power plant. From these calculations, the collector is estimated to save a total of *43 therms/m^2/year* (or *1300 kWh/m^2/year*).

It is reported by the U.S. Energy Information Administration that the average residential price in April of 2019 is about *\$0.13/kWh$_{el}$* for electricity, and *\$1.05/therm* (*\$0.04/kWh$_{th}$*) for thermal in the United States. From the previously calculated annual thermal and electrical generation of the PV/T collector, the amount of thermal (S_{th}) and electrical savings (S_{el}) in \$/m^2/year is shown below.

Equation 32 $$S_{th} = 643\ kWh_{th}/m^2/year * \frac{1\ therm}{29.3\ kWh} * \frac{\$1.05}{therm} = \$23/m^2/year$$

Equation 33 $$S_{el} = 241\ kWh_{th}/m^2/year * \frac{\$0.13}{kWh_{el}} \approx \$31/m^2/year$$

The California Air Resource Board reported emissions factors of *5.3 kg CO$_2$/therms* of natural gas (NG), and *0.331 kg CO$_2$/kWh* electric. The annual CO_2 emissions prevented by the thermal (R_{th}) and electric (R_{el}) components of the collector are calculated below.

Equation 34 $$R_{th} = 21.9\ {}^{therms}/_{m^2/_{year}} * 5.3\ {}^{kg\ CO_2}/_{therm_{NG}} \approx 116\ kg\ CO_2/m^2/year$$

Equation 35 $$R_{el} = 241\ {}^{kWh_{el}}/_{m^2/_{year}} * 0.331\ {}^{kg\ CO_2}/_{kWh_{el}} \approx 79.8\ kg\ CO_2/m^2/year$$

The thermal component to the collector will provide the largest reduction of emissions. Assuming a collector lifespan of 20 years, a total of about *3916 kg of CO$_2$/m^2* (*4.3 tons CO$_2$/m^2*) can be avoided by the ADOPTS collector.

2.8 ***Conclusion***

The Advanced Optical Photovoltaic Thermal System (ADOPTS) solar collector was thoroughly tested and analyzed in performance and cost analysis these past two years. The collector provides a low cost, two-in-one solution for residential/commercial hot water and electricity. The ADOPTS collector can be used for both single or multi-family residential buildings, or industrial-commercial project. The optics allow the device to function similar to a flat plate, which takes all diffuse and direct light. However, the limitation of the heat pipe requires a minimum of 5˚ of inclination in order to maintain the heat pipe function. Therefore, mounting on a flat roof top will require a low shelf to account for the minimum angle. A single square meter of the ADOPTS collector will provide *150 W$_{el}$* and *400 W$_{th}$*, can heat 100 liters of water up to *60˚C* in a day, costs *\$81/m^2*, saves a total of *43 therms/m^2/year* (or *1300 kWh/m^2/year*) of natural gas for both heat and electricity (assuming the electricity is generated from a natural gas plant), saves in total of *\$54/m^2/year* cost of electricity and heat, and prevents a total of *3916 kg of CO$_2$/m^2* (or *4.3 tons CO$_2$/m^2*) over a 20-year period. The collector can cover the module cost through energy saving within 1 ½ years. The

collector provides a cost and performance competitive option that delivers both heat and electricity to residents, while simultaneously preventing GHG emissions.

Furthering the development of custom solar cells to match the dimensions of the absorber will eliminate the contact issues, and adapting a low cost anti-reflective coating to the glass tubes can improve the collector's efficiency and success rates. In order to deliver a commercial ready technology, additional research and improvements in manufacturing, discussed previously, should be conducted to improve the collector.

2.9 *Acknowledgments*

This document was prepared as a result of work sponsored by the California Energy Commission. It does not necessarily represent the views of the Energy Commission, its employees, or the State of California. The Energy Commission, the State of California, its employees, contractors, and subcontractors make no warranty, express or implied, and assume no legal liability for the information in this document; nor does any party represent that the use of this information will not infringe upon privately owned rights. This report has not been approved or disapproved by the Energy Commission nor has the Energy Commission passed upon the accuracy of the information in this report.

This work was supported by the California Energy Commission as part of GFO-16-503 under contract # PIR-16-007.

Also, a special thanks for the time and assistance from Jonathan Ferry, Dr. Sarah Kurtz, Keith Blackburn, Danny Wu, Aaron Wheeler, Sreedevi Reddy, Athalia Soles, RETC Testing Facility, and the American Precision Dicing facility.

Chapter 3. The integrated compound parabolic concentration (ICPC): A low cost, non-tracking, high-efficiency solar thermal collector for process heating up to 150˚C

Note: This chapter has been submitted and 'under review' to Applied Energy Journal (Update: submitted Jan 2022, 1 Review Completed in March 2022, Review invitations sent 2+).

Authors: Jordyn Brinkley[1st Author], Bennett Widyolar[Corresp.], Yogesh Bhusal, Lun Jiang, Roland Winston

Abstract: As greenhouse gasses (GHG) continue to rise, the reliance on fossil fuels in the energy sector must be mitigated to limit the impacts of climate change. Solar energy is an abundant resource, available almost everywhere on planet earth, however capturing and harnessing this in a way that is economical in order to compete with carbon emitting fossil fuels can be challenging. This manuscript discusses the design and experimentation of the integrated compound parabolic concentrator (ICPC), which consists of an evacuated glass tube, minichannel absorber, reflective coating, and metal-glass seal, to provide renewable heat for energy sectors such as industrial processes and thermal desalination. The components of the ICPC are made from low cost materials of glass and aluminum, and has a module cost estimate of $65.54/m2. The ICPC module experimentally demonstrated thermal heat up to 140˚C at efficiencies >55%, with experimental instantaneous solar-to-thermal efficiencies of 72% ±4% at 43˚C, 65% ±6% at 95˚C, 60% ±4% at 120˚C, and 55% ±5% at 140˚C. The ICPC is capable of reaching a maximum temperature of 295˚C. The preliminary cost estimate LCOH of $0.015/kWh is highly attractive when competing with the low prices of alternative fossil fuels.

3.1 *Introduction*

Technological advances of the 20th century have enabled unprecedented growth in human population with a projected global population of over 10 billion by the end of the 21st century[38]. This population growth creates an increasing demand for water, food, and energy, with global energy demand expected to increase 4.6% by the end of 2021[39]. To meet this increasing demand for energy, countries have traditionally relied upon fossil fuels, which have become the largest source of greenhouse gas (GHG) emissions. As GHGs continuously increase, global climate repercussions are appearing with global temperatures increasing 0.3˚ per decade since 1970[40], known as climate change. With trending global temperature rise, the world is seeing less sea ice, snow cover, and glaciers and increased ocean, Troposphere, and air temperatures along with rising sea levels. The increasing sea levels and ocean temperatures are already presenting moderate risks to climates associated to coastal erosion, ecosystem degradation (including damage to Arctic systems, coral reefs, & increased species extinction risks), flood, droughts, and more frequent extreme weather events [41]–[43]. Established carbon budgets to minimize emissions and global policies limiting warming to 1.5˚C by 2100, help reduce the risks of climate change, such as the Paris Agreement with the goal to further the growing momentum towards decarbonization of the global economy[44].

The global energy sector is still heavily consuming fossil fuels to meet demands and current projection models indicating natural gas is the only fossil fuel anticipated to have strong growth in the future [45]: natural gas demand is set to grow 3.2% in 2021[39]. The energy demand cannot wait for oil and coal technologies to advance fast enough to reduce GHG emissions in production (to limit global temperature rise), therefore alternative renewable energy forms are needed in order to avoid disruptions in energy supplies. The United States (U.S.) holds the world's largest natural gas market and has regularly been emitting energy-related carbon emissions for over a century.

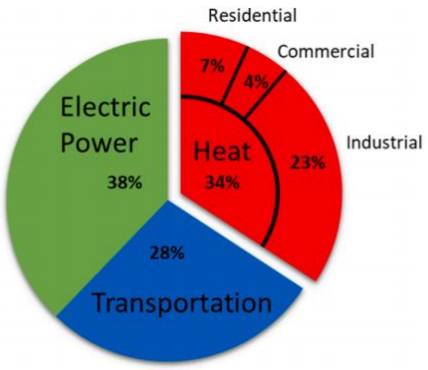

Figure 28:U.S. Primary Energy Consumption[11]

The U.S. total primary energy consumption in 2020 reached 93.13 Quadrillion BTU's [46], with 78% consumption from fossil fuels, 12% from renewables, and the rest from nuclear and other energy forms. U.S. energy sector is broken-down by end-use in Figure 28, with electricity accounting for 38%, 28% transportation, and 34% of all energy consumed by heat. With many emerging green technologies, such as solar photovoltaics (PV), wind, hydro, nuclear, and more, the electricity sector has many options for cost-competitive replacements for fossil fuels to meet the demands (considering technological advances and lowering costs of electrical storage is currently underway with research and government funding/subsidies). McKinsey and Company [47] argue that electric vehicles will most likely become the best economic choice for the transportation sectors in many parts of the world with electricity generating renewables coupled with storage to reduce costs and GHG emissions. Finally, when analyzing the heat sector of the US energy consumption, the residential and commercial heat sectors account for 11% of the heat energy demand with water heating, cooking, and space heating. In order to convert the heat energy demand for the industrial sector in the US that makes up 23%, a look into temperature requirements of manufacturing industry processes is categorized in the figure below.

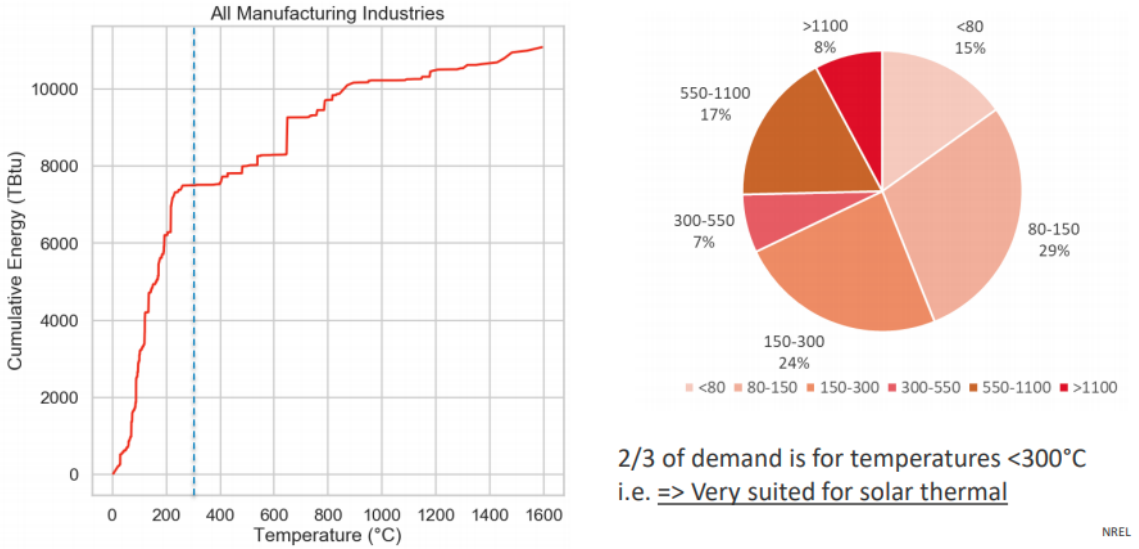

Figure 29:US manufacturing cumulative energy in TBtu with corresponding processes' temperatures (LEFT) & US industrial processes temperature requirements pie chart (RIGHT) [13], [48]

The majority of industrial processes' heat is consumed at temperatures below 300˚C, with 44% of demand below 150˚C (Figure 29). These temperatures are readily achievable using the world's most abundant source of energy, the sun. Solar thermal technologies convert solar radiation into heat; they are often classified as concentrated or non-concentrated and are often categorized into three operating temperature ranges: [a] low temperature (30-150˚C), [b] medium temperature (150-400˚C), and [c] high temperature systems (>400˚C) [17].

Low temperature collectors are often non-concentrated, and include flat plate collectors (FPC), evacuated tube collectors (ETC), solar ponds, and solar cookers. Medium temperature STE systems like the linear Fresnel reflectors (LFR), parabolic troughs (PTC), and external compound parabolic concentrators (XCPC) are concentrated: these collectors deliver the sunlight (using lenses or mirrors) onto an absorber surface to increase the power density of the solar radiation. Note evacuated flat plates are medium temperature collectors and non-concentrated. The most important property of a concentrator is the *concentration ratio*, defined as the ratio of area of input solar radiation, or 'aperture area', divided by area of output radiation, or 'absorber area'. STE collectors like central receivers (CR), parabolic dishes (PDC), and solar towers are designed with even higher concentration and result in higher operating temperatures (>400˚C). Most concentrated collectors require mechanical systems to move the collectors throughout the day in order to track the sun, which increases material and operation costs; tracking is required due to the fact that these types of collectors only accept direct light, and do not absorb diffuse light. A summary of common commercialized STE collectors is compiled in Table 8 below.

Solar Thermal Collector Type	Concentration Ratio	Temperature Range (˚C)	Collector Cost ($/m2)	Thermal Efficiency at 120˚C	LCOH ($/kWh$_{th}$)
XCPC	1.4	25-240	160 [49]	60% [49]	$0.023-0.029/kWh [49], [50]
Parabolic Trough	24-32	50-600	150 [51]	60% [52]	$0.0278-0.035/kWh[53][54]
Evacuated Flat Plate (EFP)	1	25-205	350 [55]	65% [56]	$0.05-0.09/kWh[57]
Linear Fresnel (LF)	20	25-290	180 [58]	58% [59]	$0.027-0.047/kWh[54]
CPC (shallow)	0.7	25-105	**	**	$0.015-0.017/kWh[54]
Flat Plate (FPC)	1	25-95	250[60]	-	**
Evacuated Tube (all-glass)	1/π	25-95	**	-	**
Vacuum Tube (metal-glass)	1	25-185	**	**	**
Parabolic Dish (PDC)	600-2000[61]	100-1500	350[62]	-	$0.115-0.235/kWh [62]

*Table 8: Commercial Solar Thermal Technology Summary. Note thermal efficiency column references modular efficiency & any data marked as '**' indicated information that is either only found through distributors that include unknown commercial profit percentages and/or information not readily available in peer-reviewed journals. A food processing commercial company quoted paying local natural gas public utility as low as $0.015/kWh$_{th}$ for heat within the San Joaquin Valley in Central California (an area/state with extremely low prices for natural gas in the US); host site for the experiments discussed in this manuscript is located in Central California.*

With the goal to displace fossil fuels in the heat sector, the residential and commercial heat demands (that make up 11% of U.S.'s total energy demand, see Figure 28) can be possibly displaced with low temperature renewable collectors (i.e. flat plates, evacuated tubes, etc.) and/or electric heating units (electric water heaters, stoves, ovens). When addressing the 44% of the industrial heat demand that requires temperatures up to 150˚C (industry heat makes up 23% of all U.S. energy demand), a cost-competitive solar thermal collector is needed. The high temperature collectors are expensive, complicated to operate, and require a lot of space, therefore these collectors are impractical and over-engineered for this heat demand range; low temperature collectors that cannot produce the operating temperature requirements are futile.

Certain collectors can meet the temperature requirements and provide a practical solution, however costs may not be competitive enough. For example, commercial systems like the XCPC and EFP can provide temperatures up to 150˚C, with solar-to-thermal efficiencies as high as 60% and 65% at 120˚C (shown in Table 8), however, when comparing against natural gas that can be as low as $\$0.015/kWh_{th}$ (price quoted by California food processing company), the levelized cost of heat (LCOH) of the XCPC and EFP cannot compete. A simple, high efficiency collector that can be developed to match the lowest costs of natural gas is the most ideal option in order to compete with today's inexpensive fossil fuels and meet the aggressive goals of 100% renewable energy consumption.

This manuscript discusses the development and experimental performance of a low cost solar thermal collector called the integrated compound parabolic concentrator (ICPC), which combines nonimaging optics and aluminum minichannel technology for high efficiency solar thermal process heat applications up to 150˚C. Finally, a cost analysis is performed to estimate the potential LCOH provided by the ICPC technology.

3.2 *Design*

3.2.1 Integrated Compound Parabolic Concentrator (ICPC)

The ICPC was first described by J.D. Garrison in 1979 [63] and Snail et al. in 1984 [64], and has since undergone several years of development. It is a highly efficient, simple, stationary (non-tracking) vacuum tube collector with integrated optics. By combining nonimaging concentration with selective coated absorbers encased in glass vacuum envelope, Garrison offered a path to providing a solar collector that can be completely stationary and produce high temperatures. Previous iterations included a 100 m^2 fabricated array in 1998 that supplied 50% solar-to-thermal efficiency heat (at 140-160˚C) to a double-effect absorption chiller. This array has been discussed thoroughly in proceedings and papers, concluding with a 20-year analysis [65]–[67]. Most recently, an ICPC iteration with a shaped cusp glass tube as the encasing and the reflector was fabricated and tested at UC Merced [68], [69]; the ICPC resulted in 42% efficiencies at 200˚C. Previous iterations were expensive due to production and manufacturing constraints of the time and never commercialized, however developments to metal-glass seal technology and aluminum minichannels today enable ultra-low material costs for ICPC collectors. Previously, this design of the ICPC coupled with low cost materials of aluminum and glass along with both minichannel and heat pipe absorbers was developed as a non-vacuum photovoltaic/thermal (PV/T) solar hybrid collector and thoroughly analyzed and published [19], [70], [71]. This manuscript explores the promising applications by combining vacuum insulation and the low cost ICPC design.

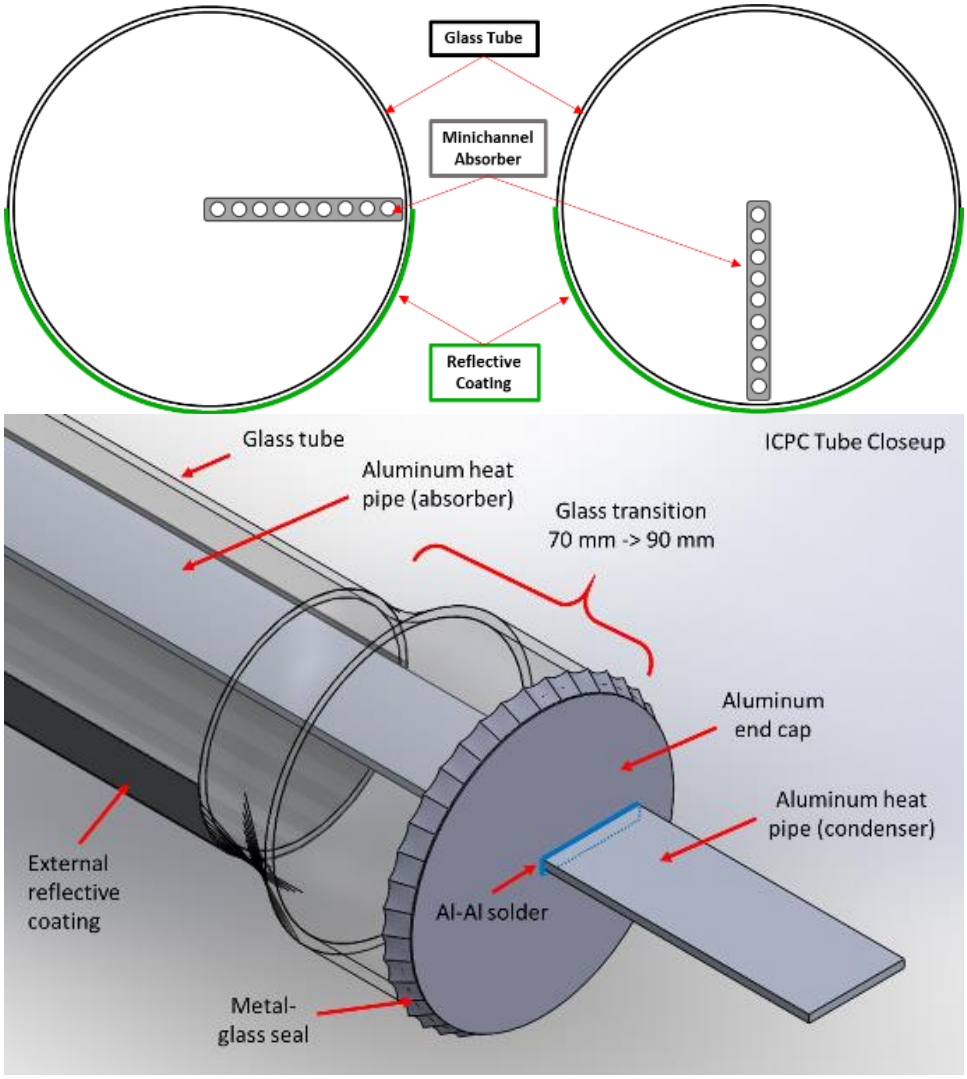

Figure 30: TOP-ICPC cross-section with minichannel absorbers orientations (horizontal & vertical) & BOTTOM - Schematic of individual components that make up the ICPC collector

The ICPC collector consists of an (i) evacuated glass tube, (ii) minichannel absorber, (iii) reflective coating, and (iv) thermocompression metal-glass seal (Figure 30). The cylindrical borosilicate glass tube (2m length, 70mm OD, 66 mm ID) encases the absorber (32 mm width, 3 mm thickness) in a vacuum-insulation jacket, improving thermal efficiency at elevated temperatures by eliminating convective and conductive heat loss. Using nonimaging optic methods, a simple optic is developed in the shape of a half circle derived from the shape of the absorber itself. A highly reflective coating applied to the bottom half of the glass tube provides optical access to the bottom half of the absorber. In this way, the ICPC has a geometric concentration ratio of approximately 1 and all incoming solar irradiance (both direct and diffuse) within the half aperture will be reflected to the bottom surface (note, flat plate concentration ratio is typically ½, while all-glass vacuum tube is $1/\pi$); concentration ratio is the aperture area divided by the absorber area [49]. The absorber area being the top and bottom area of the minichannel (32mm*2=64mm). The aperture area being the area accepting light rays, which would be the diameter of the glass encasing acting as the optic. Through this simple wide-angle nonimaging optical concentrator, the need for tracking is

eliminated, allowing a stationary configuration (which is a cost reduction when comparing to tracking solar thermal technologies).

The absorber is made from a 2 m long aluminum minichannel, which is selectively coated to provide high absorptance and low emittance at target operating temperatures and absorb as much of the solar spectrum as possible while reducing radiative losses. To collect the heat absorbed, a heat transfer fluid (HTF) is pumped directly into the minichannels and transport the heat. Aluminum minichannels are widely adopted by the automotive industry for use in radiators and also in the electronics industry for cooling methods. These are a great candidate for solar collector absorbers due to increased surface area for convective heat transfer and minimized conductive losses through the absorber material, and can be made with low cost materials [72].

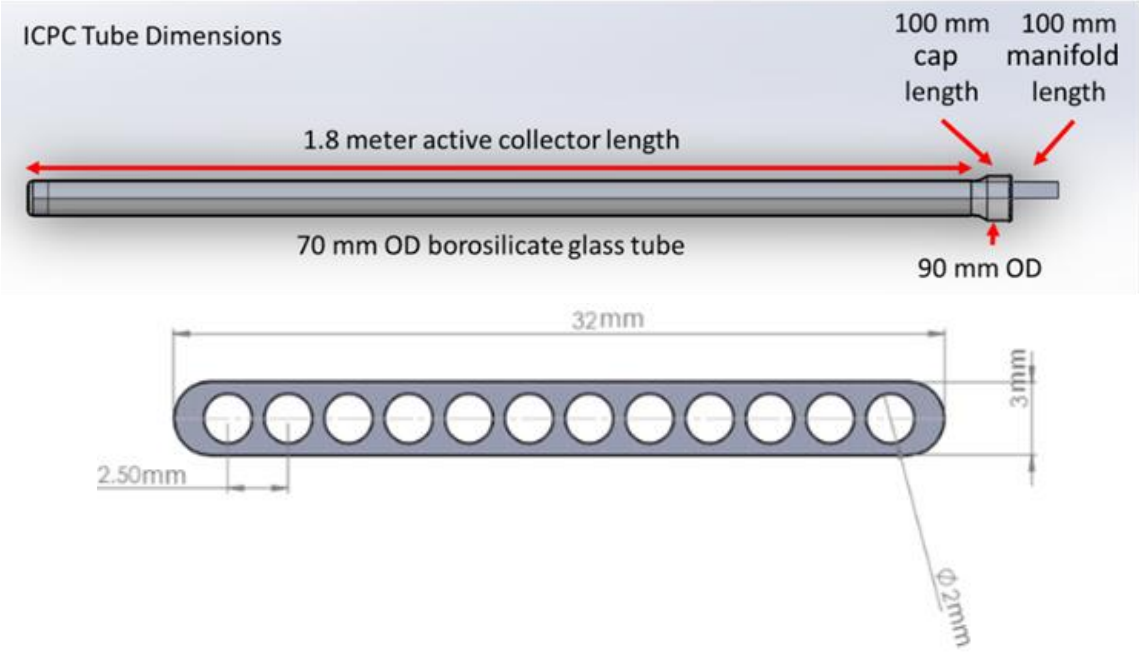

Figure 31: ICPC dimensions of components, including glass tube and minichannel absorber dimensions

The absorber has 1.8 m of active collector length, meaning length that will be exposed and absorb solar irradiance, within the vacuum insulated glass tube. The glass tube with the reflective coating to direct sunlight to the bottom side of the absorber makes the total aperture length 1.8m with a 0.066m width, resulting in a total aperture area of 0.1188 m^2. The remaining 0.2 m of the full 2 m length of the absorber is allocated to the transition section of the metal glass seal and provide extra length outside of vacuum glass tube to account for manifold connections (Figure 31). Once individual ICPC tubes are manufactured, they can be assembled into modules.

*3.2.2 **Modeling***

Performance of the ICPC was estimated using a ray tracking software and an analytical thermal model. Optical efficiency is the efficiency of the collector taking into account *only* the optical material properties and geometric positioning of the components that make up the collector. The optical configuration for the ICPC was modeled with the following material optical properties of each component: borosilicate glass, aluminum minichannel with a selective coating, silver-based reflective coating (Figure 32; left for defined optical properties)..

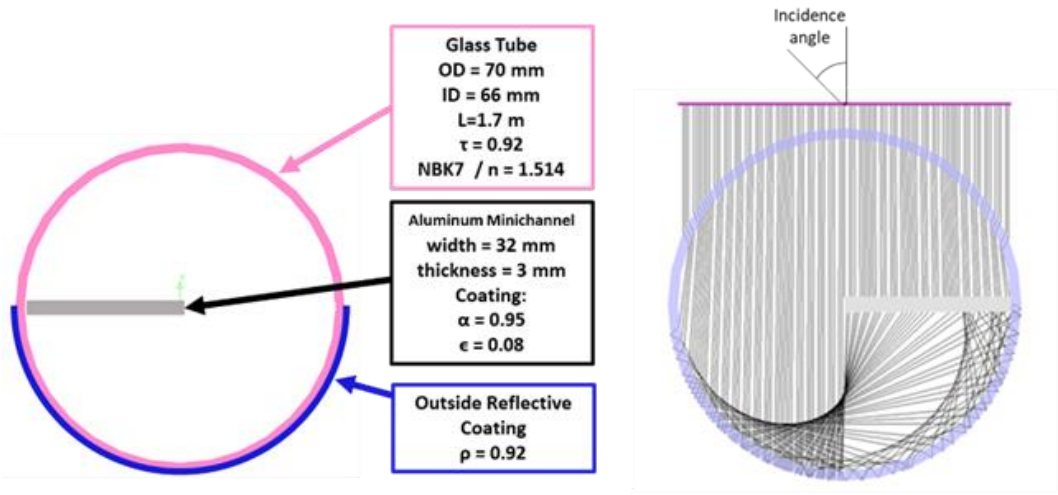

Figure 32: LEFT-ICPC ray tracing schematic with defined dimensions and optical material properties & RIGHT-Clear ray tracing rendering of ICPC at normal incidence

At normal incidence (meaning 0˚ light angle, directly perpendicular to the aperture area), all optical material properties and any 'gaps' are impacting the efficiency. A visual of the ICPC configuration at normal incidence is shown in Figure 32; right.

Varying angles are shown in the figure below ranging from -90˚ to 90˚. This analysis replicates the sun's movement through a day, as the collector is stationed in a north-south configuration with the incoming solar 'sweeping' across the ICPC, depicted in Figure 33. The light, coming from the sun, passes through the borosilicate glass tube slightly refracted: there are also Fresnel losses at each surface the light passes through [73]. After transmitting through the glass, some light will be directly absorbed by the top surface of the minichannels, and the other half will hit the mirror.

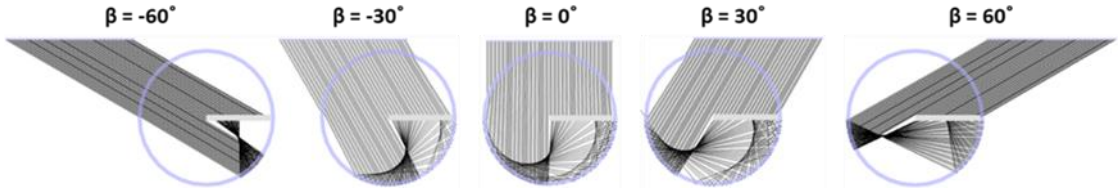

Figure 33: Ray tracing rendering of ICPC at varying incoming angles (-60˚,-30 ˚,0 ˚,30 ˚,60 ˚)

As seen in Figure 33, any solar that reaches the open aperture is directed towards the bottom surface of the absorber due to the silver mirroring process that is on the outside, bottom-half, surface of the glass tube. There is some gap loss that occurs in the 1 mm distance from the inside of the 32 mm absorber width and the 66 ID of the borosilicate glass tube. There are also small gap losses that occur through the thickness of the glass tube at the axis of aperture. These losses however are miniscule as long as the absorber maintains its horizontal position against the glass (not moving towards the center of the tube). The simulation configuration had receivers on each surface of the rectangular absorber. Figure 34 (left) shows the percentage of the total light from source absorbed by each surface face. The 'inside' and 'outside' surface, or the left and right surfaces of the rectangular absorber, correspond to the 3 mm thickness of the absorber (length of 1.8 m and width of 3mm). To calculate the optical efficiencies at a certain angle, each surface's absorbed efficiencies are summed to a total to represent the minichannel absorber as a whole. From the data shown below, the optical efficiency at normal incidence to be *75.6%*.

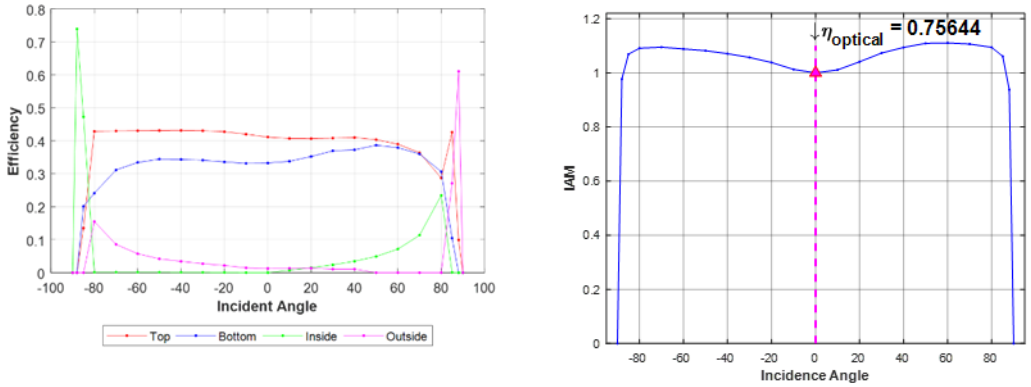

*Figure 34: LEFT-Ray tracing results of absorption of each surface of the minichannel absorber of the ICPC * Right-Incident angle modifier (IAM) results of the ICPC*

As expected, the 'top' surface absorbed the most solar light throughout the sweep of varying incidence angles (Figure 34; left), while the 'bottom' surface absorbed slightly less due to the additional reflective losses from the mirror that the 'top' surface does not experience. At the extreme angles 80+˚, the 'inside' and 'outside' surface do have high efficiencies in a small angle range, however this has minor effect on the thermal output. These extreme angles resemble the morning and evening of the sun's position when solar irradiance is low. The angles that will provide sufficient solar radiation to transport the heat into the HTF will be in the middle angles (-80˚ to 80˚) when the solar irradiation will be higher during the day.

The incident angle modifier (IAM) is a standard testing parameter used for wide-angle or non-tracking solar collectors and used to determine how long the collector can be utilized, with every 15˚ accounting for one hour of sun during the day. The y-axis represents the "relative efficiency" to the optical efficiency at normal incidence; relative efficiency is the total efficiency (absorbed) at the corresponding incident angle (x-axis) divided by the optical efficiency at normal incidence (constant 75.6%). For example, the relative efficiency at angle 0˚ is 1 (Figure 34), therefore IAM demonstrates that the efficiency is higher at off-angles (≠0˚). At normal incidence or beta= 0˚, the collector has the most optical losses. This normal incidence corresponds to solar noon, where the sun is at its highest position and solar irradiance. However, there is only slightly more losses when compared to the remaining solar positions throughout the day. The ICPC allows a simple optic to provide a wide-angle non-tracking design to absorb solar radiation throughout a full day.

After the optical performance was defined, a preliminary numerical thermal model for a single ICPC tube was developed in order to obtain the solar-to-thermal efficiency ($\eta_{thermal}$) when the minichannel absorber reaches the target operating temperatures of 150°C. The modeled thermal efficiency is shown in Equation 36.

Equation 36

$$\eta_{thermal} = \eta_{optical} - radiative\ losses = \eta_{optical} - \frac{\epsilon\sigma\left(T_{abs}^4 - T_{amb}^4\right)}{\frac{A_{aperture}}{A_{absorber}} * G}$$

Where $\eta_{optical}$ is the optical efficiency determined from the ray tracing simulation results, emissivity of the selective coating on the absorber is $\epsilon = 0.08$, ambient temperature of the surrounding environment is $T_{amb} = 25^{\circ}C$, and global solar irradiance $G = 1000\ W/m^2$. The aperture area ($A_{aperture}$) of a single ICPC tube is 0.1188 m^2, the active absorber area ($A_{absorber}$) is 0.1152 m^2, making the concentration ratio ≈ 1. The ICPC is under vacuum to reduce convective losses inside the collector itself to the environment, along with minichannels optimizing and minimizing conductive losses, therefore optical and radiative losses will be the major factors to reduce the solar-to-thermal efficiency.

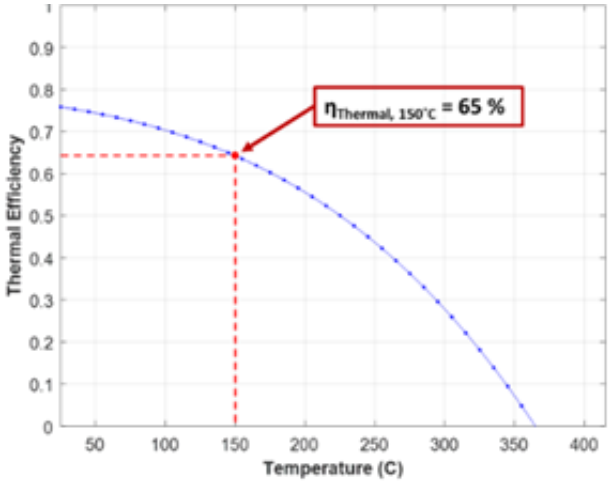

Figure 35: ICPC tube analytical thermal model results

The preliminary single tube thermal efficiency curve (shown in Figure 35 & Figure 41) was then constructed at multiple temperatures. The thermal model demonstrated optical efficiencies of around 73-75% at temperatures 40-50˚C (similar to the modeled optical efficiency of 75.6% from the ray tracing results). From the analytical thermal model, the ICPC collector is expected to perform at thermal efficiencies up to 65% at temperatures as high as 150˚C and a stagnation temperature of 375˚C.

3.3 *Experimental Testing*

3.3.1 Prototype Development

In summary, individual ICPC tubes were assembled using glass tubes, selectively coated minichannel absorbers, gas-getters, and stainless steel absorber supports. Absorber supports were designed to allow the absorber to slide and expand length-wise direction to avoid any buckling of the absorber as it goes through daily thermal cycling. The final stage is the vacuum bake-out process. Once the individual tubes were manufactured, a commercial silver coating was applied to the bottom exterior of the glass tubes.

The individual ICPC tubes are assembled into modules through the use of a custom manifold. Note in Figure 36, the absorber is now in a vertical positon (compared to horizontal) for ease of manifold assembly. To connect each ICPC to the manifold, the tubes were connected in parallel.

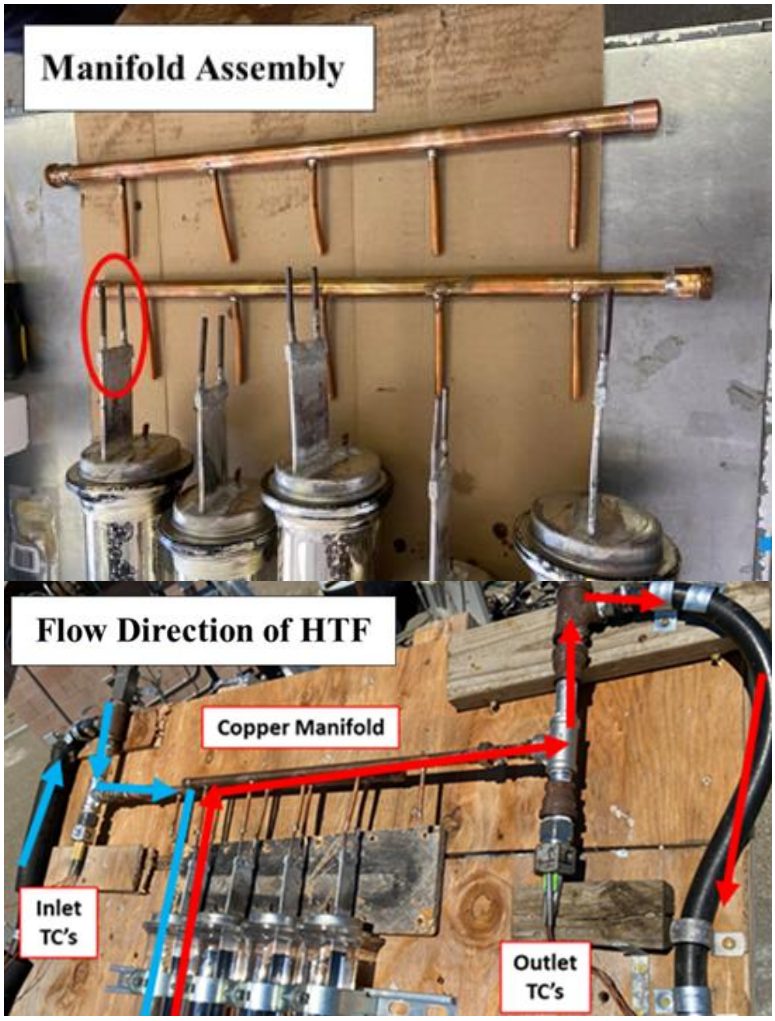

Figure 36:LEFT-- ICPC module manifold assembly with rotated minichannel position indicated with red circle && RIGHT-Fully assembled ICPC module manifold with inlet and outlet thermocouple clusters and HTF flow direction indicated with markers

The HTF is pushed, using a circulating centrifugal pump, through the Cu 'header' pipes of the manifold, to be directed into each ICPC tube, where the HTF flows directly down and back up the absorber, to pass through the other Cu 'header' pipe. A 4-tube module prototype was assembled for first prototype experimental testing, shown in Figure 37.

Figure 37: Integrated Compound Parabolic Concentrator (ICPC) module

When looking at the ICPC module directly, the whole of each tube look a blue/purple color. This is an optical illusion that demonstrates the effectiveness of the optics of the collector. The color shown in the tube is the visible color of the selective coating applied to the minichannel absorber. The technique to analyzing nonimaging optic collectors is to trace backwards from the 'target' or absorber, because rays starting at the source of energy have to end up at the absorber and therefore vice versa. When looking at the collector and see only the absorber in the mirror, it shows that any rays (within the acceptance angle) that enter the aperture will reach the absorber. Another interesting analysis of this optical illusion is the following; if the illusion is not fully blue/purple, there is light that is missing/passing the absorber. Taking a closer look, the ICPC 4-tube module has accurate optics and possibly a slight gap loss right underneath the vertical absorber. It can be reduced during assembly of tube by adding more tension to keep the absorber pushed against the glass in the correct positon. However, some gap loss is inevitable due to the thickness of the glass tube. Overall, the optical positioning of the collector looked correct and was then experimentally tested.

*3.3.2 **Test Protocols & Data***

The ICPC module was tested at the University of California, Merced (UCM) Castle Research Facility in Atwater, CA. Three experimental tests were conducted on-sun under typical conditions (>850 W/m^2) while mounted on a two-axis tracker: an optical test, thermal test, and stagnation test. Optical testing with typical conditions are performed at low HTF temperatures (close to ambient) where heat losses are low and performance is a function primarily of the optical performance of the ICPC's components. This includes both material properties and geometric positioning, and can be compared with the ray tracing optical efficiency results. Thermal testing was performed at several temperatures (100˚C, 120˚C, & 140˚C) to characterize performance under expected target operating

temperatures. Both optical and thermal experiments were conducted using flow loop calorimetry, by measuring the flow rate and temperature rise of the HTF as it passes through the ICPC module.

The thermal gain across the collector is calculated according to Equation 37, where m is flow rate (g/s), c_p is specific heat of the propylene glycol (kJ/kgK) supplied through the HTF supplier, and the temperature difference of the inlet ($T_{in,\,avg}$) and outlet ($T_{out,\,avg}$) of the ICPC manifold:

Equation 37

$$Q_{thermal} = mc_p(T_{out,avg} - T_{in,avg})$$

The product of the global solar irradiance (G) and the 4-tube collector area of 0.48 m^2 calculates the incoming solar flux on the collector's aperture (Equation 38), which can be used to calculate the instantaneous solar-to-thermal efficiency (Equation 39):

Equation 38

$$Q_{solar} = A_{collector} * G$$

Equation 39

$$\eta = \frac{Q_{thermal}}{Q_{solar}}$$

Stagnation temperature testing was performed to measure the maximum temperature the collector could reach. These three tests will provide solar-to-thermal efficiency in relation to HTF temperature to indicate the collector's performance for different applications.

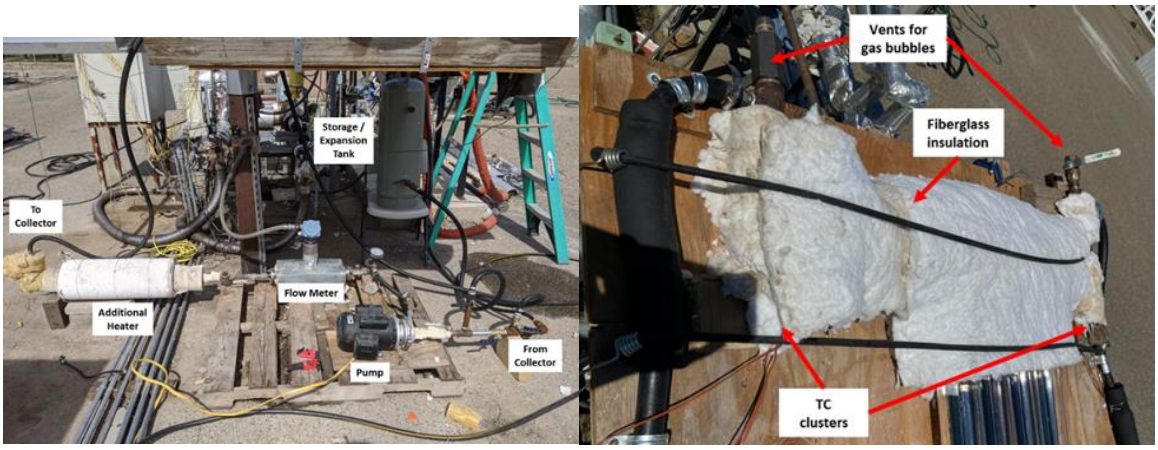

Figure 38: LEFT--Test site for ICPC module with additional heaters for temperature control, flow meter, storage, and pump indicated by markers && RIGHT- Fiberglass insulation covering all surfaces between the inlet and outlet thermocouple clusters

To measure the temperature-rise through the ICPC module, a cluster of two J-type thermocouples was installed at the 'inlet', and another cluster of three J-type thermocouples was installed at the 'outlet' of the Cu manifold (see Figure 36). Prior to testing, the individual thermocouples were calibrated using an ice bath (0˚C) and boiling water (100˚C), indicating instrumental uncertainties of ±0.1˚C (at 95% confidence). Once installed, the manifold, caps, and thermocouple clusters were fully insulated (Figure 38, right) with commercial fiberglass insulation to reduce any thermal losses to the environment. At least 5 cm of fiberglass insulation was applied to all surfaces between the inlet and outlet thermocouple clusters. Flow was measured (Figure 38, left) using a MicroMotion Coriolis flow meter, with a measurement uncertainty of 0.1% of flow. A commercial centrifugal pump was used to push the HTF through the calorimeter loop and ICPC module. A storage tank was connected to store additional HTF for thermal expansion within the HTF, and provide an escape for any gas bubbles before reaching the pump. An additional heater with temperature controller was wrapped around the plumbing to provide more heat to the HTF and control the temperature of the HTF for testing specific ranges. The HTF used is a commercial propylene glycol

(95%) with metal inhibitors (5%) to mitigate the Al, Cu, and black steel corrosion. This is an unpressurized system, the boiling point is 154˚C. Due to this constraint, testing will be limited to a maximum of 140˚C to avoid any boiling issues. The global solar irradiance was measured using an Eppley precision spectral pyranometer (PSP, Figure 40) with a relative uncertainty of ±1.6%.

The flow, temperature, and solar sensors were connected to a data logger, which recorded data every 5 seconds. Varying days of data are shown in the figure below.

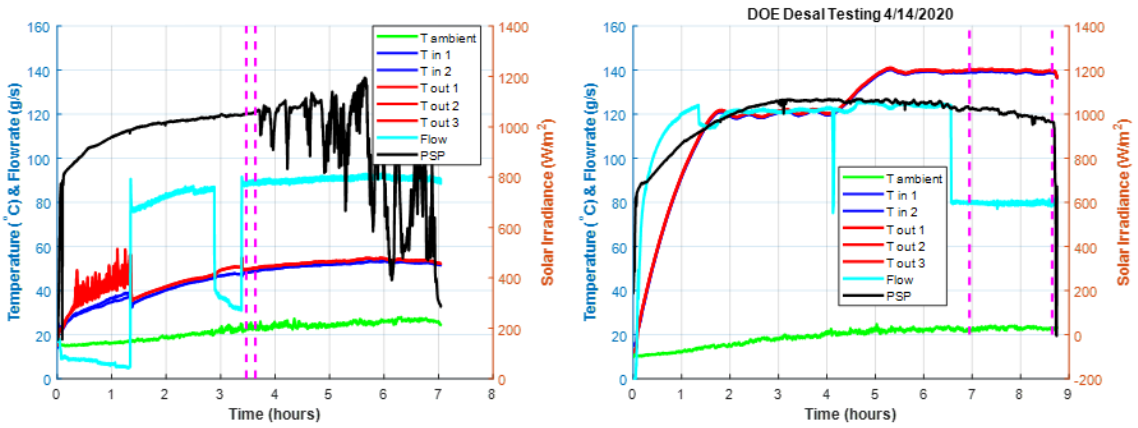

*Figure 39: Low Temperature(Left) and High Temperature (Right) Testing. *In these figures, the ambient temperature (green), inlet temperatures (blue), and outlet temperatures (red) are plotted against the left side axis along with the heat transfer fluid flow rate (cyan). The incoming solar irradiance measured by the PSP is plotted against the right side axis in black*

The left graph in Figure 39 above shows a semi-poor weather day with the HTF testing at lower temperatures (<60˚C). The figure on the right above shows a sunny day of testing with HTF at high temperatures (120-140˚C). As the ICPC module is secured to a two-axis tracker, the module was tested directly on-sun (normal to the incoming solar), demonstrating the steady high solar irradiance (shown in black – PSP) throughout the full days. Tests were performed similarly over the course of multiple days and at varying flow rates.

The stagnation temperature is the maximum temperature a solar thermal collector can reach, where the energy lost to the environment is equivalent to the energy gained from the sun. Stagnation testing was performed by inserting thermocouples into the channels of the Al absorber of an individual ICPC tube. Two T-type thermocouples were inserted about 1 m into the tube length; one thermocouple was inserted in the channel that is closest to the center of the collector's housing and the other towards the channel closest to the glass tube surface. The PSP is placed on the same plane axis as the individual ICPC tube and all-glass vacuum tube.

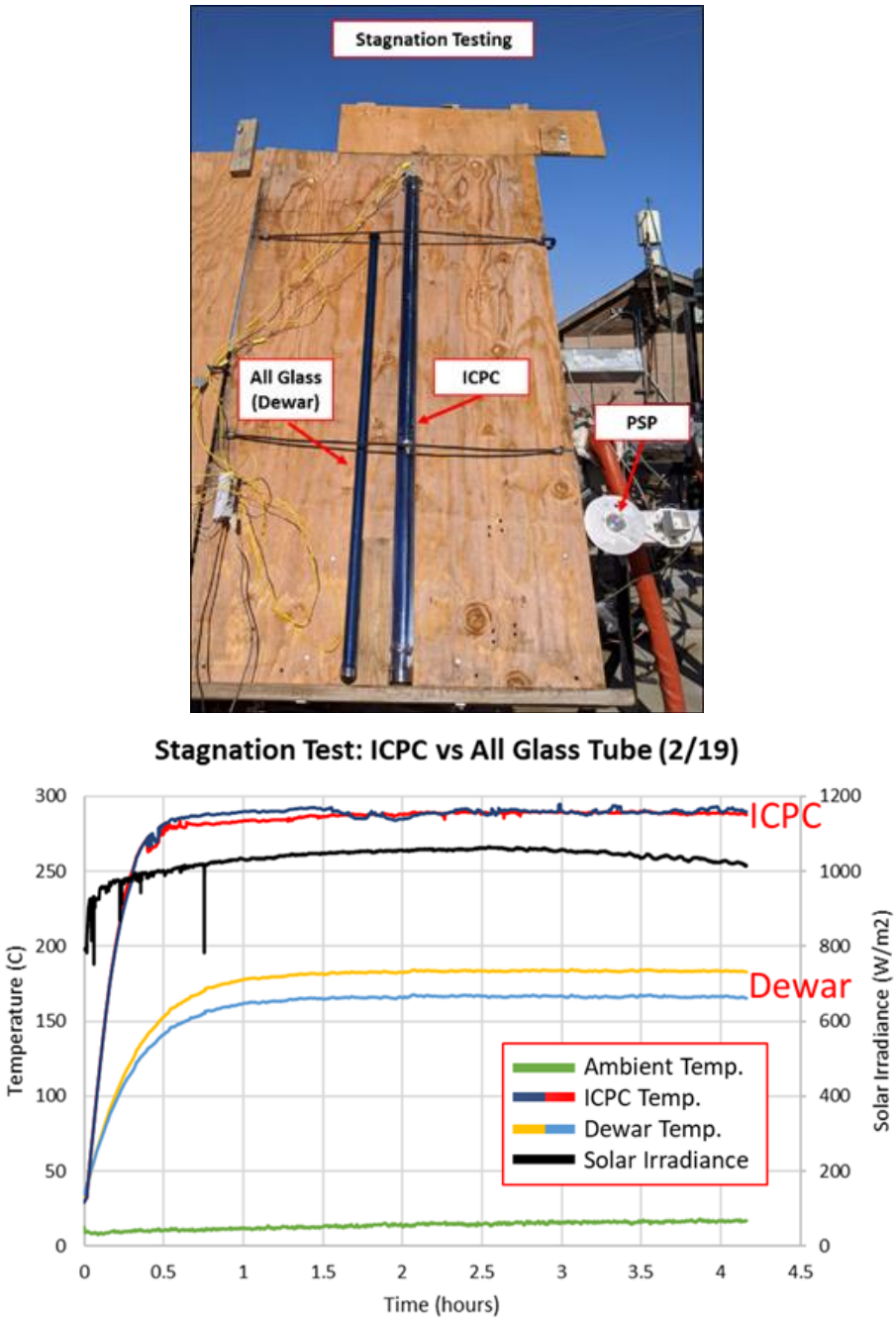

Figure 40: TOP- ICPC and All-glass Vacuum Collector Stagnation test setup with PSP indicated by marker && BOTTOM-Stagnation Results of ICPC and All-glass collector

To compare to existing solar thermal commercial collectors, an all-glass vacuum collector ('Dewar', Figure 40: left) was also tested for stagnation temperatures. This collector also had two T-type thermocouples inserted inside along the inner walls; the all-glass vacuum would have additional manifolds in a real installation that accounts for more heat losses before reaching the HTF in operating conditions. In order to obtain the stagnation temperature, the solar thermal collectors are left directly on-sun, allocating over 4 hours for the collectors to heat up to their maximum temperatures. As shown on the right of Figure 40, the results show the ICPC reached an

average stagnation temperature of 295˚C within a short amount of time (~ ½ hour) and maintained temperature over 3 ½ hours. When comparing to the all-glass collector (reaching a maximum average of 180˚C), the ICPC is capable of reaching higher temperatures up to 295˚C.

3.4 *Discussion and Analysis*

The solar-to-thermal efficiency results of the ICPC four-tube module's optical and thermal testing are shown and discussed in the next section. Along with the experimental results, updated thermal models are also discussed and compared with previous ICPC design's performance. A cost estimate is included to demonstrate the ICPC's potential to compete with low cost fossil fuels.

3.4.1 Performance

Using the test site and the equations discussed previously, the data was processed to determine the instantaneous solar-to-thermal efficiency of the ICPC module at varying temperatures. All test results and models are plotted in Figure 41, with error bars incorporating uncertainty analysis based on sensor uncertainties. Experimental optical efficiency results are depicted in blue (low temperatures where heat loss is minimal), thermal efficiency results are plotted in red, and the stagnation (maximum temperatures collector can reach and heat input is equivalent to heat loss) results are in green. The original estimated single-tube performance model using Equation 1 discussed previously (red dashed line) was updated to incorporate convective losses through the fluid and copper manifold, along with conductive losses through the 5 cm thick fiberglass insulation and later to the environment (depicted as dotted blue line, Figure 41); this models the additional losses through the module system. The original model is a tube-only model which accounts only for optical and radiation losses inside the ICPC glass tube, where the updated model shown with a blue dashed line in Figure 41 incorporates losses within the manifold and 4-tube module as a whole system.

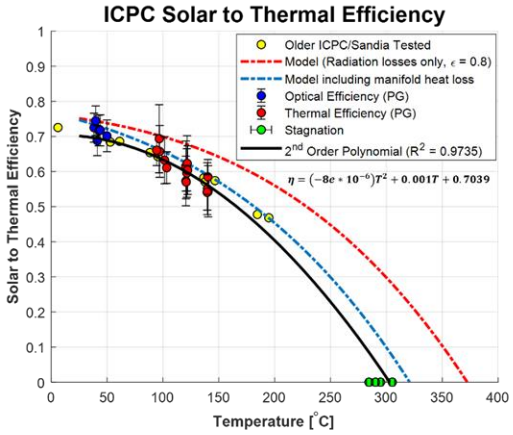

Figure 41: ICPC solar-to-thermal efficiency experimental results, thermal models, and best fit curve, along with Sandia-Tested ICPC (or 'older' ICPC) results [74]

A best fit curve was produced from the solar-to-thermal efficiency versus outlet HTF temperature data points (blue and red points with uncertainty bars, Figure 41) to better predict the ICPC module performance at varying temperatures (shown as solid black line and equation represented within the graph). The ICPC module discussed in this manuscript demonstrated about 60% ±4% instantaneous solar-to-thermal efficiency around HTF outlet temperature of 120˚C. Around 100˚C, the solar-to-thermal efficiency was about 65% ±6%, and at 140˚C the efficiency was about 55% ±5%. The current ICPC design is compared to experimental results of the previous 14-tube module (yellow points) sent to Sandia National Labs for testing [74], [75], which is the same design used

in the previously discussed Sacramento installation[65]–[67]. The Sandia tested ICPC module was tested similarly with the 4-tube ICPC module discussed in this manuscript, and was also tested on a 2-axis tracker. The experimental results of the Sandia tested module follow the updated thermal model indicated as a blue dotted line, validating the model. As shown in the figure, the current ICPC design has extremely similar results to the older 14-tube module (Sandia tested results of approximately 64% at 95˚C, 58% at 146˚C).

However, the model from the best fit curve (black line) and stagnation results (green points, averaged at 295˚C) of the ICPC indicate there are more thermal losses at higher temperatures compared to the updated model (blue line) and the Sandia tested results (yellow points). The 4-tube ICPC module does demonstrate slightly lower performance at higher temperatures (>140˚C) when compared to the Sandia tested module, which could be a result of slightly poor functioning selective coatings. As the absorber reaches higher temperatures, the selective coating should limit its radiation losses with expected emissivity of 0.08. The performance of the selective coating could be slightly less than expected, which would result in higher radiative losses at higher temperatures. The results also show the 4-tube ICPC module may be performing at a lower optical efficiency of 72% ±4% at 43˚C, which could be a result from 'gaps' or 'misaligned' absorbers (ray tracing results indicate optical efficiency of 75.6%, Figure 36). If the minichannel absorber is slightly bent or deformed during the manufacturing assembly process, there could be optical 'gaps' where light will miss the bent/deformed absorber and be reflected back to the environment. Certain improvements to make at the manufacturing stage would include re-evaluating the emissivity of the selective coating and improving absorber handling to prevent any deforming. More supports could also be added within the individual tubes to further support the optical absorber (which may be unnecessary with manufacturing improvements). As mentioned previously, minichannels are recent innovations as solar thermal absorbers due to their cost-effective production and leak-proof performance, however further analysis of the soldering connections on the minichannel absorbers are needed to determine the risks of blockages of the channels and heat transfer load losses. However, the optics are performing at a high experimental efficiency and there is only a slight differentiation between the ray tracing (75.6%) and the experimental results (72%±4% at 43˚C), and the flow of the HTF did not seem to be blocked. The optical efficiency is not presenting a major constraint and functioning acceptably. Since the ICPC is an evacuated collector, possible applications can be higher temperatures (>100˚C) and radiative losses should be explored in order to get the most heat possible from the ICPC.

The 4-tube module has experimentally demonstrated thermal heat up to 140˚C at efficiencies >55%, with experimental instantaneous solar-to-thermal efficiencies of 72%±4% at 43˚C, 65% ±6% at 95˚C, 60% ±4% at 120˚C, and 55% ±5% at 140˚C. The ICPC is capable of reaching a maximum temperature of 295˚C.

*3.4.2 **Cost Estimate***

An estimate of capital costs, annual operation and maintenance costs, and annual thermal output is described in this section in order to demonstrate the potential levelized cost of heat (LCOH) for the ICPC collector at operating temperatures of 140˚C based on the ICPC experimental results shown in Figure 41. To calculate LCOH, the following Equation 40 is used:

Equation 40
$$LCOH = \frac{(Installed\ Cost * FCR) + Annual\ O\&M}{Annual\ Thermal\ Generation}$$

The fixed charge rate (FCR) is a factor that includes assumptions regarding financing, tax, and inflation and for this calculation is assumed 0.083/year for a 25-year lifespan. The annual thermal generation (ATG) is estimated using the following equation:

Equation 41 $$ATG = GTI * 365\ days * \eta_{operating\ temp} * Thermal\ efficiency\ of\ system$$

The daily annual average global tilt irradiance (GTI) is assuming a site of Merced, CA, with a GTI of 5.82 kWh/m^2/day. The thermal efficiency of the system is assumed 85% to consider the additional losses to the environment of a full system compared to a modular system. The estimated annual thermal generation for the ICPC at 140˚C is 935 kWh/m^2/year.

The annual operation and maintenance (O&M) is assumed to be \$3.11/m^2, which is typical variable O&M costs of commercial solar flat plates. The 'installed cost', used in Equation 5, is the sum of the capital costs of an ICPC solar field, balance of system (BOS), and installation costs. The ICPC can be mass produced at \$5.87/tube based on quotes and material costs. The cost of assembly of ICPC modules including manifolds, insulation, collector frame, and additional miscellaneous pieces, are estimated to be \$38.24/module similar to commercial hot water systems (a single module is made up of 20 tubes and has aperture area of 2.44 m^2, this area is active area of the collector that is accepting light rays and does not include land area needed for shading). Therefore, the total solar field cost is estimated as \$65.54/m^2. The total BOS cost is estimated at \$26.96/m^2 and includes the HTF, pump, filters, plumbing materials, instrumentation, insulation, and weather proofing based on system dimension assumptions and quotes. The installations costs were estimated using installations costs of commercial parabolic troughs. Assuming a permanent installation on the ground, site preparation for this estimate included clearing, grubbing, ground leveling, and labor (assuming labor of \$30/hr) with a resulting estimate of \$51.69/m^2. The cost estimates and LCOH are summarized in Table 9 below.

$\eta_{140^\circ C}$	55%	Annual O&M	\$3.11/m2
Thermal efficiency of system	85%	Solar Field (ICPC)	\$65.54/m^2
GTI (Merced, CA)	5.82 kWh/m^2/day	BOS	\$26.96/m^2
Estimated annual thermal generation	993 kWh/m^2/year	Installation costs (site prep & labor)	\$51.69/m^2
FCR	0.083/year	LCOH	\$0.015/kWh

Table 9: Cost estimate summary of ICPC with calculated LCOH highlighted in yellow cell

From the cost estimate, the ICPC has potential of providing heat up to 140˚C at \$0.015/kWh. This cost estimate is only an estimate and annual generation is based on modular thermal efficiency: larger-scale testing is needed to obtain more accurate thermal system performance and additional unknown costs (i.e. specific labor, permitting, contracting, etc.). There are also areas where the costs can be re-evaluated and possibly lowered. The components at makeup ICPC modules are made of low cost materials like glass and aluminum and seem to have bottomed-out in cost (\$65.54/m^2), however further design alterations could potentially reduce module material costs: for example, the ICPC can be designed with a flat installation configuration, which would reduce frame material. A larger scale installation is needed in order to better and more accurately understand system thermal performance and daily output, and find where more cost reductions can occur.

A food processing commercial company quoted the team of paying as low as \$0.015/kWh for heat within the San Joaquin Valley in Central California (an area/state with extremely low prices for natural gas in the US). Although further cost reductions can and will be explored in the future, the preliminary LCOH of \$0.015/kWh is highly attractive when competing with the low prices of alternative fossil fuels.

*3.4.3 **Next Steps***

The 4-tube module discussed in this manuscript is the first round of prototypes for this specific ICPC design, therefore larger scale manufacturing must also be demonstrated. The solar-to-thermal efficiency results discussed in this manuscript are modular level, and do not include larger system

performance; which will include additional thermal losses, varying HTF flow conditions, and increased risk of leaks throughout the plumbing.

Testing at an array scale will also provide more accurate readings from temperature sensors with a larger temperature difference between the inlet and outlet. Therefore, the research team is currently testing and analyzing the daily energy output of a 12 kW array made up of the 228 individual ICPC tubes. The longevity of the manufacturing processes (i.e. vacuum integrity, soldered connections, metal-glass seal) will also be analyzed, and the team plans to publish updated results and findings in a follow up manuscript.

Current publications of solar thermal energy collectors are limited in information about installed larger scale array performance or detailed cost analyses, so future work will incorporate the array results, updated annual thermal generation and cost estimate, and a further look into more applications.

3.5 *Conclusion*

The team designed a low cost, high efficiency solar thermal collector using nonimaging optics, vacuum insulation, and aluminum minichannels, called the integrated compound parabolic concentrator (ICPC). The ICPC demonstrated instantaneous solar-to-thermal efficiencies of 72% ±4% at 43˚C, 65% ±6% at 95˚C, 60% ±4% at 120˚C, and 55% ±5% at 140˚C. This technology is a promising alternative renewable technology to deliver heat up to 140+˚C at a potential LCOH of $0.015/kWh for thermal applications, and a low module capital cost of $65.54/m^2. The ICPC has the potential to compete with fossil fuels and displace those fuels to account for 44% of the industrial heat temperature demands.

If coupled with storage, the ICPC can be a low cost, dispatchable, renewable heat source with applications in solar thermal desalination for water treatment and industrial processes across the globe (due to the nonimaging concentrator accepting both direct and diffuse light).

The ICPC, made up of a combination of low cost materials, vacuum insulation, and nonimaging optics, has been demonstrated at modular level in this manuscript, and shows potential of mitigating GHG emissions from the use of fossil fuels in large heat demand sectors, such as industrial processes requiring temperatures up to 150˚C and thermal desalination.

3.6 *Acknowledgments & Disclaimers*

A special acknowledgement and thanks to Robyn Lukens, Souvik Roy, Dr. James Palko, and Dr. Gerardo Diaz for the support and guidance throughout this project.

This material is based upon work supported by the U.S. Department of Energy's Office of Energy Efficiency and Renewable Energy (EERE) under the Solar Energy Technologies Office (SETO) Award Number DE-EE0008399. This manuscript was prepared as an account of work sponsored by an agency of the United States Government. Neither the United States Government nor any agency thereof, nor any of their employees, makes any warranty, express or implied, or assumes any legal liability or responsibility for the accuracy, completeness, or usefulness of any information, apparatus, product, or process disclosed, or represents that its use would not infringe privately owned rights. Reference herein to any specific commercial product, process, or service by trade name, trademark, manufacturer, or otherwise does not necessarily constitute or imply its endorsement, recommendation, or favoring by the United States Government or any agency thereof. The views and opinions of authors expressed herein do not necessarily state or reflect those of the United States Government or any agency thereof.

Chapter 4. 12 kW array analysis

Note: This chapter has plans to be converted and submitted once the Chapter 3 manuscript is published.

4.1 *ICPC array installation*

With the modular performance described in Chapter 3 being bench scale prototyping of the ICPC, the next step is upscaling size. An array sized at 12 kW, made up of 228 ICPC tubes, was constructed in order to determine daily generation at operating temperatures above 120˚C with system wide thermal losses, and establish installation and system design prototyping steps. The quality of the ICPC tube vacuum is summarized to demonstrate improvement in the manufacturing stage is still needed for the ICPC.

4.1.1 Individual investigation and reflector application

Although many iterations of the ICPC have been explored, the flow through minichannel absorber proved to be the ideal choice. An aluminum heat pipe absorber was explored thoroughly, a reliable quality, non-leaking heat pipe supplier with the specific dimensions and design could not be found. The heat pipe crimping using ultrasonic welding to seal the phase change HTF inside was not permanent, and the HTF would leak out over the course of 1-3 thermal cycles. This made them unreliable for the absorber choice, and the flow through configuration was then adopted.

With module testing completed, an array was designed and sized at 12 kW to demonstrate additional losses that would occur at a system level for solar thermal collectors. These additional losses include additional conductive and convective thermal losses to the environment through the plumbing lines and sensors. To build the 12 kW array, a total of 375 ICPC tubes were received from the supplier at the Castle Airbase Campus. These tubes came in large boxes of individual ICPC tubes that have been fully assembled with selectively coated absorbers, metal glass seal with vacuum, and soldered manifold connections. These connection points are shown in Figure 42.

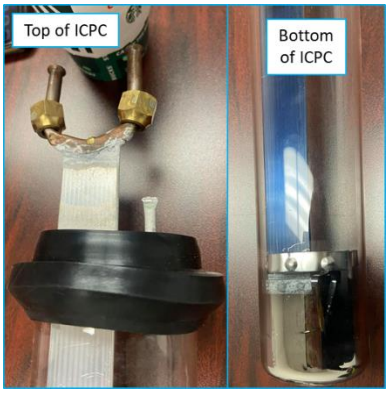

Figure 42: Close up image of the copper to aluminum solder joint and aluminum cap sealed to the housing glass tube (Left) & the bottom of the ICPC with the gas-getter and aluminum u bend solder joining with the selectively coated minichannel with a blue purple appearance

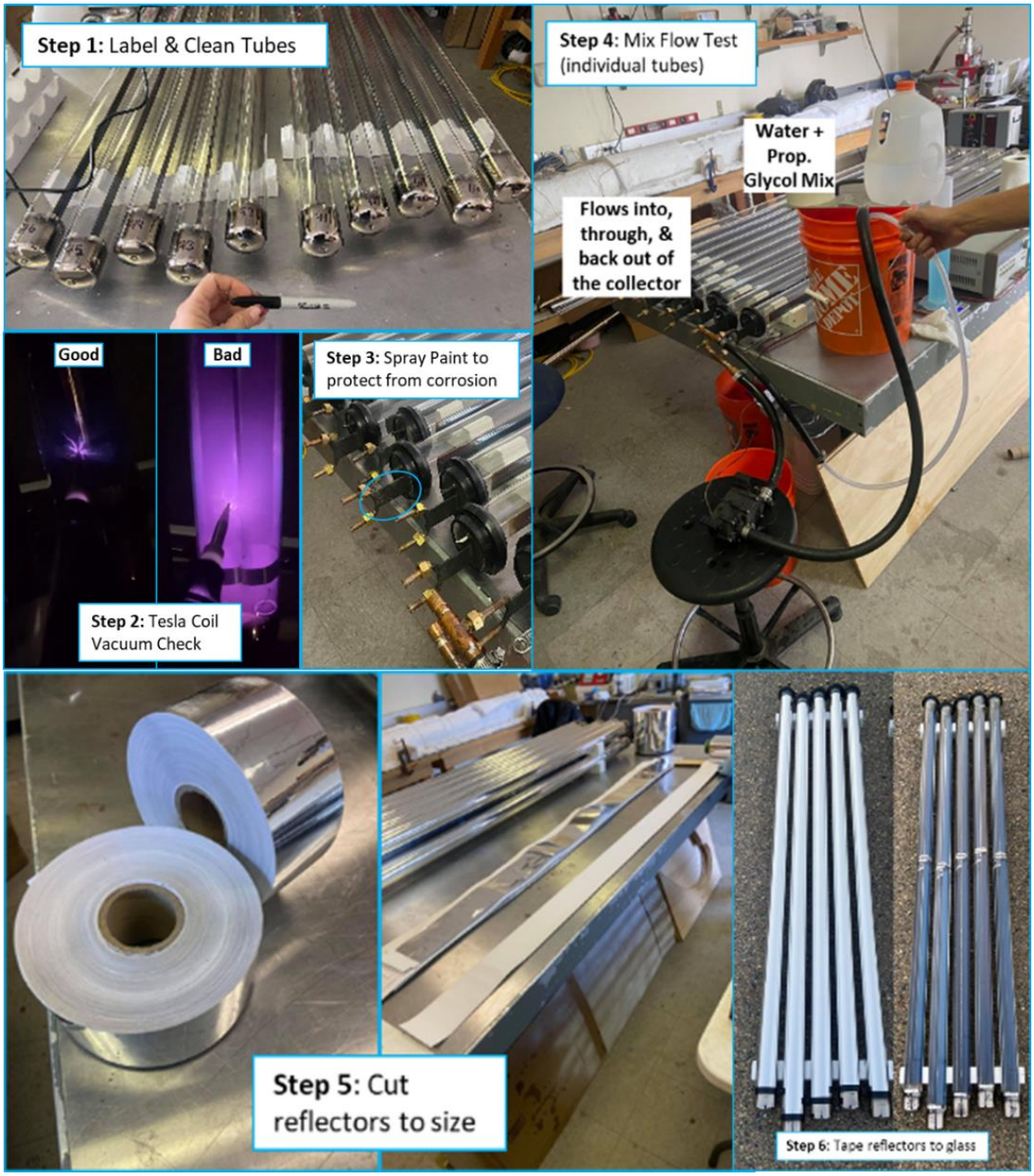

Figure 43:Outline of steps for individual tube inspection and reflector application

Once the tubes were unpacked, each were labeled and the vacuum was checked with a tesla wand, shown in Step 2 of Figure 43. It's important to check the vacuum in order to select the ideal ICPC tubes to make up the 12 kW array. A simple method to check for leaks in glass to glass seals is with a Tesla coil leak detector, and these methods can be referenced from PH Plesch 'High vacuum techniques for chemical syntheses and measurements'. Tesla coil leak detectors produce high voltage AC at low current. When the Tesla coil tip is placed on the glass tube with vacuum seal, the tip will spark and ionize the low pressure gas remaining inside the device. Any small leaks in

glass to glass seals will result in the sparks concentrating to the point where the leak is located when the high voltage tip is brought close by. The most accurate way to leak check (but most thorough, and it works with all types of seals) is to use a mass spectrometer to detect helium. As the device under test is pumped by the helium leak detector, a flow of helium gas is brought near the seals to be checked. If the helium leak rate jumps up every time the helium gas is brought near a seal, then you have found a problem. However, this method is too expensive and the tesla coil is reliable and cost effective.

Out of box, a total of 29 tubes had poor vacuum. This could have been from errors during assembly in manufacturing, or during shipping.

The Cu to Al soldered U-bend (see left image of Figure 42) was soldered by hand and have a high risk of the solder blocking the minichannels within the Al absorber. Therefore, each tube was connected to a propylene glycol water mixture line pumped with a 12 V DC pump (see step 4, Figure 43). Once the tube was connected, the pump was turned on, and the flow rate of the 50/50 propylene glycol mixture was manually measured using a stop watch, small contained, and mass scale. Each flowrate was recorded and summarized in Table 10.

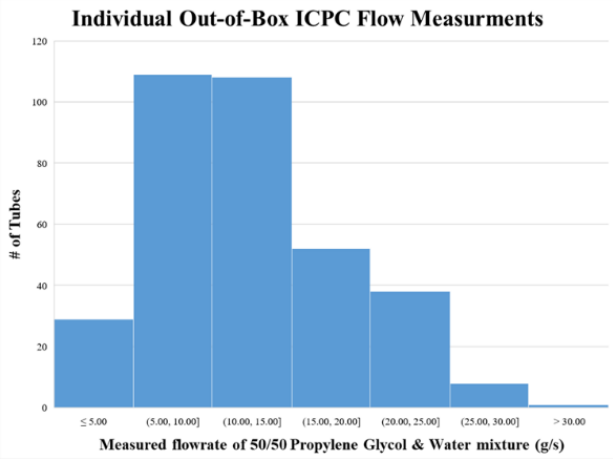

Flow inside individual tube	# of Tubes
≤ 5	29
5 ~ 10	109
10 ~ 15	108
15 ~ 20	52
20 ~ 25	38
25 ~ 30	8
> 30	1
Total with vacuum	345

Table 10: Individual ICPC tube flow measurement summarized into increments of 5 g/s. Note, the flow inside individual tubes is recorded in units of g/s. A bar graph representation is included for visual representation.

From the flow measurements of the 345 maintained vacuum tubes, it was found that about 63% had flows between 5-15 g/s and 15% had 15-20 g/s (accounting for a total of 269 tubes). When constructing the array, these 269 similar flow (5-20 g/s) and good vacuum group were used to make up the 12 kW array.

After flow was recorded, reflectors were manually applied to the bottom half of the collectors (absorber orientation now in the 3 o'clock or horizontal configuration shown in Figure 30). The reflector is a Mylar laminated sticking surface, an aluminum based material with reflectivity around 88-90%, that was lined up and smoothed over the glass tube by hand (see Step 6, Figure 43).

Important note to those who explore metal glass seal with lead; the ICPC tubes CANNOT be left outside (regardless of what the supplier says). An additional 60 tubes (from the available 269 tubes) were lost when the supplier affirmed they could be stored outside and exposed to the elements. A slight rain on the exposed metal glass seal caps introduce water corrosion to the lead within the seal, making those tubes lose vacuum. Due to this, an additional 19 tubes were pulled from the 20-25 g/s range to make up the total 228 needed.

4.1.2 Module design change

Previously the modules were designed with an upright collector in a north-south orientation. This requires a frame with load and leg supports to angle the collector at latitude of testing location (assumed 37˚ for test site of Castle Airbase in Atwater, CA, USA).

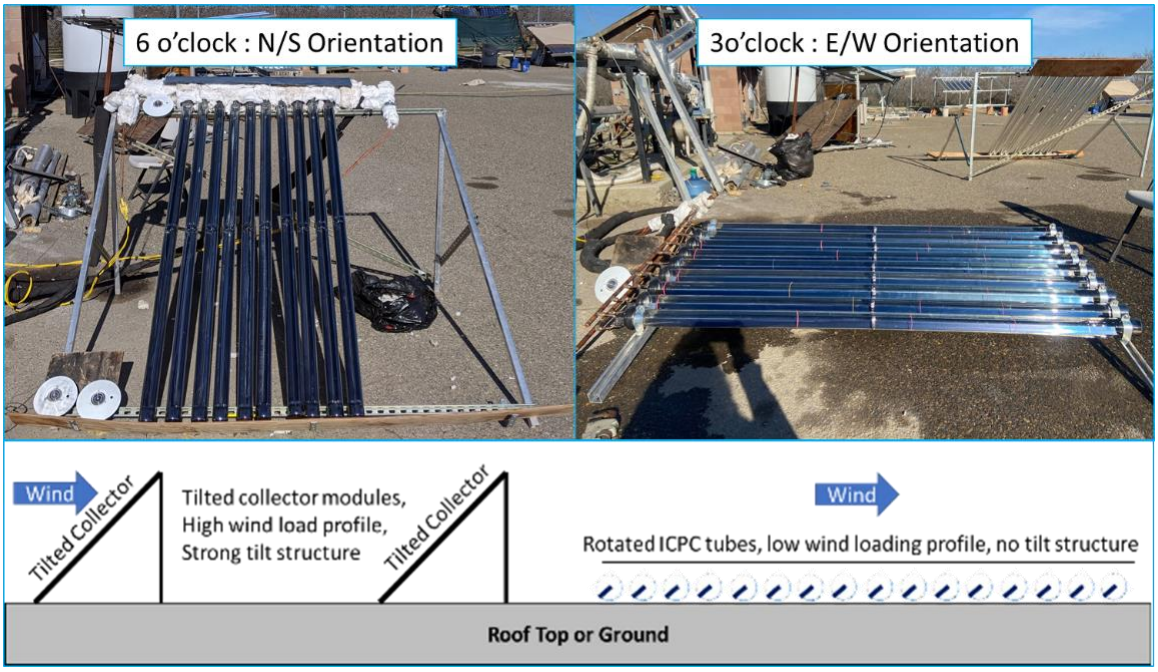

Figure 44: Installation orientation change from modular performance to array performance

For the array, the modules were rotated and re-designed into a low standing or flat thermal collector. By changing the aperture orientation to horizontal or "East-West" orientation and rotating the minichannel absorber to the 3 o'clock orientation, the frame is minimized to tube and manifold supports. By reducing material in the frame structures, the overall capital cost is reduced for the collector. This orientation of flat collector changes the variation in thermal efficiency. A side by side comparison of optical efficiency is shown in the Figure 45.

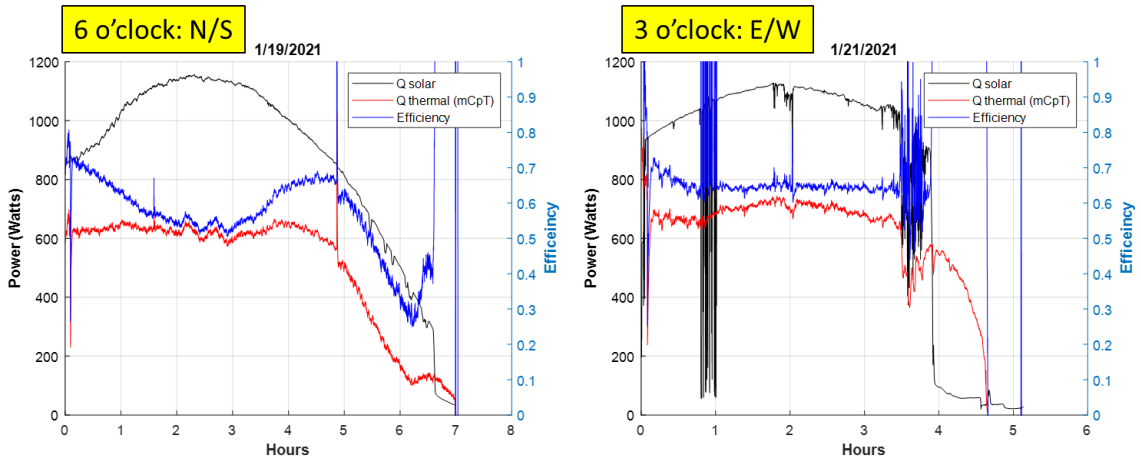

Figure 45: Measured instantaneous solar-to-thermal optical efficiency of both the North-South and East-West orientation

Due to the ICPC's acceptance angle of ±90˚, the aperture accepts all direct and diffuse light, making it adaptable to orientation changes. As shown in the data, the optical efficiency of the East-West collector is steadier throughout the day compared to the North-South collector. The maximum and minimum measure instantaneous solar-to-thermal efficiency averages higher for the East-West over the North-South. Therefore, the East-West orientation was used in the array due to higher efficiencies and cost reductions in frame materials.

Due to the supplied copper manifolds from the manufacturer, the rotation of the ICPC tubes within the module were limited. Therefore, the modules could not be completely flat and an average height of 1 ft legs made from bricks were used to tilt the aperture area of the module to latitude of the test location.

*4.1.3 **Array fabrication***

To make up the 12 kW array, 12 modules made up 19 ICPC tubes were assembled manually at test site. Originally, the modules were design with an even 20 tubes, but the supplier sent pre-brazed Cu manifolds of 19 ports. When constructing the modules for the array, the tubes with the most similar flows (pulled from the source of 269 tubes mentioned in Section 4.1.1) were coupled together to make up the individual 12 modules.

Figure 46: Images of the fabricated frames, manifolds, and manifold supports of the ICPC array

Aluminum square tubes with 1/8" thick walls were manually measured, cut, drilled, and assembled into 12 frames. The provided manifolds had to have connections brazed to connect the manifold into the system. The 19 tubes modules were piped in parallel flow and threaded with the flanges to the Cu header pipes shown in 2nd image from the left of Figure 46. Additionally, once the tubes were placed on the frame and connected to the Cu manifold via flanges, the tubes were secured with a thin aluminum strap at the ends of the glass tubes. The manifolds were secured to the frame with U-clamps, unistrut, and calcium silicate insulation pipe supports.

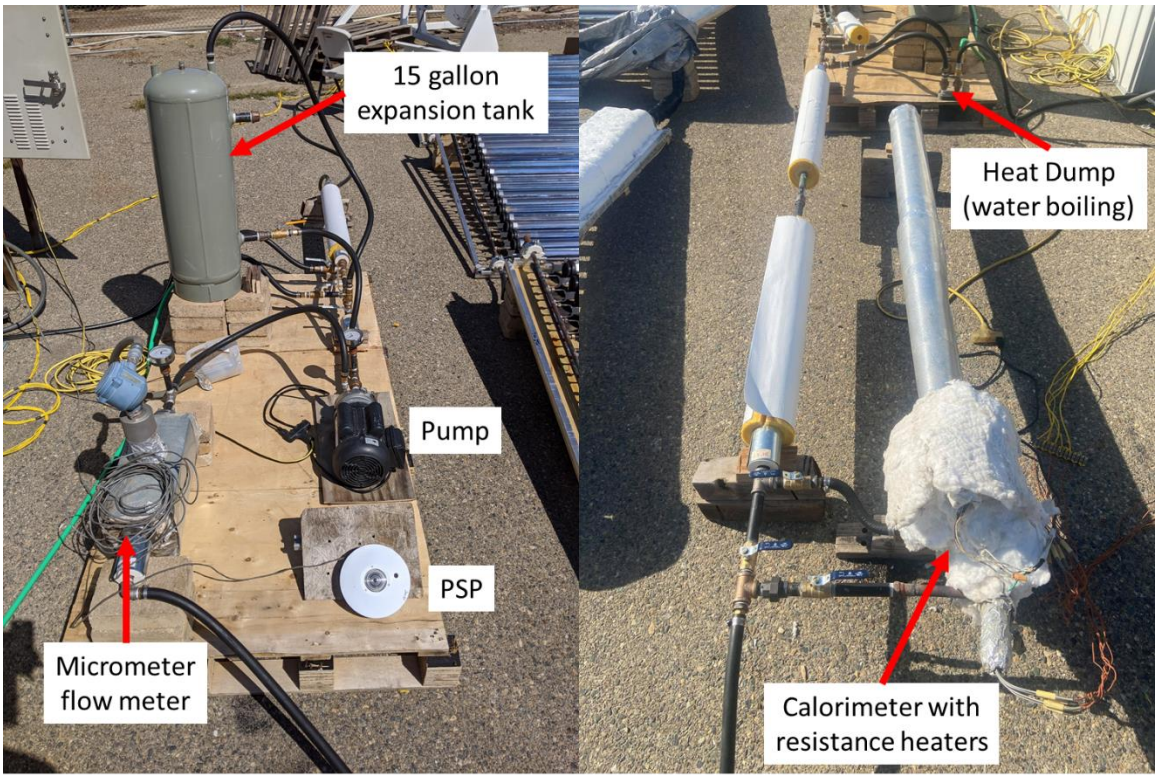

Figure 47: Array system installation includes the sensors, instruments, loggers, heat load, and resistant heater calorimeter

The PSP, pump, flow meter, data logger, and expansion tank were re-used from Chapter test rig. A colorimeter was added with 2 resistant heaters and an all glass vacuum tube with additional fiberglass insulation wrapper around the all glass vacuum tube. The calorimeter is used to determine the specific heat of the heat transfer fluid, a method thoroughly explained by Widyolar [49].

As for the temperature measurements, clusters of 5 K-type thermocouples were placed at the inlet and outlet of the array to measure the temperature rise throughout the total 12 modules.

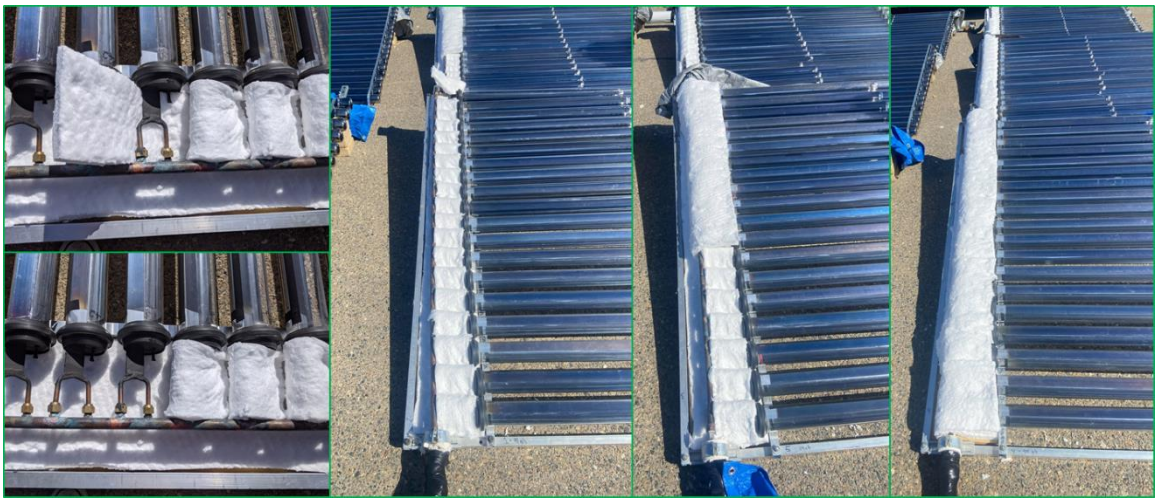

Figure 48: Full insulation process of manifold with a minimum of 2" of insulation was secured around the copper manifolds

To get the ideal system performance results, thermal losses must be minimized. In order to do so, a minimum of 2" of fiberglass insulation was wrapped around all plumbing, manifolds, Cu to Al solder joints, and caps. Shown in Figure 48, even individually wrapped the manifold sections of each ICPC tube within each module. From the image below, 3 modules were piped in series and 4 'banks' of 3 modules each were plumbed in parallel in order to combat pressure drop throughout each module and bank. The banks will be referenced as Bank 1-4 starting from left to right.

Figure 49: 12 kW ICPC array with insulation and weatherproofing

As shown in Figure 49, all plumbing between the inlet and outlet thermocouples were heavily insulated. Additionally, the full system's plumbing was insulated with a combination of fiberglass insulation and calcium silicate insulation to prevent heat losses. The full system must be insulated to understand the system performance. Insulation was also weather proofed, in order to protect from weather and any possibility of getting wet. Polyester tarps were used at the end of the day to cover each module and prevent stagnation and exposure to elements when not testing the array. The tarps are meant to be a temporary covering method and will need further designing or methods to negate the need for covers will be needed to get this system fully commercialized.

The array was finalized with the parameters summarized in Table 11.

Array configuration	East-West
# of ICPCs per module	19
# of modules in array	12
Module aperture area	2.26 m^2
Array aperture area	27.1 m^2
Array tilt angle	37˚ (latitude)
Array azimuth angle	15˚ south-west

Table 11: Summary of finalized array installation parameters

4.2 *Array performance*

This section summarizes the array thermal performance. The instantaneous solar-to-thermal efficiency is evaluated along with the daily efficiency.

4.2.1 Array efficiency and daily thermal generation

As mentioned, the inlet and outlet 5-thermocouple clusters measure the temperature rise across the array, while the PSP measures the on-sight total global solar irradiance on the same plane as the aperture plane of the array. The Coriolis flow meter measures the flow rate of the RhoGuard propylene glycol with metal inhibitors mixture, and a K-type thermocouple actively measures the ambient temperature. The total 5 days of testing data are shown in Appendix C, and one day is shown in Figure 50.

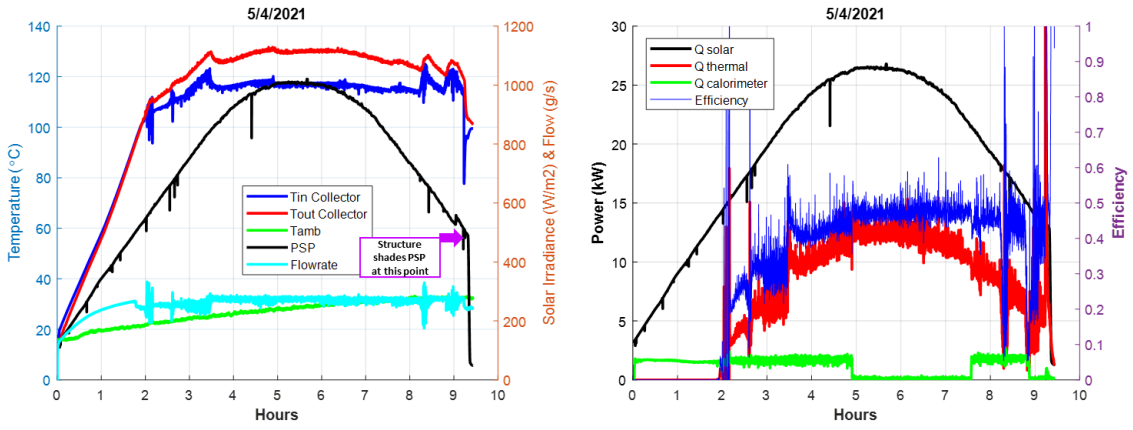

Figure 50: Data from full-day testing of 12 kW array on May 4th, 2021. Note the drastic decrease in teh solar irradiance caused by shading of the PSP by a shed structure. The blue line on the right graph represents the instantaneous solar-to-thermal efficiency of the array.

The calorimeter power of 2 parallel resistance heaters averaged about 1.76 kW. Multiple measurements of the calorimeter temperature difference were used to determine a best-fit curve function of the HTF specific heat and used in processing the thermal output and efficiency results of the arrays.

At outlet HTF temperatures averaging 127.8˚C ±0.3˚C demonstrated average instantaneous solar-to-thermal efficiencies of about 43% ±2.8%. To compare the system wide thermal efficiency to the modular thermal efficiency, array thermal efficiency results, annotated in magenta in Figure 51, were added to the ICPC modular performance results graph shown in Chapter 3, Figure 41.

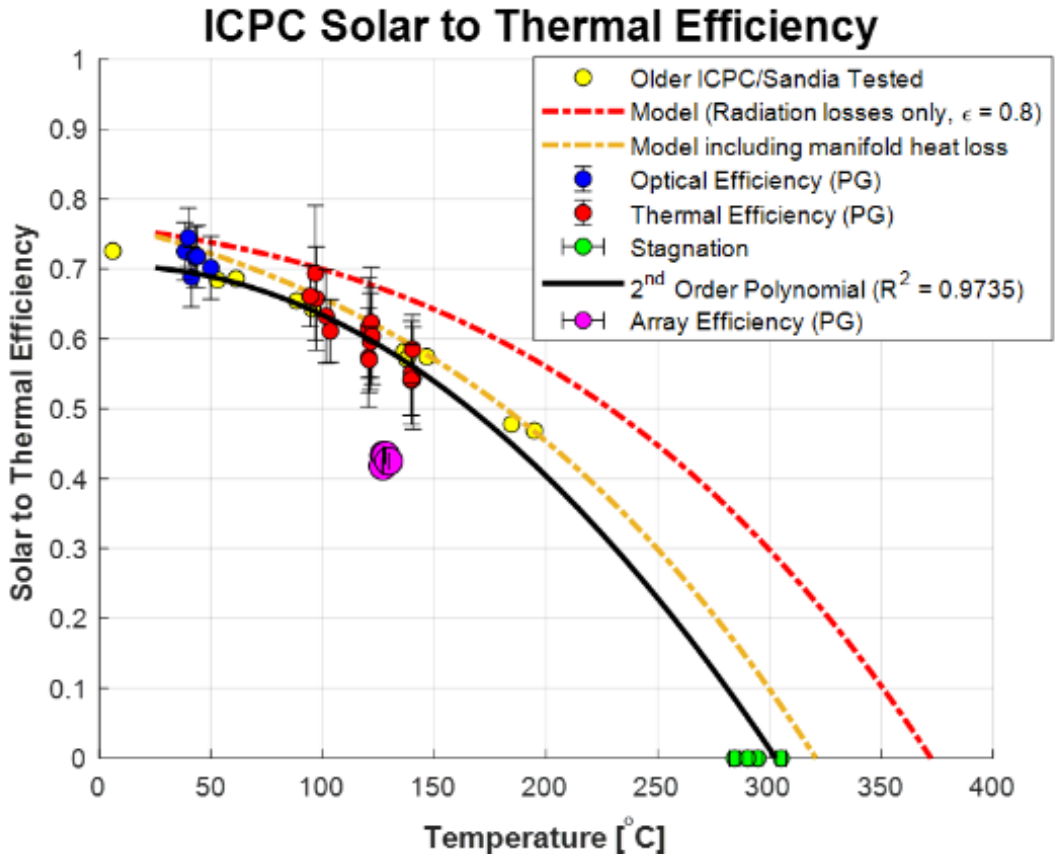

Figure 51: Array instantaneous solar-to-thermal efficiency results,

By increasing the number of thermocouples in the inlet and outlet clusters to 5, the error of instantaneous solar-to-thermal efficiency is very low with average relative efficiency error of 6.5%. The drop in performance for the array of 43% ±2.8% at 128˚C from the modular performance of 60% ±4% at 120˚C (17% efficiency drop) is due to the additional conductive and convective heat losses to the environment. The array system has much more plumbing surface area compared to the modular scale, therefore thermal losses naturally increase.

Date	5/4/2021	5/7/2021	5/10/2021	5/11/2021	5/12/2021
T*	0.113	0.123	0.118	0.116	0.118
T amb(˚C)	29.2	23.9	28.5	30.4	32.4
Average PSP (W/m2)	864	839	833	843	825
Efficiency (%)	43.3	43.4	41.8	43.3	42.5
Eta error (+/-%)	2.7	3	2.6	2.8	2.9
T fluid out (˚C)	127.3	127.4	126.9	128.2	129.6
T error (+/-˚C)	0.34	0.3	0.3	0.33	0.32
Energy out @ target temp. (kWh)	62.4	59.8	60.2	62.4	59.6
Flow (g/s)	269	266	263	270	266
Full Day solar potential (kWh)	177.6	168.8	170	171.2	168.9
Full Day thermal generation (kWh)	68.2	64.1	63.6	65.8	64.4
Daily Efficiency (%)	38.4	38	37.4	38.4	38.1
Daily Generation (kWh/m2)	2.6	2.4	2.4	2.5	2.5
Hours Generating	6.26	6.46	6.48	6.42	6.39

Table 12: 12 kW ICPC pilot array results with the total thermal output at temperatures above 120˚C and the daily efficiency representing the total daily thermal generation over the total daily solar potential are highlighted with red boxes.

Although multiple days of testing occurred, 5 days of full day and consistent data were used to analyze the performance and thermal generation of the 12 kW array, summarized in Table 10. Performance calculations used Equation 37, Equation 38, and Equation 39.

The array collector area is determined with Equation 42. During assembly and testing, 7 tubes had to be removed from the total 228 tubes due to leaking solder joints or broken glass tubes from accidental debris. Therefore, the area of 7 tubes were subtracted from the overall array aperture area.

Equation 42 $$((1.8*0.066*19)*12) - (7*0.066*1.8) = 26.25\ m^2$$

The ICPC array generated an average of about 61 kWh of thermal energy at target operating temperatures greater than 120˚C at an average flow of 267 g/s, and performed at average of 38% daily efficiency.

In summary, the daily efficiency incorporates the heat up cycle (the amount of time the collector is heating up the HTF, sensor, and plumbing) and additional thermal losses compared to the modular performance. Unlike the average efficiency at operating temperatures, the daily efficiencies encompass all HTF temperatures throughout the entirety of the day (see section 4.2.2 for equations summary). The ICPC's daily efficiency averages at 38%, with the 12 kW array of a total of 26.25 m^2 generating a range between 63-68 kWh over an average span of 6.4 hours of active solar.

4.2.2 Data analysis with error propagation equations

For measurement analysis on the inlet and outlet thermocouples of the array with error analysis, the following equations were used.

Equation 43 $$T_{in} = (T_{in1} + T_{in2} + T_{in3} + T_{in4} + T_{in5}) / 5$$

Equation 44 $$T_{in\_error} = sqrt((((T_{in1} - T_{in}).\hat{}2) + ((T_{in2} - T_{in}).\hat{}2) + ((T_{in3} - T_{in}).\hat{}2) + ((T_{in4} - T_{in}).\hat{}2) + ((T_{in5} - T_{in}).\hat{}2)) / (5-1));$$

Equation 45 $$T_{out} = (T_{out1} + T_{out2} + T_{out3} + T_{out4} + T_{out5}) / 5$$

Equation 46 $$T_{out\_error} = sqrt((((T_{out1} - T_{out}).\hat{}2) + ((T_{out2} - T_{out}).\hat{}2) + ((T_{out3} - T_{out}).\hat{}2) + ((T_{out4} - T_{out}).\hat{}2) + ((T_{out5} - T_{out}).\hat{}2)) / (5-1))$$

Equation 47 $$\Delta T = (T_{out} - T_{in})$$

Equation 48 $$\Delta T_{error} = sqrt((T_{out\_error}.\hat{}2)+(T_{in\_error}.\hat{}2))$$

Equation 49 $$T^* = (((T_{in} + T_{out})/2)-T_{amb}) ./ PSP$$

For measurement analysis on the inlet and outlet thermocouples of the calorimeter with error analysis, the following equations were used.

Equation 50 $$T_{calin} = (T_{calin1} + T_{calin2} + T_{calin3} + T_{calin4} + T_{calin5}) / 5$$

Equation 51 $$T_{calin\_error} = sqrt((((T_{calin1} - T_{calin}).\hat{}2) + ((T_{calin2} - T_{calin}).\hat{}2) + ((T_{calin3} - T_{calin}).\hat{}2) + ((T_{calin4} - T_{calin}).\hat{}2) + ((T_{calin5} - T_{calin}).\hat{}2)) / (5-1))$$

Equation 52 $$T_{calout} = (T_{calout1} + T_{calout2} + T_{calout3} + T_{calout4} + T_{calout5}) / 5$$

Equation 53 $$T_{calout\_error} = sqrt((((T_{calout1} - T_{calout}).\hat{}2) + ((Tcalout2 - T_{calout}).\hat{}2) + ((Tcalout3 - T_{calout}).\hat{}2) + ((T_{calout4} - T_{calout}).\hat{}2) + ((T_{calout5} - T_{calout}).\hat{}2)) / (5-1))$$

Equation 54 $$\Delta T_{\_cal} = (T_{calout} - T_{calin}) + 0.4386$$

Note the 0.4389 in Equation 54 is from a thermocouple calibration.

Equation 55 $$\Delta T_{\_cal\_error} = sqrt((T_{calout\_error}.\hat{}2)+(T_{calin\_error}.\hat{}2))$$

The Coriolis flow meter has a relative error of 0.1% and the PSP has a relative error of 1.6%, therefore the following equations give the error propagation of the instantaneous solar-to-thermal efficiency based on Equation 37, Equation 38, and Equation 39 (where η is thermal efficiency).

Equation 56 $$Q_{thermal\_error} = Q_{thermal} .* sqrt(((flow_{\_error}./flow).\hat{}2) + ((\Delta T_{error}./\Delta T).\hat{}2))$$

Equation 57 $$Q_{solar\_error} = Q_{solar} .* sqrt((PSP_{\_error} ./ PSP).\hat{}2)$$

Equation 58 $$\eta_{error} = \eta .* sqrt((((Q_{thermal\_error}./Q_{thermal}).\hat{}2) + ((((Q_{solar\_error}./Q_{solar})*(-1)).\hat{}2))$$

Equation 59 $$\eta_{rel\_error} = \eta_{error} ./ \eta$$

To calculate the thermal generation above 120˚C HTF temperatures, the following equations are used specifically within the temperature boundary. In other words, all data from lower than 120˚C is negated here. Note, the startScan and stopScan indicate the points where the outlet HTF lies above the target operating temperature.

Equation 60 $$thermal_{\_sum} = sum(Q_{thermal}(startScan:stopScan))$$

Equation 61 $$daily\_output = thermal_{\_sum} * 5 * (1/3600)$$

Equation 62 $$solar_{\_sum} = sum(Q_{solar}(startScan:stopScan))$$

Equation 63 $$daily\_solar\_potential = solar_{\_sum} * 5 * (1/3600)$$

The daily efficiency is determined using the following equations. The total solar potential energy and thermal generation for the full day incorporates all energy from the point when the array is uncovered in the morning and re-covered in the evening.

Equation 64 $$fullday\_thermal_{\_sum} = sum(Q_{thermal})$$

Equation 65 $$daily\_full\_output = fullday\_thermal_{\_sum} * 5 * (1/3600)$$

Equation 66 $$fullday\_solar_{\_sum} = sum(Q_{solar})$$

Equation 67 $$daily\_\eta = daily\_full\_output / daily\_solar\_potential$$

4.3 *Array discussion*

The ICPC demonstrated system performance capability of generating 61 kWh of thermal energy at operating temperatures greater than 120˚C at an average instantaneous solar-to-thermal efficiency of 43% ±2.8%. With additional thermocouples, the error is lower compared to the modular performance; however, the 17% drop in thermal efficiency (module has 60% at 120˚C) is due to additional system wide thermal losses to the environment with the additional plumbing and exposed surfaces. The ICPC's daily efficiency averages at 38%, with the 12 kW array, 26.25 m^2 aperture area, generating between 63-68 kWh of thermal energy over an average span of 6.4 hours of active solar each day (producing average 2.5 kWh/m^2 at 38%).

This instantaneous efficiency and solar thermal daily generation of the 12 kW ICPC array has potential to be improved with improved vacuum integrity, updated manifolds, and better HTF options.

It was confirmed that the largest loss of tubes comes from the grade in vacuum over time. During the first individual inspection, 7.8% out of 374 tubes arrived with poor or lost vacuum. An additional 60 tubes were lost after reflectors were attached, due to the supplier insisting the tubes could handle exposure to the elements. Turns out, they can't. The ICPC tubes with reflectors left in rain resulted in the lead holding the aluminum cap and glass tube together corroded from the water exposure, and eventually lost vacuum (this happened to a total of 60 tubes).

During array testing, gas getters were noticed to change from the grey composite to a white or clear composite, indicating vacuum loss in a total of 25 tubes of the 228 tubes that make up the array (11% of array lost to vacuum degradation). Testing was limited in time due to this high risk, high impact factor; with over 10% of array losing vacuum, the data is limited to the 5-day window in order to maintain experimental consistency. Table 13 summarizes the amounts of tubes lost in each bank of the array. The banks, made up of 3 modules in series, were previously defined in Section 4.1.3 with numbers 1-4 and labeled from left farthest bank to right farthest bank.

Total # of tubes originally installed on array :	228
Total # of tubes lost vacuum throughout running array :	25
Total # of tubes lost vacuum in Bank 1 during testing :	4
Total # of tubes lost vacuum in Bank 2 during testing :	7
Total # of tubes lost vacuum in Bank 3 during testing :	14
Percentage of tubes broken/lost vacuum of total 228 tube array: (%)	11

Table 13: Breakdown summary of tubes that lost vacuum within the array during testing

Out of those 25 tubes that lost vacuum during testing of the array, 7 of those tubes either has shattered glass tubes or leaking point at the solder connections shown in Figure 42, and were eventually physically removed from the array and their collective area subtracted from the overall array aperture area.

Total of 54 tubes arrived with bad vacuum or lost vacuum during shipping, handling, or testing out of the total 375 tubes. Making 14.4% of tubes with failed vacuum, and can be accounted for either in the manufacturing stage (i.e. machine line-up accuracy of metal-glass seal) or the longevity stage (metal-glass seal needs more improvement for mass production scale).

In total, 114 tubes experienced vacuum loss, making that about 30% of the total 375 tubes. If the ICPC is to be further improved, one of the largest risk factors is proven to be vacuum integrity.

Another issue with the current manufacturing of the ICPC are the high risks of leaks at the solder joints that make up the ICPC. These joints include the U-bend joint at the bottom of the minichannel absorber, the joint of the Al minichannel to the Al cap, and the Cu to Al joint to connect the individual ICPC collector to the Cu manifold with the use of Cu threaded flanges.

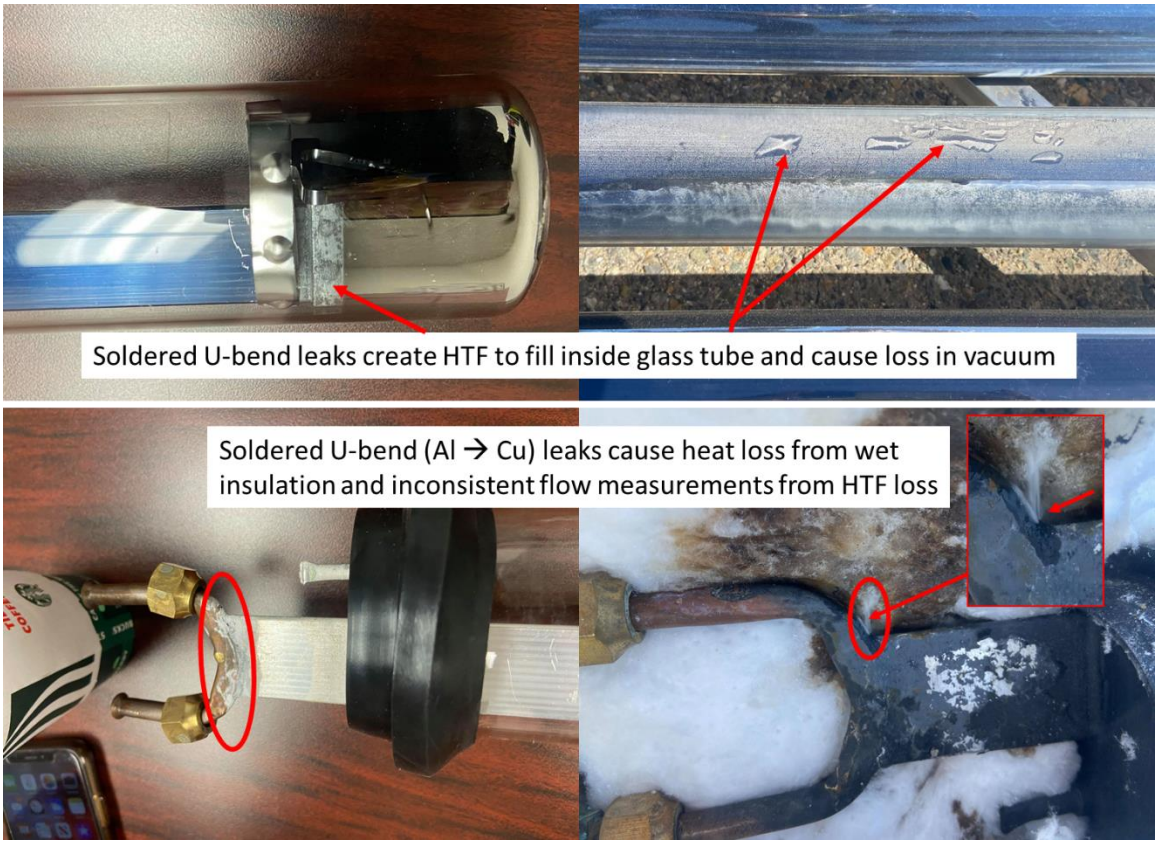

Figure 52: Leak points on the current ICPC design

These joints are corroded by water, therefore exposure to high perspiration areas can be a risk for leaking. 7 out of 228 tubes experienced leaks at these weaker soldered joints. These leaks are detrimental to the system performance, due to the loss of HTF volume and the inconsistent flow measurements. Leaking inside the glass tube, losses the vacuum, and therefore reduces the active

aperture area of the array. Leaks outside the glass tube begin to soak the insulation, creating additional thermal loads and losses to the environment.

4.4 *Updated annual generation and LCOH*

Annual solar resource and calculated global tilt irradiance (GTI) for Merced, Ca was previously estimated as 1936.1 kWh/m^2/year for GHI, 2452.2 kWh/m^2/year for DNI, and a calculated GTI of 2021.6 kWh/m^2/year [11]. Using the daily efficiency of the 12 kW array of 38%, η_{daily} (see Table 12), the array's annual thermal generation, E_{annual}, can be estimated as 784.4 kWh/m^2-year, using Equation 68.

Equation 68

$$E_{annual} = \eta_{daily} * GTI$$

In order to update the estimated LCOH from Equation 40 with array performance, the BOS, solar field, and O&M costs need to be updated. The fixed charge rate (FCR) is a factor that includes assumptions regarding financing, tax, and inflation and for this calculation is assumed 0.083/year for a 25-year lifespan.

ICPC - Glass Tube	$ 2.50	/tube	~cost of material and shaping of manifold flange connections
ICPC - Aluminum Minichannel	$ 0.50	/tube	Previous Quote
ICPC - Selective Coating	$ 0.10	/tube	Batch PVD coating on suspended minichannels
ICPC - Absorber Supports	$ 0.20	/tube	1/4" Steel strip x 5X diameter (circumference + 2D)
ICPC - Reflective Coating	$ 0.59	/tube	Previous Quote
ICPC - Glass-to-metal Seal	$ 1.29	/tube	Includes cost of end cap and thermocompression process
	$ 5.18	/tube	Note: All-glass Dewar tubes are $3/tube
	$ 103.60	/module	
ICPC Tubes Total	**$ 41.31**	**/m^2**	
Manifold - Tubing	$ 4.16	/m^2	3/4" x SCH40 Steel Tubing - 6 ft x 2 x $0.87/ft
Manifold - Insulation	$ 3.23	/m^2	Fiberfrax - 6ft x 2 ft @ $135/100 sq ft
Manifold - Jacketing / Box	$ 4.78	/m^2	Aluminum Sheet Metal - 6ft x 2 ft @ $2/sq ft
Manifold - Fittings	$ 1.99	/m^2	Solder, fittings
Manifold - EPDM Steam Hose	$ 1.20	/m^2	$3/ft @ 1 ft per module
Manifold - Assembly Labor	$ 5.98	/m^2	$60/hr @ 1/4 hour per module
Manifold Total	**$ 21.35**	**/m^2**	
Frame - Rail Mounts	$ 6.29	/m^2	1"x1"x1/8" Steel Square - 2 rails X 5.8 ft X $27/20ft
Frame - Ballast (Bricks)	$ -	/m^2	Need for brick legs eliminated with manifold updates
Frame - Angle	$ 0.54	/m^2	1"x1"x1/8" Steel Angle - 0.5 ft x 4 @ $13.5/20ft
Frame - Fastening	$ 1.59	/m^2	$4 per module estimate
Frame - Assembly / Installation Labor	$ 5.98	/m^2	$60/hr @ 1/4 hour per module @ factory OR on-site
Frame Total	**$ 14.40**	**/m^2**	

Table 14: Cost breakdown of Solar Field by component (totals highlighted in yellow cells, and sum to give solar field cost)

Table 14 shows the cost breakdown and assumptions of the ICPC fabrication (assuming an upscale in production of x10). The total solar field cost is the sum of the ICPC tubes, manifold total, and frame total an is estimated at $77.07/m^2. Some assumptions made were the improved manifolds, negating the need for bricks.

BOS - Pump	$ 1.98	/m^2	20 degree dT, 1.4 kg/s flow, 60 psi, 60% pump efficiency. Based on prev quote $419.635/kW
BOS - Pipe & Fittings	$ 5.71	/m^2	3/4" SCH 40 black steel pipe @ $0.87/ft, 2 m pipe per m2 aperture
BOS - Heat Transfer Fluid	$ 4.39	/m^2	RhoGard Ultra @ $16.7/gal (prev. quote), diluted 50/50 with DI water @ $1/gal, 0.5 gal per m2 aperture
BOS - Insulation	$ 9.84	/m^2	1/2" x 1" thick fiberglass @ $1.5 / ft (prev quote), 2 m pipe per m2 aperture
BOS - Jacketing	$ 6.30	/m^2	11.5" aluminum pipe jacketing @ $0.96/ft (prev quote), 2 m pipe per m2 aperture
BOS - Instrumentation	$ 4.00	/m^2	Assuming $1K for instrumentation out of 100 kW (250 m2) system
BOS - Heat Exchanger	$ 9.75	/m^2	$24.38 per kW of heat exchanger (prev quote), 400 W per m2
BOS - Installation Labor	$ 7.50	/m^2	$60/hr @ 1/8 hour per m2 on-site
BOS Total	$ 49.47	/m^2	

Table 15:Balance of System BOS cost breakdown

O&M - Pump Energy Cost	$ 1.38	/m^2-year	1.2 kWe pump @ 8 hrs per day @ $0.10 per kWhe energy cost
O&M - Pump Maintenance	$ 0.34	/m^2-year	1 hour labor per year inspection + $25 per year parts
O&M - Tube Replacement	$ 0.51	/m^2-year	Assuming 0.5% of tubes fail per year, 1 tube = 0.1254 m2, 1/8 hour per tube replacement labor @ $60/hr
O&M - Solar Field Cleaning	$ 0.20	/m^2-year	6 cleanings per year @ $10/hr @ 30 seconds per module
O&M Total -	$ 2.42	/m^2-year	

Table 16: Operation and Maintenance (O&M) Cost breakdown

The updated LCOH is summarized and compared to an +4.5% improved daily efficiency which is similar to the array's instantaneous efficiency performance at >120˚C.

	Current LCOH	Improved Efficiency LCOH
Annual Site GTI (kWh/m^2-year)	2021.6	
Annual Generation (kWh/m^2-year)	784.4	859.2
Daily Efficiency (%)	38	42.5
Solar Field Cost ($/m^2)	$ 77.05	
BOS Cost ($/m^2)	$ 49.47	
Total Direct Cost ($/m^2)	$ 126.53	
O&M Cost ($/m^2)	$ 2.42	
FCR	0.083	
LCOH ($/kWh)	**0.0168**	**0.015**

Table 17: LCOH calculation results with current daily efficiency compared to LCOH with an estimated efficiency improvement

With the current collector's daily efficiency, the ICPC produces heat at $0.0168/kWh. If manufacturing and quality improvements are made to the ICPC design to minimize losses and increase daily efficiency, a lower LCOH is estimated at $0.015/kWh.

Chapter 5. Dissertation Conclusions

This section of the dissertation summarizes ICPC experimental results and cost analysis for the PV/T system, 4-tube ICPC-thermal only module, and 12 kW ICPC array. Future work and awards are also discussed.

5.1 *ICPC Conclusions*

The ICPC coupled with minichannels has been demonstrated as a high efficiency nonimaging optical design ideal for solar collection and concentration. As a hybrid PV/T collector, the ICPC has been shown to cool the PV cells effectively and actively, and to transport the energy for low temperature heat use. For low temperature heat demands, relatively inexpensive PV technology, couple with affordable electric heaters beat out the ADOPTS collector (PV/T ICPC). Again, the goal is to provide a cost-competitive alternative to fossil fuels to facilitate adoption of low emission technology. The proposed technology is an economically viable option that makes this goal achievable. Other renewable technologies could be considered viable options (i.e. if there are more viable options for small installation and low temperature applications, the ICPC may not be effective being further pushed as a hybrid collector). Since the ADOPTS has no vacuum insulation, the temperature is limited and cannot be applied to other markets outside of low temperature heat demands. The max stagnation of the PV/T ICPC is 93˚C; and for comparison, the maximum stagnation of ICPC with vacuum insulation is 295˚C.

There are several performance characteristics that make the ICPC a desirable option for application in heat processes. By removing the PV and adding vacuum insulation, higher temperatures of usable heat can be delivered for applications such as solar heating industrial processes (SHIP) and solar desalination.

The 4-tube module has experimentally demonstrated thermal heat up to 140˚C at efficiencies >55%, with experimental instantaneous solar-to-thermal efficiencies of 72%±4% at 43˚C, 65% ±6% at 95˚C, 60% ±4% at 120˚C, and 55% ±5% at 140˚C. The ICPC is capable of reaching a maximum temperature of 295˚C. The estimated annual thermal generation for the module results of ICPC at 140˚C is 935 kWh/m^2/year.

The ICPC demonstrated system performance capability of generating 61 kWh of thermal energy at operating temperatures greater than 120˚C at an average instantaneous solar-to-thermal efficiency of 43% ±2.8%. With additional thermocouples, the error is lower compared to the modular performance; however, the 17% drop in thermal efficiency (module has 60% at 120˚C) is due to additional system wide thermal losses to the environment with the additional plumbing and exposed surfaces. The ICPC's daily efficiency averages at 38%, with the 12 kW array, 26.25 m^2 aperture area, generating between 63-68 kWh of thermal energy over an average span of 6.4 hours of active solar each day (producing average 2.5 kWh/m^2 at 38%).

This instantaneous efficiency and solar thermal daily generation of the 12 kW ICPC array has potential to be improved with improved vacuum integrity, updated manifolds, and better HTF options.

Vacuum reliability introduces risk and jeopardizes technology cost-effectiveness. In this study of the 12 kW ICPC array, a total of 54 tubes were received from suppliers with bad vacuum or lost vacuum during shipping, handling, or testing out of the total 375 tubes. Making 14.4% of tubes with failed vacuum, and can be accounted for either in the manufacturing stage (i.e. machine line-up accuracy of metal-glass seal) or the longevity stage (shipping, handling, etc.). In theory, the thermocompression lead metal-glass seal needs more improvement, which comes from further prototyping and development research. In total, 114 tubes experienced vacuum loss, making that

about 30% of the total 375 tubes. If the ICPC is to be further improved, one of the largest risk factors is proven to be vacuum integrity. The relatively high failure rate may also jeapordize cost effectiveness of technology adoption (if tubes cannot last and need to be replaced frequently, labor and material costs increase). Therefore, further development in the ICPC's vacuum integrity is needed.

At the manufacturing stage, the solder joints also need innovating in order to provide long lasting ICPC collectors that can experience daily thermal cycles without corroding and leaking.

As mentioned, the absorber rotation in the design change from the N-S orientation collector to E-W flat collector (Figure 44) was limited by the pre-brazed provided Cu manifold header pipes. Therefore, future prototypes of the ICPC can have specifically designed manifolds to allow each space between each individual tube to rotate aperture plane to latitude of installation site. Some innovation to simplify the installation process and guarantee the correct aperture plane angle will be needed to optimize the installation process, and in return optimize the installation costs.

The HTF used was chosen specifically due to the metal inhibitors incorporated, and limited the collector to the HTF's boiling point of 150˚C. Mineral oils are too dense and would not flow at lower fluid temperatures in the small channels within the Al minichannel absorber. Although water would be the ideal candidate (due to its density, heat transfer properties, and low cost), but the low cost material of Al that makes up the ICPC is highly corrosive to water. Therefore, a propylene glycol mixture with metal inhibitors was selected. If a water HTF with Al and Cu metal inhibitors can be cost effective, the heat transfer within the collector would be improved (merely due to the increased heat transfer properties of water compared to propylene glycol mix). Further testing of fluids would be ideal, specifically pressurized mixtures of PG and water with metal inhibitor should be explored for future ICPC installations.

The thermal performance of the ICPC has been tested with a variation of designs, insulations (argon, vacuum), and materials: the ICPC has been thoroughly demonstrated to be capable of capturing solar radiation to provide useable heat at operating temperature for solar desalination and industrial process heat need up to 140˚C. Another round of research and development (R&D) funding exploring the manufacturing and material improvements would confirm the ICPC's commercial value as low cost, low carbon emitting heat generation.

The combination of nonimaging optics, aluminum minichannel absorbers, and vacuum insulation has been demonstrated within the ICPC as a viable, low cost solar collection technology for operating temperatures up to 150˚C. With the summarized improvements, the ICPC has the possibility of supplying as low as $0.015/kWh of useable heat at operating temperatures > 120˚C for applications such as solar thermal desalination and solar heating industrial processes (SHIP). The low LCOH allows the ICPC to compete with the cheapest, and largest carbon emitting fossil fuel, natural gas.

5.2 *Future Work*

As greenhouse gasses (GHG) continue to rise, the reliance on fossil fuels in the energy sector must be mitigated to limit the impacts of climate change. Solar energy is an abundant resource, available almost everywhere on planet earth, however capturing and harnessing this in a way that is economical in order to compete with carbon emitting fossil fuels can be challenging. With the summarized improvements, the ICPC has the possibility of supplying as low as $0.015/kWh of useable heat at operating temperatures of > 120˚C for applications such as solar thermal desalination and solar heating industrial processes (SHIP). The low LCOH allows the ICPC to compete with the least expensive, and largest carbon emitting fossil fuel, natural gas. It is this researcher's opinion with another round of R&D funding (with focus of upscaling and improving

quality of production/manufacturing) of the ICPC, this collector could be commercial ready for large and fast deployment into today's solar desalination and SHIP markets.

This opinion is supported with the fact that current global government agenda and funding has high focus on mitigating climate change and reducing carbon emissions, along with private sectors also pushing for renewable energy. Within the U.S., the ICPC has secured funding from government initiative programs like DOE's SETO and CEC's many deployment initiatives and progressive goals towards net zero carbon emitting energy sector. The ICPC has been submitted to the DOE's solar initiative contest called "American-Made Solar Desal Prize: Round 2". The ICPC won the first stage of prize ($50,000) and accepted to move on for stage 2 submission teaming phase. The four-stage competition was designed to accelerate the development of low cost desalination systems that use solar-thermal power to produce clean water from salt water.

Chapter 6. References

[1] ESA & NASA/Solar Orbiter/EUI team; Data processing: E. Kraaikamp (ROB), *The_Sun_in_high_resolution*. The European Space Agency, 2022.

[2] C. Payne-Gaposchkin and C. H. P. Gaposchkin, "Stellar Atmospheres: A contribution to the Observational Study of High Temperature in the Reversing Layers of Starts," 1925.

[3] F. Kreith and J. F. Kreider, *Principles of solar engineering*, vol. 1, no. 1. New York: McGraw-Hill Book Company, 1978.

[4] J. A. Duffie and W. A. Beckman, *Solar Engineering of Thermal Processes*, vol. 3, no. February. John Wiley & Sons, Ic., 2006.

[5] C. A. Gueymard, "SMARTS2, a simple models of the atmospheric radiative transfer of sunshine," *Florida Sol. Energy Center/University Cent. Florida*, p. 84, 1995.

[6] A. Mehta, *Introduction to the electromagnetic spectrum and spectroscopy*. 2011.

[7] L. L. Vant-Hull and A. F. Hildebrandt, "Solar thermal power system based on optical transmission," *Sol. Energy*, vol. 18, no. 1, pp. 31–39, 1976, doi: 10.1016/0038-092X(76)90033-5.

[8] C. for the C. L. of the R. C. (Great Britain), S. and E. R. C. (Great B. Nautical Almanac Office, Rutherford Appleton Laboratory, and U. S. N. O. N. A. Office, *The Astronomical Almanac for the Year 2010*. United Kingdon Hydrographic Office, 2008.

[9] M. Blanco-Muriel, D. C. Alarcón-Padilla, T. López-Moratalla, and M. Lara-Coira, "Computing the solar vector," *Sol. Energy*, vol. 70, no. 5, pp. 431–441, 2001, doi: 10.1016/S0038-092X(00)00156-0.

[10] I. Reda and A. A. Nrel, "Solar Position Algorithm for Solar Radiation Applications (Revised)," *Natl. Renew. Energy Lab. Nrel/Tp-560-34302*, no. January, pp. 1–56, 2005.

[11] B. Widyolar, L. Jiang, Y. Bhusal, J. Brinkley, and R. Winston, "Solar thermal process heating with the external compound parabolic concentrator (XCPC) – 45 m2 experimental array performance, annual generation (kWh/m2-year), and economics," *Sol. Energy*, vol. 230, no. May, pp. 131–150, 2021, doi: 10.1016/j.solener.2021.10.027.

[12] R. Jim Skea (United Kingdom), Priyadarshi R Shukla (India), Andy Reisinger (New Zealand) *et al.*, "Mitigation of Climate Change," 2022. doi: 10.1201/9781003264705-7.

[13] P. Kurup, C. Schoeneberger, and C. Mcmillan, "Applications for Solar Thermal for Industrial Processes," 2019.

[14] R. Winston, "High Collection Nonimaging Optics," *6th Mtg Isr. Opt. Eng.*, vol. 1038, no. July 1989, p. 590, 1989, doi: 10.1117/12.951097.

[15] G. Diaz, "Performance analysis and design optimization of a mini-channel evacuated-tube solar collector," in *ASME International Mechanical Engineering Congress and Exposition, vol. 48692*, 2008, pp. 61–67.

[16] N. Sharma and G. Diaz, "Performance model of a novel evacuated-tube solar collector based on minichannels," *Sol. Energy*, vol. 85, no. 5, pp. 881–890, 2011, doi: 10.1016/j.solener.2011.02.001.

[17] A. Robles, V. Duong, A. J. Martin, J. L. Guadarrama, and G. Diaz, "Aluminum minichannel solar water heater performance under year-round weather conditions," *Sol. Energy*, vol. 110, pp. 356–364, 2014, doi: 10.1016/j.solener.2014.09.031.

[18] J. F. Kreider, *Medium and High Temperature Solar Processes*, 1st ed. Academic Press, 1979.

[19] J. Brinkley *et al.*, "Thermal, electrical, and cost study of advanced optical photovoltaic thermal system (ADOPTS)," *Appl. Energy*, vol. 269, no. May, p. 115105, 2020, doi: 10.1016/j.apenergy.2020.115105.

[20] Y. Jia, G. Alva, and G. Fang, "Development and applications of photovoltaic–thermal

systems: A review," *Renew. Sustain. Energy Rev.*, vol. 102, no. June 2018, pp. 249–265, 2019, doi: 10.1016/j.rser.2018.12.030.
[21] T. T. Chow, "A review on photovoltaic/thermal hybrid solar technology," *Appl. Energy*, vol. 87, no. 2, pp. 365–379, 2010, doi: 10.1016/j.apenergy.2009.06.037.
[22] A. Chauhan, V. V. Tyagi, and S. Anand, "Futuristic approach for thermal management in solar PV/thermal systems with possible applications," *Energy Convers. Manag.*, vol. 163, no. January, pp. 314–354, 2018, doi: 10.1016/j.enconman.2018.02.008.
[23] M. Herrando, A. Ramos, J. Freeman, I. Zabalza, and C. N. Markides, "Technoeconomic modelling and optimisation of solar combined heat and power systems based on flat-box PVT collectors for domestic applications," *Energy Convers. Manag.*, vol. 175, no. September, pp. 67–85, 2018, doi: 10.1016/j.enconman.2018.07.045.
[24] F. Huide, Z. Xuxin, M. Lei, Z. Tao, W. Qixing, and S. Hongyuan, "A comparative study on three types of solar utilization technologies for buildings: Photovoltaic, solar thermal and hybrid photovoltaic/thermal systems," *Energy Convers. Manag.*, vol. 140, pp. 1–13, 2017, doi: 10.1016/j.enconman.2017.02.059.
[25] I. Guarracino, J. Freeman, A. Ramos, S. A. Kalogirou, N. J. Ekins-Daukes, and C. N. Markides, "Systematic testing of hybrid PV-thermal (PVT) solar collectors in steady-state and dynamic outdoor conditions," *Appl. Energy*, vol. 240, pp. 1014–1030, 2019, doi: 10.1016/j.apenergy.2018.12.049.
[26] X. Zhang, X. Zhao, S. Smith, J. Xu, and X. Yu, "Review of R&D progress and practical application of the solar photovoltaic/thermal (PV/T) technologies," *Renew. Sustain. Energy Rev.*, vol. 16, no. 1, pp. 599–617, 2012, doi: 10.1016/j.rser.2011.08.026.
[27] C. De Keizer *et al.*, "Evaluating the Thermal and Electrical Performance of Several Uncovered PVT Collectors with a Field Test," *Energy Procedia*, vol. 91, no. 0, pp. 20–26, 2016, doi: 10.1016/j.egypro.2016.06.166.
[28] C. De Keizer and M. De Jong, "PVT Benchmark: An overview of PVT modules on the European market and the barriers and opportunities for the Dutch Market," 2018.
[29] D. Feldman, E. O'Shaughnessy, and R. Margolis, "Solar Industry Update Q3/Q4 2019," *NREL Present.*, no. February, pp. 1–83, 2020, [Online]. Available: https://www.nrel.gov/docs/fy20osti/76158.pdf.
[30] G. Fiorenza, G. L. Paparo, F. Apicella, N. Bianco, and G. Graditi, "Renewable Energy in the Service of Mankind Vol II," *Renew. Energy Serv. Mank. Vol II*, vol. II, 2016, doi: 10.1007/978-3-319-18215-5.
[31] M. Vivar *et al.*, "Initial field performance of a hybrid CPV-T microconcentrator system," *Prog. Photovoltaics Res. Appl.*, vol. 21, no. 8, pp. 1659–1671, Dec. 2013, doi: 10.1002/pip.2229.
[32] J. S. Coventry, "Performance of a concentrating photovoltaic/thermal solar collector," *Sol. Energy*, vol. 78, no. 2, pp. 211–222, 2005, doi: 10.1016/j.solener.2004.03.014.
[33] L. Brottier, S. Naudin, V. Veeser, G. Terrom, and R. Bennacer, "Field Test Results of an Innovative PV/T Collector for Solar Domestic Hot Water," *Energy Procedia*, vol. 91, pp. 276–283, 2016, doi: 10.1016/j.egypro.2016.06.219.
[34] J. Moreno Puerto, "Performance Evaluation of the Solarus AB Asymmetric Concentrating Hybrid PV / T Collector," p. 126, 2013, [Online]. Available: http://hig.diva-portal.org/smash/get/diva2:727716/FULLTEXT01.pdf.
[35] E. Azad, "Experimental analysis of thermal performance of solar collectors with different numbers of heat pipes versus a flow-through solar collector," *Renew. Sustain. Energy Rev.*, vol. 82, no. October 2017, pp. 4320–4325, 2018, doi: 10.1016/j.rser.2017.10.015.
[36] M. J. Carvalho, P. Horta, J. F. Mendes, M. C. Pereira, and W. M. Carbajal, "Incidence angle modifiers: A general approach for energy calculations," *ISES Sol. World Congr. 2007, ISES*

2007, vol. 1, pp. 608–612, 2007, doi: 10.1007/978-3-540-75997-3_112.
[37] W. Li, Y. Shi, K. Chen, L. Zhu, and S. Fan, "A Comprehensive Photonic Approach for Solar Cell Cooling," *ACS Photonics*, vol. 4, no. 4, pp. 774–782, 2017, doi: 10.1021/acsphotonics.7b00089.
[38] David Adam, "How far will global population rise? Researchers can't agree," *Nature*, vol. 597, no. September, pp. 462–465, 2021.
[39] International Energy Agency, "Global Energy Review 2021," 2021. [Online]. Available: https://iea.blob.core.windows.net/assets/d0031107-401d-4a2f-a48b-9eed19457335/GlobalEnergyReview2021.pdf.
[40] Rocky Mountain Climate Organization, "Climate Change in the Headwaters Water and Snow Impacts," Silverthorne, 2018. [Online]. Available: http://www.nwccog.org/wp-content/uploads/2018/02/Climate-Change-in-the-Headwaters.pdf.
[41] J. Melillo, T. Richmond, and G. Yohe, "Ch. 8: Ecosystems, Biodiversity, and Ecosystem Services. Climate Change Impacts in the United States: The Third National Climate Assessment," United States, 2014. [Online]. Available: http://s3.amazonaws.com/nca2014/low/NCA3_Climate_Change_Impacts_in_the_United States_LowRes.pdf?download=1.
[42] M. Oppenheimer and B. Glavovic, "Chapter 4: Sea Level Rise and Implications for Low Lying Islands... SI," pp. 1–31, 2019, [Online]. Available: https://www.ipcc.ch/srocc/.
[43] B. C. O'Neill *et al.*, "IPCC reasons for concern regarding climate change risks," *Nat. Clim. Chang.*, vol. 7, no. 1, pp. 28–37, 2017, doi: 10.1038/nclimate3179.
[44] C. F. Schleussner *et al.*, "Science and policy characteristics of the Paris Agreement temperature goal," *Nat. Clim. Chang.*, vol. 6, no. 9, pp. 827–835, 2016, doi: 10.1038/nclimate3096.
[45] S. H. Mohr, J. Wang, G. Ellem, J. Ward, and D. Giurco, "Projection of world fossil fuels by country," *Fuel*, vol. 141, pp. 120–135, 2015, doi: 10.1016/j.fuel.2014.10.030.
[46] U.S. Energy Information Administration, "Table 1.1 U.S. Primary Energy Overview by year," 2021. [Online]. Available: https://www.eia.gov/totalenergy/data/browser/index.php?tbl=T01.01#/?f=A&start=1949&end=2020&charted=4-6-7-14.
[47] McKinsey & Company, "Global energy perspective 2021," *McKinsey Co.*, no. January, p. 9, 2021.
[48] B. Widyolar, L. Jiang, J. Brinkley, Y. Bhusal, J. Ferry, and R. Winston, "External compound parabolic concentrator (XCPC) for decarbonizing industrial processing heat," no. August 2020, p. 27, 2020, doi: 10.1117/12.2570839.
[49] B. Widyolar, L. Jiang, J. Ferry, and R. Winston, "Non-tracking East-West XCPC solar thermal collector for 200 celsius applications," *Appl. Energy*, vol. 216, no. November 2017, pp. 521–533, 2018, doi: 10.1016/j.apenergy.2018.02.031.
[50] Y. Bhusal, A. Hassanzadeh, L. Jiang, and R. Winston, "Technical and economic analysis of a novel low cost concentrated medium-temperature solar collector," *Renew. Energy*, vol. 146, pp. 968–985, 2020, doi: 10.1016/j.renene.2019.07.032.
[51] M. Ashouri, A. M. Khoshkar Vandani, M. Mehrpooya, M. H. Ahmadi, and A. Abdollahpour, "Techno-economic assessment of a Kalina cycle driven by a parabolic Trough solar collector," *Energy Convers. Manag.*, vol. 105, pp. 1328–1339, 2015, doi: 10.1016/j.enconman.2015.09.015.
[52] G. Hoste and N. Schuknecht, "Thermal Efficiency Analysis of SkyFuel's Advanced, Large-aperture, Parabolic Trough Collector," *Energy Procedia*, vol. 69, pp. 96–105, 2015, doi: 10.1016/j.egypro.2015.03.012.
[53] K. Mohammadi, S. Khanmohammadi, J. Immonen, and K. Powell, "Techno-economic

analysis and environmental benefits of solar industrial process heating based on parabolic trough collectors," *Sustain. Energy Technol. Assessments*, vol. 47, no. June, p. 101412, 2021, doi: 10.1016/j.seta.2021.101412.

[54] I. Lillo-Bravo, E. Pérez-Aparicio, N. Sancho-Caparrini, and M. A. Silva-Pérez, "Benefits of Medium Temperature Solar Concentration Technologies as Thermal Energy Source of Industrial Processes in Spain," *Energies*, vol. 11, no. 11, 2018, doi: 10.3390/en11112950.

[55] F. Calise, M. D. D'Accadia, M. Vicidomini, and M. Scarpellino, "Design and simulation of a prototype of a small-scale solar CHP system based on evacuated flat-plate solar collectors and Organic Rankine Cycle," *Energy Convers. Manag.*, vol. 90, pp. 347–363, 2015, doi: 10.1016/j.enconman.2014.11.014.

[56] A. Buonomano *et al.*, "Experimental analysis and dynamic simulation of a novel high-temperature solar cooling system," *Energy Convers. Manag.*, vol. 109, pp. 19–39, 2016, doi: 10.1016/j.enconman.2015.11.047.

[57] A. Wahed, M. Bieri, T. K. Kui, and T. Reindl, "Levelized Cost of Solar Thermal System for Process Heating Applications in the Tropics," in *Transition Towards 100% Renewable Energy: Selected Papers from the World Renewable Energy Congress WREC 2017*, vol. 269, no. January, A. Sayigh, Ed. Springer International Publighing AG 2018, 2018, pp. 441–450.

[58] G. Zhu, T. Wendelin, M. J. Wagner, and C. Kutscher, "History, current state, and future of linear Fresnel concentrating solar collectors," *Sol. Energy*, vol. 103, pp. 639–652, 2014, doi: 10.1016/j.solener.2013.05.021.

[59] T. Sultana, G. L. Morrison, R. Taylor, and G. Rosengarten, "TRNSYS modeling of a linear Fresnel concentrating collector for solar cooling and hot water applications," *J. Sol. Energy Eng. Trans. ASME*, vol. 137, no. 2, pp. 1–9, 2015, doi: 10.1115/1.4028868.

[60] Z. Naghibi, S. Ekhtiari, R. Carriveau, and D. S. Ting, " Hybrid solar thermal/ photovoltaic-battery energy storage system in a commercial greenhouse: Performance and economic analysis ," *Energy Storage*, vol. 3, no. 1, pp. 1–19, 2021, doi: 10.1002/est2.215.

[61] V. P. Stefanovic, S. R. Pavlovic, E. Bellos, and C. Tzivanidis, "A detailed parametric analysis of a solar dish collector," *Sustain. Energy Technol. Assessments*, vol. 25, no. December 2017, pp. 99–110, 2018, doi: 10.1016/j.seta.2017.12.005.

[62] S. Abdelhady, "Performance and cost evaluation of solar dish power plant: sensitivity analysis of levelized cost of electricity (LCOE) and net present value (NPV)," *Renew. Energy*, vol. 168, pp. 332–342, 2021, doi: 10.1016/j.renene.2020.12.074.

[63] J. D. Garrison, "Optimization of a fixed solar thermal collector," *Sol. Energy*, vol. 23, no. 2, pp. 93–102, 1979, doi: 10.1016/0038-092X(79)90108-7.

[64] K. A. Snail, J. J. O'Gallagher, and R. Winston, "A stationary evacuated collector with integrated concentrator," *Sol. Energy*, vol. 33, no. 5, pp. 441–449, 1984, doi: 10.1016/0038-092X(84)90196-8.

[65] W. S. Duff, R. Winston, J. J. O'Gallagher, J. Bergquam, and T. Henkel, "Performance of the Sacramento demonstration ICPC collector and double effect chiller," *Sol. Energy*, vol. 76, no. 1–3, pp. 175–180, 2004, doi: 10.1016/j.solener.2003.08.022.

[66] W. Duff and J. Daosukho, "Twelve year Evaluation of a Novel ICPC Solar Collector Installation: The Role of Failure Modes in Changing Optical and Thermal Performance," in *39th ASES National Solar Conference 2010, SOLAR 2010*, 2010, vol. 6, pp. 3530–3576.

[67] W. S. Duff and J. Daosukho, "Twenty years' experience with a novel geometry ICPC evacuated solar collector," *Energy Procedia*, vol. 57, pp. 2285–2294, 2014, doi: 10.1016/j.egypro.2014.10.236.

[68] L. Jiang, "Implementation of thermodynamically efficient collectors for medium high temperature applications," *UC Merced Electron. Theses Diss.*, 2014, [Online]. Available:

https://escholarship.org/uc/item/4cn1d17h.
[69] L. Jiang, B. Widyolar, and R. Winston, “Characterization of Novel Mid-temperature CPC Solar Thermal Collectors,” *Energy Procedia*, vol. 70, pp. 65–70, 2015, doi: 10.1016/j.egypro.2015.02.098.
[70] B. K. Widyolar *et al.*, “Low cost solar photovoltaic-thermal (PVT) collector using aluminum minichannels and nonimaging optics,” no. August 2020, p. 22, 2020, doi: 10.1117/12.2570838.
[71] B. Widyolar *et al.*, “Experimental performance of an ultra-low cost solar photovoltaic-thermal (PVT) collector using aluminum minichannels and nonimaging optics,” *Appl. Energy*, vol. 268, no. April, p. 114894, 2020, doi: 10.1016/j.apenergy.2020.114894.
[72] L. Evangelisti, R. De Lieto Vollaro, and F. Asdrubali, “Latest advances on solar thermal collectors: A comprehensive review,” *Renew. Sustain. Energy Rev.*, vol. 114, no. March, p. 109318, 2019, doi: 10.1016/j.rser.2019.109318.
[73] M. Born and E. Wolf, *Principles of Optics*, 7th Expand., vol. 7, no. 2. University Press, Cambridge, 2003.
[74] R. Winston, J. J. O’Gallagher, J. Muschaweck, A. R. Mahoney, and V. Dudley, “Comparison of Predicted and Measured Performance of an Integrated Compound Parabolic Concentrator (ICPC),” in *ISES Solar World Congress 1999, Volume III*, 1999, pp. 382–387.
[75] R. Winston, J. O’Gallagher, A. R. Mahoney, V. E. Dudley, and R. Hoffman, “Initial Performance Measurements from a Low Concentration Version of an Integrated Compound Parabolic Concentrator (ICPC),” in *Proceedings of the 1998 American Solar Energy Society Annual Conference*, 1998, pp. 369–374.

Chapter 7. Appendices

Appendix A

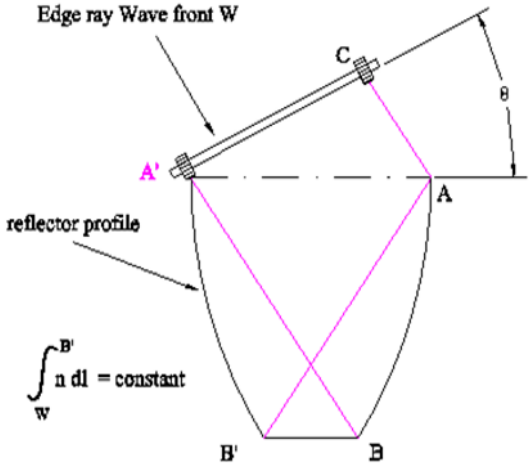

$$B'A + AC = B'B + BA'$$

$$B'A = BA'$$

$$BB' = AC = AA'\sin\vartheta$$

$$\Rightarrow AA'\sin\vartheta = BB'$$

$$C = \frac{AA'}{BB'} = \frac{1}{\sin\vartheta}$$

$$C(\text{cone}) = \left(\frac{AA'}{BB'}\right)^2 = \frac{1}{\sin^2\vartheta}$$

sine law of concentration limit!

Appendix B

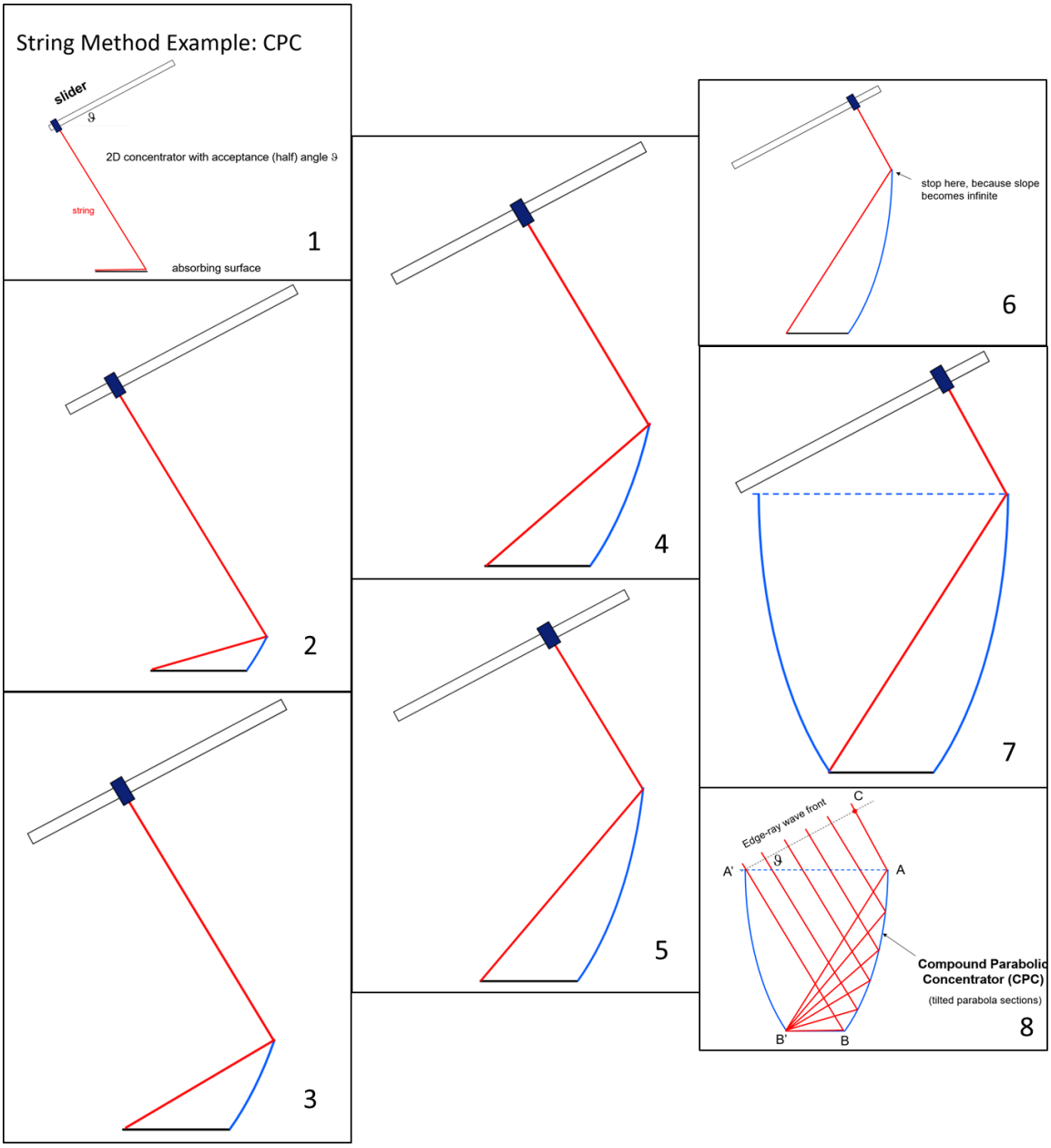
String Method Example: CPC
slider
ϑ
2D concentrator with acceptance (half) angle ϑ
string
absorbing surface
1
2
3
4
5
stop here, because slope becomes infinite
6
7
Edge-ray wave front
C
A'
ϑ
A
B'
B
Compound Parabolic Concentrator (CPC)
(tilted parabola sections)
8

Appendix C

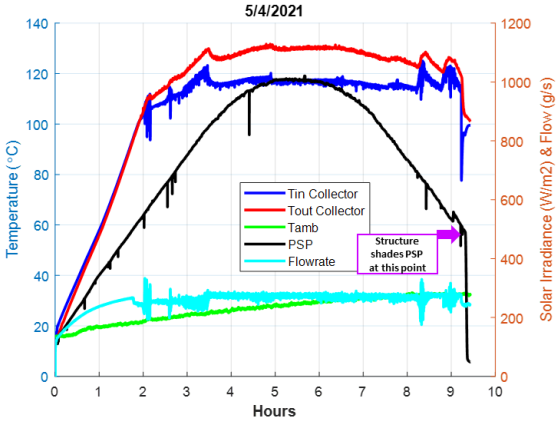
5/4/2021
Temperature (°C)
Solar Irradiance (W/m2) & Flow (g/s)
Hours
Tin Collector
Tout Collector
Tamb
PSP
Flowrate
Structure shades PSP at this point

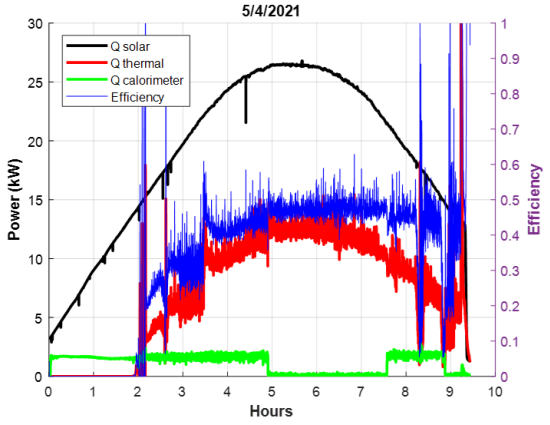
5/4/2021
Power (kW)
Efficiency
Hours
Q solar
Q thermal
Q calorimeter
Efficiency

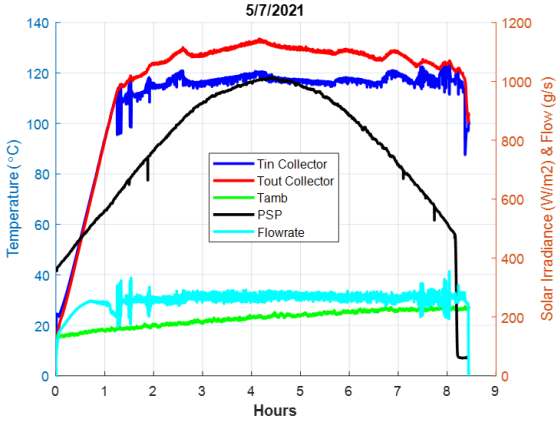
5/7/2021
Temperature (°C)
Solar Irradiance (W/m2) & Flow (g/s)
Hours
Tin Collector
Tout Collector
Tamb
PSP
Flowrate

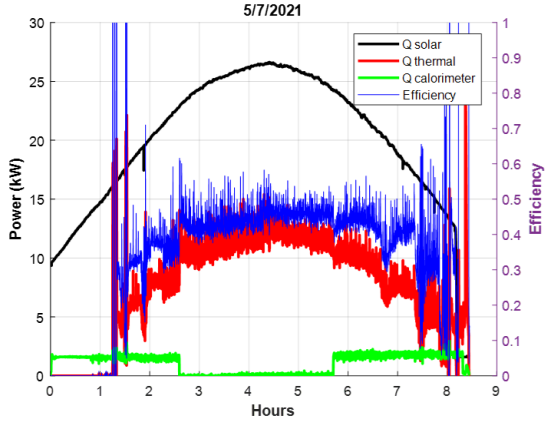
5/7/2021
Power (kW)
Efficiency
Hours
Q solar
Q thermal
Q calorimeter
Efficiency

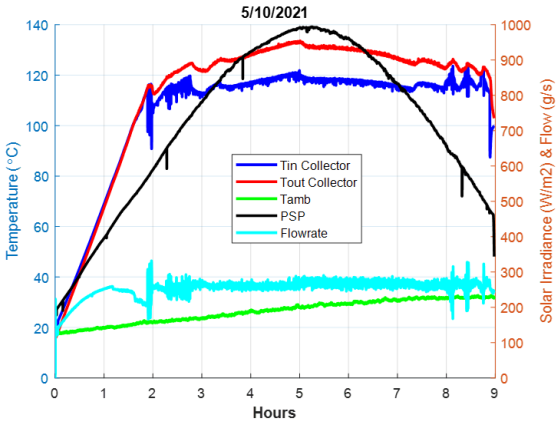
5/10/2021
Temperature (°C)
Solar Irradiance (W/m2) & Flow (g/s)
Hours
Tin Collector
Tout Collector
Tamb
PSP
Flowrate

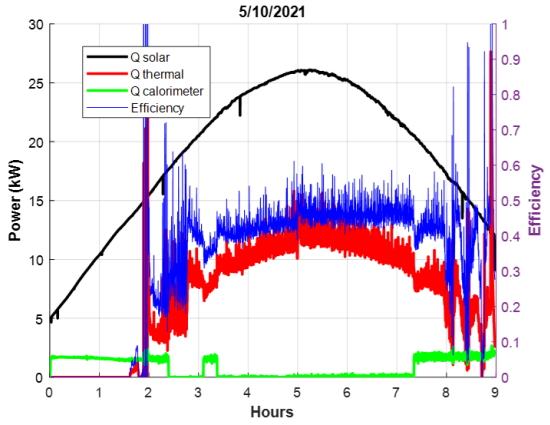
5/10/2021
Power (kW)
Efficiency
Hours
Q solar
Q thermal
Q calorimeter
Efficiency

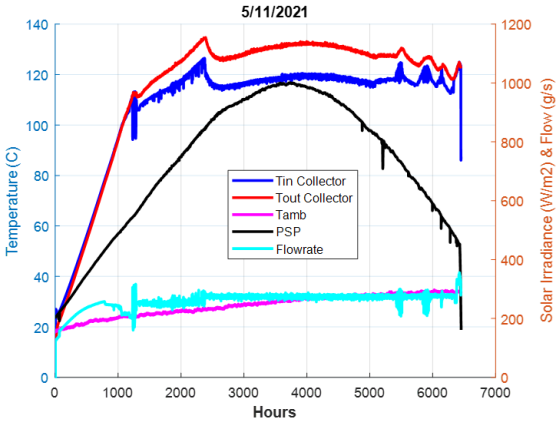
5/11/2021
Temperature (C)
Solar Irradiance (W/m2) & Flow (g/s)
Hours
Tin Collector
Tout Collector
Tamb
PSP
Flowrate

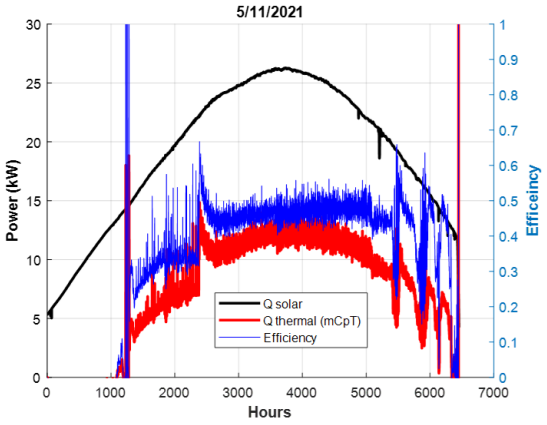
5/11/2021
Power (kW)
Efficiency
Hours
Q solar
Q thermal (mCpT)
Efficiency

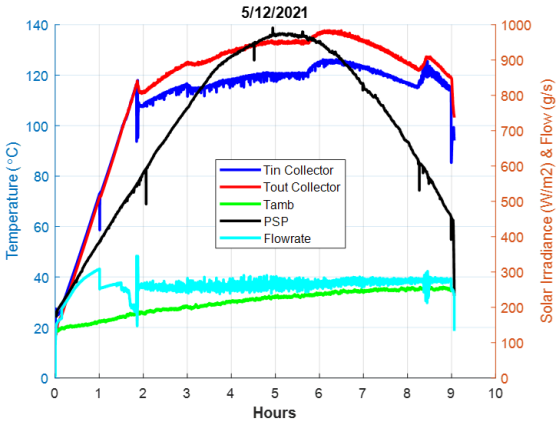
5/12/2021
Temperature (°C)
Solar Irradiance (W/m2) & Flow (g/s)
Hours
Tin Collector
Tout Collector
Tamb
PSP
Flowrate

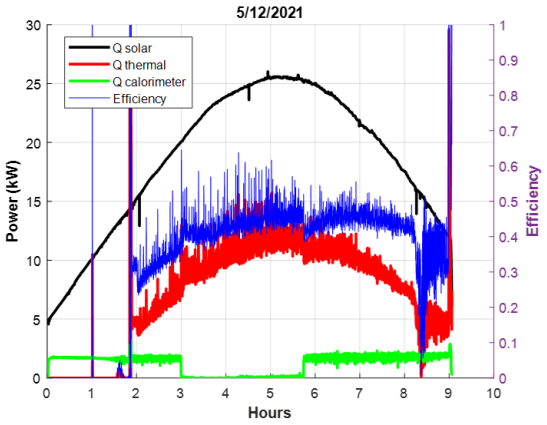
5/12/2021
Power (kW)
Efficiency
Hours
Q solar
Q thermal
Q calorimeter
Efficiency

Appendix D

Date	Fluid temp	flow (g/s)	Flow (kg/s)	Flow in channel (kg/s)	velocity (m/s)	Re	Nu
4-May	127	269	0.269	0.000590	0.182	596	
7-May	127	266	0.266	0.000583	0.180	589	3.66 = laminar with constant
10-May	127	263	0.263	0.000577	0.178	583	surface temperature for circular
11-May	128	270	0.27	0.000592	0.183	598	tube
12-May	130	266	0.266	0.000583	0.180	589	

Assumptions:
Nu = 4.36 = laminar with constant heat flux for circular tube
Don't think this is true since we visibly see a focus point of light on bottom half
Assuming temperature is constant because thermal resistance through 1/2 mm Al wall is extremely low

Minichannel Schematic:

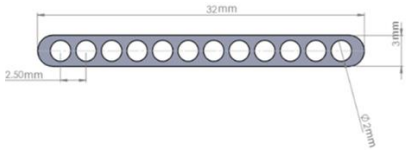

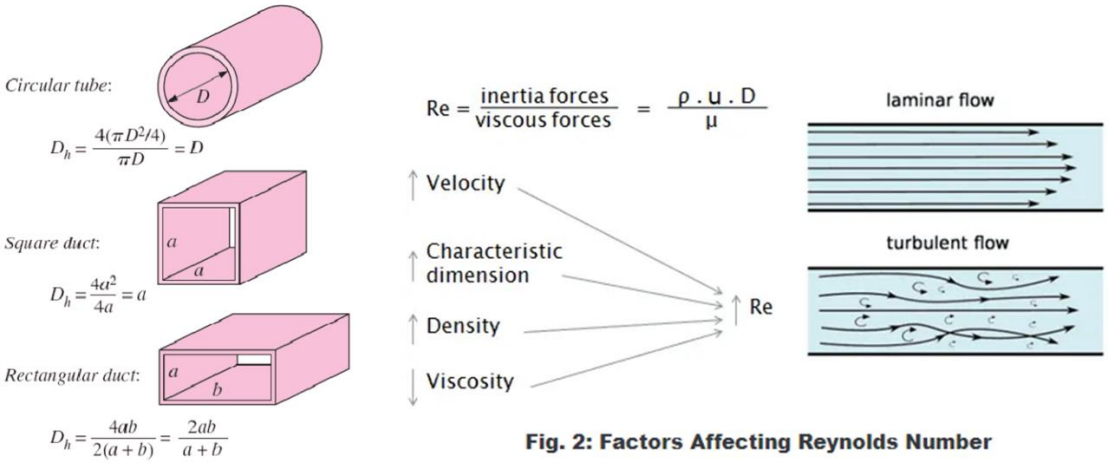

Fig. 2: Factors Affecting Reynolds Number

Therefore, for fully developed **laminar flow** in a circular tube subjected to constant surface heat flux, the Nusselt number is a constant. There is no dependence on the Reynolds or the Prandtl numbers.

Laminar Flow - Circular Tube

$$Nu_L = \frac{h.L}{k_f} = 4.36$$

where:
Nu is the Nusselt number [-]

Validity:

Constant Surface Heat Flux

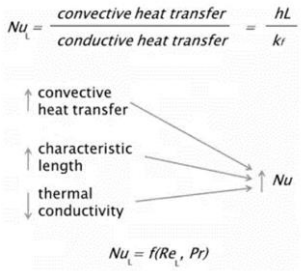

Sources:

Nusselt figure: https://www.nuclear-power.com/nuclear-engineering/heat-transfer/introduction-to-heat-transfer/characteristic-numbers/what-is-nusselt-number/

hydraulic diameter: http://nuclear-power.com/wp-content/uploads/2016/05/Hydraulic-Diameter-non-circular-tubes.png

Reynold's figure: https://whatispiping.com/reynolds-number/